

Copyright Warning & Restrictions

The copyright law of the United States (Title 17, United States Code) governs the making of photocopies or other reproductions of copyrighted material.

Under certain conditions specified in the law, libraries and archives are authorized to furnish a photocopy or other reproduction. One of these specified conditions is that the photocopy or reproduction is not to be “used for any purpose other than private study, scholarship, or research.” If a user makes a request for, or later uses, a photocopy or reproduction for purposes in excess of “fair use” that user may be liable for copyright infringement,

This institution reserves the right to refuse to accept a copying order if, in its judgment, fulfillment of the order would involve violation of copyright law.

Please Note: The author retains the copyright while the New Jersey Institute of Technology reserves the right to distribute this thesis or dissertation

Printing note: If you do not wish to print this page, then select “Pages from: first page # to: last page #” on the print dialog screen

The Van Houten library has removed some of the personal information and all signatures from the approval page and biographical sketches of theses and dissertations in order to protect the identity of NJIT graduates and faculty.

ABSTRACT

GLOBAL MHD AND ACOUSTIC SOLAR MODELING AND HELIOSEISMIC ANALYSIS

by
Andrey M. Stejko

Computational fluid dynamic simulations have become one of the most prolific avenues of study in the fields of solar and stellar physics within the last several decades. With the advent of ever increasing computing power, high-definition global models of the Sun have become indispensable in understanding the complex and chaotic nature of flows in the solar interior, as well as their impact on the evolution of the global solar dynamo. The mechanisms that connect the generation of the toroidal magnetic field at the base of the convection zone to the emergence of a poloidal field onto the solar surface can be explored with the non-linear global model: EULAG-MHD (EULerian/semi-LAGrangian fluid solver—MagnetoHydroDynamic extension). This model is used to investigate the role that subsurface shear plays in shaping the extended solar magnetic cycle. The simulation of a wide range of convective near-surface transport regimes demonstrates that increased subsurface convection appears to have a significant impact on the distribution of angular momentum and the development of the α -effect—responsible for transforming the toroidal magnetic field into a poloidal one. These changes result in a global shift of the surface expression of the solar dynamo, from a North-South symmetric pattern to a staggered anti-symmetric emergence, more in line with solar observations.

The results of these global MHD models illustrate the significance of the near-surface shear layer (NSSL) and the radiative-convective interface (the tachocline) in shaping the evolution of the global magnetic field. The crucial key connecting the magnetic activity in these two layers is the action of the meridional circulation in the convection zone. The exact nature of meridional structure, however, is uncertain, with

techniques in helioseismology showing inferences for both single-cell and double-cell meridional profiles—results that carry large implications for the transport of magnetic flux near the tachocline. In order to address this controversy from a modeling perspective, this dissertation presents the formulation of a three-dimensional (3D) numerical solver of the linearized compressible Euler equations (GALE—Global Acoustic Linearized Euler), on a full spherical mesh. The application of an efficient pseudo-spectral computational method is used to calculate the contribution of the material derivative dyad in its conservative form, simulating the impact internal solar mass flows on helioseismic signatures. This algorithm is employed in a forward-modeling capacity, investigating profiles of single-cell meridional circulation with deep and shallow return flows, as well as double-cell meridional circulation with strong and weak reversals. The travel-time signatures for the four profiles are measured in an attempt to explore whether deviations in these regimes can be distinguished from realization noise—simulated by the stochastic excitation of resonant modes in the convective interior. These measurements show that even though the low-end of differences between profiles of single- and double-cell meridional circulation may be indistinguishable, the analysis of meridional circulation generated by mean-field models may offer the opportunity to better understand and constrain inferences of helioseismology in the context of their impact on global dynamics.

The pseudo-spectral method used in the formulation of the GALE code presents the possibility of extending its numerical techniques to the contributions of all external forces in their conservative form. This allows for the development of a new efficient non-linear compressible global MHD algorithm, computed entirely in frequency space. Such a global solar model can be used to explore the connection between the action of the dynamo on the solar surface and at the tachocline as a single interconnected evolving system, something that cannot be adequately achieved in the anelastic approximation employed in many global solar MHD models.

**GLOBAL MHD AND ACOUSTIC SOLAR MODELING AND
HELIOSEISMIC ANALYSIS**

by
Andrey M. Stejko

**A Dissertation
Submitted to the Faculty of
New Jersey Institute of Technology and
Rutgers, The State University of New Jersey-Newark,
in Partial Fulfillment of the Requirements for the Degree of
Doctor of Philosophy in Applied Physics**

Department of Physics

May 2021

Copyright © 2021 by Andrey M. Stejko

ALL RIGHTS RESERVED

APPROVAL PAGE

**GLOBAL MHD AND ACOUSTIC SOLAR MODELING AND
HELIOSEISMIC ANALYSIS**

Andrey M. Stejko

Dr. Alexander G. Kosovichev, Dissertation Advisor
Professor of Physics, NJIT Date

Dr. Gelu M. Nita, Committee Member
Research Professor of Physics, NJIT Date

Dr. Gregory D. Fleishman, Committee Member
Distinguished Research Professor of Physics, NJIT Date

Dr. Haimin Wang, Committee Member
Distinguished Professor of Physics, NJIT Date

Dr. Yuan-Nan Young, Committee Member
Professor of Mathematical Sciences, NJIT Date

Dr. Daniel Murnick, Committee Member
Distinguished Professor of Physics, Rutgers Date

BIOGRAPHICAL SKETCH

Author: Andrey M. Stejko
Degree: Doctor of Philosophy
Date: May 2021

Undergraduate and Graduate Education:

- Doctor of Philosophy in Applied Physics,
New Jersey Institute of Technology, Newark, NJ, 2021
- Bachelor of Arts in Applied Physics,
Ithaca College, Ithaca, NY, 2015

Major: Applied Physics

Presentations and Publications:

- Stefan, J. T., Kosovichev, A. G., & Stejko, A. M. 2021. Analysis of Time-Distance Helioseismology for Detection of Emerging Active Regions. *ApJ*, in press. <https://arxiv.org/abs/2012.01367> [accessed on May 1, 2021]
- Stejko, A. M., Kosovichev, A. G., & Pipin, V. V. 2021b. Helioseismic Signatures of One- and Two-cell Meridional Circulation. *ApJ*, 911, 90, doi: [10.3847/1538-4357/abec70](https://doi.org/10.3847/1538-4357/abec70)
- Stejko, A. M., Kosovichev, A. G., & Mansour, N. N. 2021a. Helioseismic Modeling of Background Flows. *ApJS*, 253, 9, doi: [10.3847/1538-4365/abd3fe](https://doi.org/10.3847/1538-4365/abd3fe)
- Stejko, A. M., Guerrero, G., Kosovichev, A. G., & Smolarkiewicz, P. K. 2020. 3D MHD Modeling of the Impact of Subsurface Stratification on the Solar Dynamo. *ApJ*, 888, 16, doi: [10.3847/1538-4357/ab5854](https://doi.org/10.3847/1538-4357/ab5854)
- Zhao, J., Stejko, A., & Chen, R. 2016. Effect of Foreshortening on Center-to-limb Variations of Measured Acoustic Travel Times. *Sol. Phys.*, 291, 731, doi: [10.1007/s11207-016-0864-7](https://doi.org/10.1007/s11207-016-0864-7)
- Stejko, A. M. 2020. Helioseismology Techniques explored Through 3D Global Modeling. In *2020 AGU Fall Meeting*, SH002-0004
- Stejko, A. M. 2020. Modeling Internal Solar Oscillations. In *AAS Solar Physics Division meeting #51*, 204.02. <https://ui.adsabs.harvard.edu/abs/2020SPD....5120402S> [accessed on May 1, 2021]

- Stejko, A. M. 2016. New Modeling Tools Help Explore the Interior of the Sun. In *SC20 Supercomputing Conference*, 17. <https://www.nas.nasa.gov/SC20/demos/demo17.html> [accessed on May 1, 2021]
- Stejko, A. M., Guerrero, G., & Kosovichev, A. G. 2019. Modeling of Subsurface Shear with EULAG-MHD. In *American Astronomical Society Meeting #234*, 302.08. <https://ui.adsabs.harvard.edu/abs/2019AAS...23430208S> [accessed on May 1, 2021]
- Stejko, A. M. 2017. 3D Global Modeling of the Solar Dynamo. In *Solar Heliospheric and INterplanetary Environment (SHINE 2017)*, 49. <https://ui.adsabs.harvard.edu/abs/2017shin.confE..49S> [accessed on May 1, 2021]
- Stejko, A. M. 2016. Exploring the Sun through High-resolution Modeling. In *SC16 Supercomputing Conference*, 12. <https://www.nas.nasa.gov/SC16/demos/demo12.html> [accessed on May 1, 2021]

*Through the closed blinds the golden sun
Poured in a dusty beam,
Like the celestial ladder seen
By Jacob in his dream.*

Henry Wadsworth Longfellow

ACKNOWLEDGMENT

I would like to thank my research and dissertation advisor Dr. Alexander Kosovichev, for presenting me with an amazing opportunity to learn and do interesting and insightful research, as well as sharing some of his passion for the field of heliophysics.

I would like to thank the committee members, Drs. Gelu Nita, Gregory Fleishman, Haimin Wang, Yuan-Nan Young, and Daniel Murnick for their time and their expertise, as well as for helping foster an environment at NJIT and Rutgers-Newark where young scientists are encourage to learn and grow

I would also like to thank the Applied Physics departments at NJIT for providing financial support, as well as a strong foundation of faculty that help students discover their passion for learning every day.

This work is supported by the NASA grants: 80NSSC19K0630, 80NSSC19K1436, NNX14AB70G and NNX17AE76A.

I want to thank the heliophysics modeling and simulation team at the NASA Ames Research Center, including Drs. Alan Wray and Irina Kitiashvili, for an amazing working opportunity and very productive and instructive meetings that kept the research in this dissertation on track. I want to thank the former head of the HMS team, Dr. Nagi Mansour, whose notes became the foundation for the development of a new compressible algorithm. I want to thank Drs. Phillip Scherrer and Junwei Zhao for the opportunity to perform summer research at Stanford University, supporting me in navigating through one of my first professional working environments. I also want to thank Dr. Joyce Guzik for the opportunity of a summer fellowship at the Los Alamos Research Lab, one of the most scientifically compelling experiences of my early career.

I want to thank my wife, Aarushi Bhardwaj, who encouraged me to pursue my passion and to never give up. I want to also thank my mother, Lina Stejko, and my

sister, Lily Stejko, for helping to nurture my early interests in science and learning, as well as for providing me with the foundation to be the person that I am today.

TABLE OF CONTENTS

Chapter	Page
1 INTRODUCTION	1
1.1 The Solar Dynamo	1
1.1.1 Active regions	4
1.2 Solar Dynamics	5
1.2.1 Helioseismology	5
1.2.2 Differential rotation	7
1.2.3 Meridional circulation	8
1.3 Global Modeling - Overview and Motivation	12
1.3.1 MHD modeling	12
1.3.2 Acoustic modeling	13
1.4 Outline	15
2 GLOBAL MHD MODELING WITH EULAG	18
2.1 Model Description	18
2.2 Modifying the NSSL	21
2.3 Results	23
2.3.1 Mean-field analysis	30
2.4 Discussion	36
3 GLOBAL ACOUSTIC MODEL	39
3.1 Summary of the Governing Equations	39
3.1.1 Linearized field formulation	39
3.2 Derivation	40
3.2.1 Mass continuity	40
3.2.2 Conservation of momentum	41
3.2.3 Conservation of energy	43
3.3 Brunt-Väisälä Frequency	44

TABLE OF CONTENTS
(Continued)

Chapter	Page
3.4 Acoustic Oscillation Source Function	45
3.5 Damping Layer	46
3.6 Numerical Method	48
3.6.1 Temporal discretization	48
3.6.2 Radial discretization and differentiation	49
3.6.3 Spherical harmonic decomposition and differentiation	51
3.6.4 Numerical solver of the potential field	53
3.6.5 Material derivative dyad	56
3.6.6 Rotating reference frame	57
3.6.7 Stability and CFL condition	59
3.6.8 Parallelization	62
3.7 Model Validation	64
3.7.1 Power spectrum	64
3.7.2 Rotation	65
3.7.3 Sound speed perturbations	67
4 HELIOSEISMIC ANALYSIS	72
4.1 Model Parameters	72
4.2 Deep Focusing Method	72
4.3 Measuring Acoustic Travel Times	75
4.3.1 Characterizing noise	79
4.4 Analysis of Meridional Circulation	83
4.4.1 Meridional profiles	83
5 DISCUSSION	90
5.1 Global Solar Modeling	90
5.2 The GALE Code	91
5.3 Future Plans	94

TABLE OF CONTENTS
(Continued)

Chapter	Page
5.3.1 Magnetic field extension	94
5.3.2 Non-linear algorithm	96
APPENDIX A VECTOR/TENSOR SPHERICAL HARMONICS	101
A.1 Vector Spherical Harmonics	101
A.2 Tensor Spherical Harmonics	103
A.3 Properties	111
A.4 Divergence	112
A.5 Curl	114
APPENDIX B RECURSION RELATIONS	116
B.1 Calculating Clebsch-Gordan Coefficients	116
B.2 Deriving Recursion Relations	120
B.2.1 Surface functions	120
B.2.2 Surface derivatives	122
REFERENCES	125

LIST OF FIGURES

Figure	Page
1.1 The global magnetic field generated by the EULAG-MHD model.	1
1.2 The butterfly diagram of sunspots shows their average location in latitude plotted against time, since the first detailed observations in 1874.	2
1.3 A visual representation of the evolution of the solar dynamo.	3
1.4 An active region as viewed by the 1-meter Swedish Solar Telescope and the Solar Dynamics Observatory.	4
1.5 A representation of the path of acoustic rays traveling through the solar interior.	6
1.6 The contour of rotational frequency in the Sun.	7
1.7 A simple model of meridional circulation in the convection zone, consistent with the continuity of mass flows in the Sun.	8
1.8 Travel-time differences in the cross-correlation of acoustic oscillations, demonstrating the systematic center-to-limb effect, where ϕ is the distance from the center of the observed solar disk.	9
1.9 The latitudinal velocities (u_θ in m s^{-1}) that characterize meridional circulation.	11
2.1 Profiles of ambient states of the potential temperature (Θ_e) for simulations: ns1, ns2, and ns3.	23
2.2 The time averaged (over three dynamo cycles) and azimuthally-averaged differential rotation and meridional circulation profiles: ns1, ns2, and ns3.	24
2.3 Radial shear profiles of simulations ns1 and ns2, characterized by the radial derivative of the angular velocity.	26
2.4 Radial profile of the rms velocity (u'_{rms}).	28
2.5 The time-latitude diagrams of the magnetic field (B_ϕ measured in Tesla) for simulations ns1, ns2, and ns3 at $0.95 R_\odot$ and $0.72 R_\odot$, as well as the time-radius diagram at a 45° latitude.	29
2.6 Radial dependence of the turbulent diffusivity, η_t , and the Alfvén and kinetic correlation times, τ_a and τ_k , as defined by the first-order smoothing approximation (FOSA).	32
2.7 Snapshots of polarity reversal for model ns1.	33

LIST OF FIGURES
(Continued)

Figure	Page
2.8 Same as Figure 2.7 for simulation ns2.	34
2.9 The magnetic turbulent transport coefficient, α_m , computed from the current helicity in the FOSA.	36
3.1 The altered background profile of the Brunt-Väisälä frequency, where slightly negative values in the convection zone are set to zero.	45
3.2 An example of the frequency spectrum that characterizes the time-dependent profile of the source of acoustic oscillations near the surface of the model.	46
3.3 The background profiles of pressure and density.	47
3.4 A 1D representation of the radial grid.	50
3.5 The distance between radial grid points in cm.	51
3.6 A representation of the 3D structure of the model grid.	52
3.7 A representation of real-space mesh-point storage in memory.	62
3.8 A symbolic representation of memory arrangement across compute ranks.	63
3.9 An $l-\nu$ diagram, showing the power spectrum of p-modes sampled 20 km above the model surface.	65
3.10 The angular frequency (Ω) profile derived from model M1, described in Pipin & Kosovichev (2019).	66
3.11 An $m-\nu$ diagram, showing the power spectrum of acoustic oscillation, sampled 30 km above the model surface, for spherical harmonic degree $l = 180$	67
3.12 An $l-\nu$ diagram for a spectral resolution of $l_{max} = 1000$, showing the power spectrum of p-modes sampled 30 km above the model surface.	68
3.13 The acoustic power map generated by a summation of Fourier decomposed modes over the frequency intervals: 1-3 mHz and 3-5 mHz, sampled 30 km above the solar surface.	69
3.14 Acoustic power maps of sound speed perturbations, over the frequency intervals: 1-3 mHz and 3-5 mHz, remapped into $30^\circ \times 30^\circ$ patches.	70
4.1 Time-distance diagram of the cross-correlation of radial velocity perturbations for various angular travel distances (Δ), sampled 300 km above the solar surface.	73

LIST OF FIGURES
(Continued)

Figure	Page
4.2 An illustration of the deep-focusing method.	75
4.3 The latitudinal velocity (\tilde{u}_θ) of a single-cell model of meridional circulation (Hartlep et al., 2013).	76
4.4 The N-S travel-time differences (δt_{NS}) as a function of latitude for six different depths.	77
4.5 The N-S travel-time differences (δt_{NS}) under the application of a Gaussian phase-speed filter ($\sigma = 0.05v_p$) as a function of latitude for six different depths.	78
4.6 The N-S travel-time differences (δt_{NS}) with noise subtracted from the corresponding model with no flows.	80
4.7 The N-S travel-time differences (δt_{NS}) under the application of a Gaussian phase-speed filter ($\sigma = 0.05v_p$) with noise subtracted from the corresponding model with no flows.	81
4.8 The error in travel-time differences ($\delta\tau$) as a function of travel distance (Δ) for five latitudinal averages.	82
4.9 Latitudinal velocities (\tilde{u}_θ), generated by the mean-field models of Pipin & Kosovichev (2019) (M1 and M2) and Pipin & Kosovichev (2018) (K1 and K2—referred to as M2 and M3 in their paper).	84
4.10 The N-S travel-time differences ($\delta\tau_{NS}$) as a function of travel distance (Δ) for models M1, M2, K1, and K2. The travel-time measurements are shown unfiltered for five latitudinal averages.	85
4.11 The N-S travel-time differences ($\delta\tau_{NS}$) as a function of travel distance (Δ) for models M1, M2, K1, and K2. The travel-time measurements are shown under the application of a Gaussian phase-speed filter ($\sigma = 0.05v_p$) for five latitudinal averages.	86
4.12 The N-S travel-time differences ($\delta\tau_{NS}$) as a function of travel distance (Δ) for models M1, M2, K1, and K2, under the application of Gaussian phase-speed filter ($\sigma = 0.05v_p$), with profiles of noise subtracted for five latitudinal averages.	88
4.13 The N-S travel-time differences ($\delta\tau_{NS}$) as a function of travel distance (Δ) for MDI/GONG data published by Gizon et al. (2020).	89

CHAPTER 1

INTRODUCTION

1.1 The Solar Dynamo

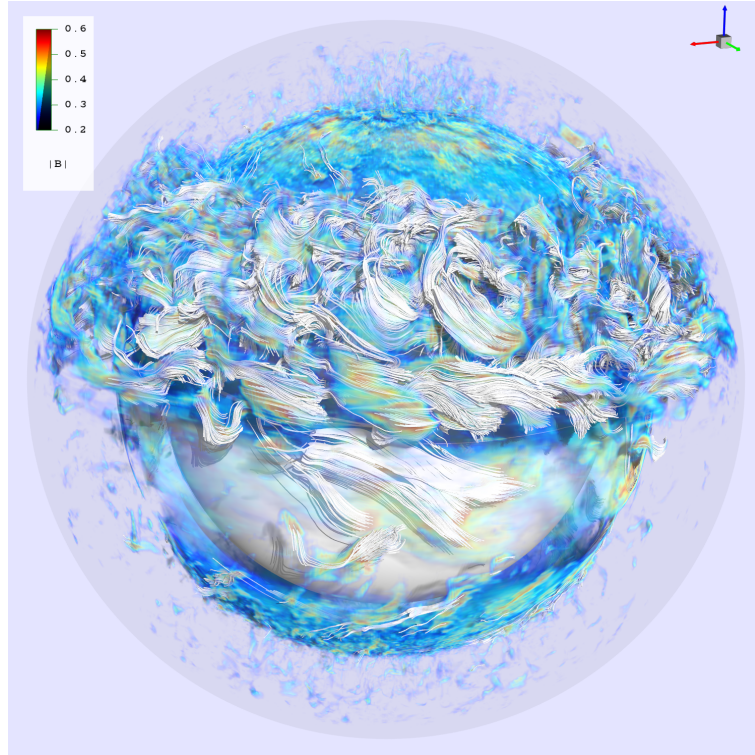


Figure 1.1 The global magnetic field generated by the EULAG-MHD model (see Chapter 2). A strong toroidal magnetic field is shown emerging onto the surface in the upper hemisphere, with magnetic field lines drawn in.

Source: Image generated by Timothy Sandstrom NASA/NAS.

The solar dynamo is a complex magnetic mechanism that serves as the generator for the Sun's magnetic field and the 11-year solar cycle that can be observed in the sunspot pattern on the solar surface (Figure 1.2). By employing large-scale flows of plasma on the Sun, such as differential rotation (see Subsection 1.2.2) and meridional circulation (see Subsection 1.2.3), together with the contribution of turbulent cyclonic motions and currents, the so called α -effect, models of the solar dynamo aim

to simulate the development and evolution of the large-scale solar magnetic field (Charbonneau, 2010). Polarity reversals every 11 years, equatorward migration of sunspots during cycles, as well as the hemispheric anti-symmetry of the magnetic field, however, are issues that still have not been adequately explained. Between mean-field dynamo-wave (Parker, 1955; Moffatt, 1978; Brandenburg & Subramanian, 2005; Pipin & Kosovichev, 2019) and flux-transport (Babcock, 1961; Leighton, 1969) solar dynamo models there is still no consensus about the locations and mechanisms responsible for these observations.

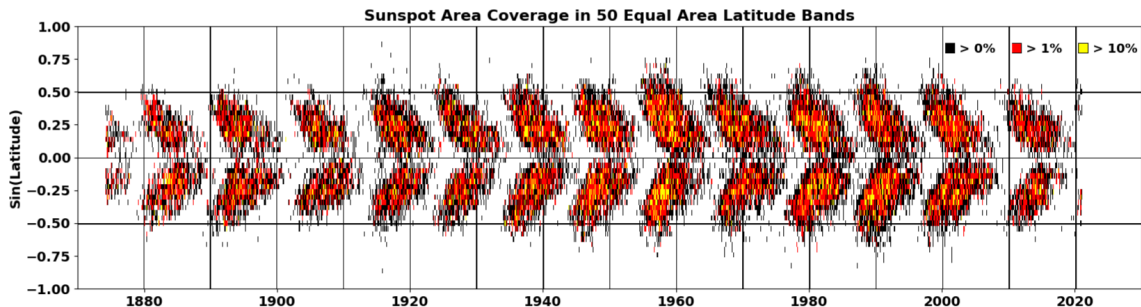


Figure 1.2 The butterfly diagram of sunspots shows their average location in latitude plotted against time, since the first detailed observations in 1874.

Source: Hathaway, 2021, <https://solarcyclescience.com> [accessed on May 1, 2021].

In mean-field dynamo theory, the generation of the toroidal magnetic field is presumed to be dominant in the high shear region at the base of the convection zone, but the location of the α -effect is particularly uncertain. Parker (1955) and Steenbeck et al. (1966) theorized the contribution of the turbulent kinetic helicity, or α -effect, while Babcock (1961) suggested the formation of a near-surface poloidal field due to the diffusive decay of active regions (Subsection 1.1.1). In this scenario the connection with the toroidal field at the base of the convection zone would occur via meridional circulation. This approach found relative success in modeling some of the main characteristics of the solar cycle for profiles of differential rotation, meridional

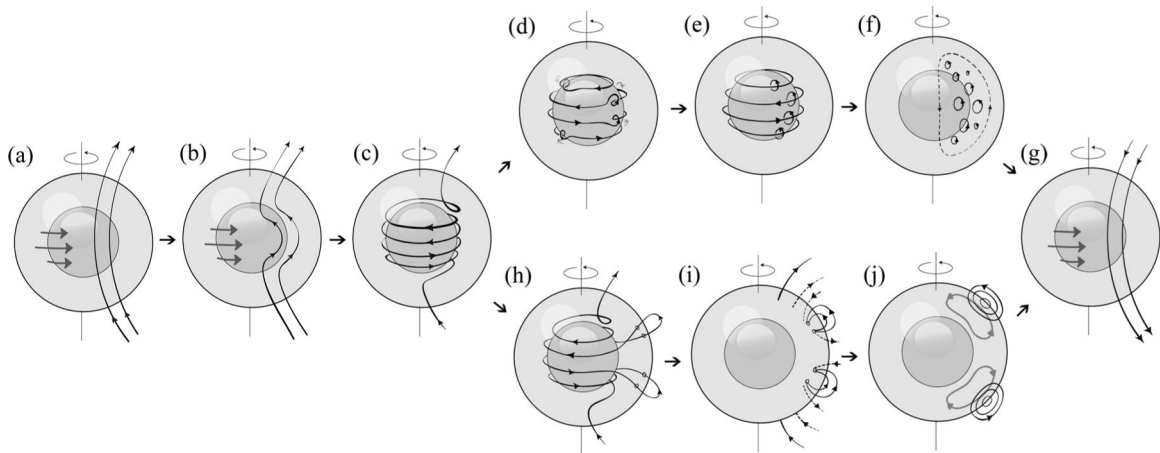


Figure 1.3 A visual representation of the evolution of the solar dynamo. In (a), (b), and (c), the poloidal field is stretched into a toroidal field in the high shear region at the base of the convection zone. (d), (e), and (f) demonstrate the development of the toroidal field back into the poloidal field (g), through the turbulent cyclonic process of the α -effect. (h), (i), and (j) show the development of the poloidal field due to the diffusive decay of active regions in the Babcock-Leighton dynamo mechanism.

Source: adapted from Sanchez et al. (2014).

circulation and the kinetic α -effect (e.g., Dikpati & Charbonneau, 1999; Nandy & Choudhuri, 2002). These simulations were performed in one hemisphere and anti-symmetry of the toroidal field across the equator was not explored. An issue of parity, however, resulted when flux-transport dynamo models with both hemispheres were considered. Several alternate theories have been since proposed to address the issue—among which are three hypotheses: placing the α -effect near the base of the convection zone (Dikpati & Gilman, 2001; Bonanno et al., 2002), considering a magnetic diffusivity for the poloidal field two orders of magnitude larger than that of the toroidal field (Chatterjee et al., 2004), and including the contribution of turbulent pumping (Guerrero & de Gouveia Dal Pino, 2008). The first hypothesis has some caveats since the strong toroidal field in the region would normally quench kinetic turbulent action. Nevertheless, the development of buoyant or magneto-shear instabilities in this region may circumvent the problem, providing a different source for the α -effect (Dikpati & Gilman, 2001). By using the test-field method to explore

the non-linear behavior of turbulent coefficients in simplified flows, Karak et al. (2014) found that the quenching of turbulent diffusivity is isotropic, i.e., the same for all field components. Even though the conditions in the test-field models differ from the solar interior, the second hypothesis seems unrealistic in view of these results. The third hypothesis is still feasible, however, it is hard to predict the amplitudes and profiles of the turbulent transport coefficients.

1.1.1 Active regions

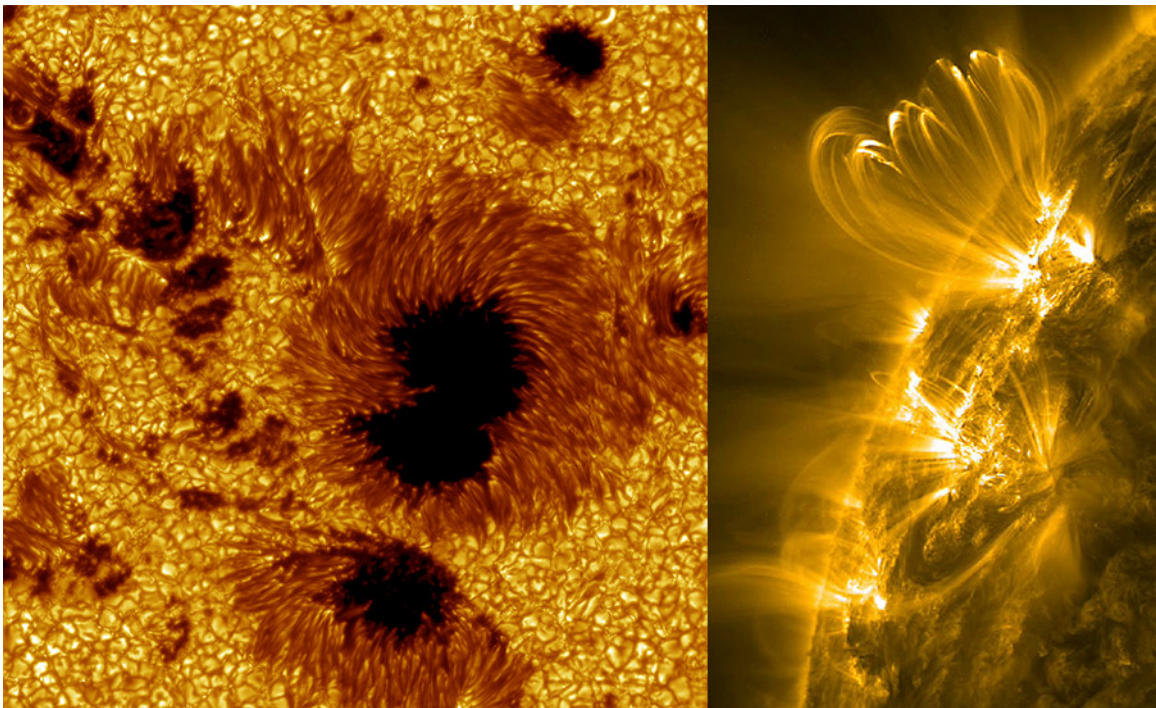


Figure 1.4 An active region as viewed by the 1-meter Swedish Solar Telescope (left, Scharmer et al. (2003)) and the Solar Dynamics Observatory (right, see Subsection 1.2.1).

Source: <https://scied.ucar.edu/sun-active-region> [accessed on May 1, 2021].

Active regions are the surface manifestations of the global solar magnetic field. Toroidal magnetic flux tubes are assumed to rise from the base of the convection zone to the surface via magnetic buoyancy and solar convection (Parker, 1955). As flux

tubes hit the photosphere, they begin to emerge onto the solar surface as magnetic elements of positive and negative polarities. If the magnetic flux in the region is strong enough ($> 10^{20}$ Mx) they begin to form sunspots, otherwise they will remain as “ephemeral active regions” (Harvey & Martin, 1973). Strong active regions are often associated with the rise of arch filament systems (AFS), or magnetic loops pushed into the corona by the undular mode of the Parker instability (Parker, 1979; Shibata et al., 1989). Magnetic reconnection in these regions can often result in the abrupt release of energy in the form of solar flares or coronal mass ejections (CMEs) (see Toriumi & Wang, 2019).

Techniques in local helioseismology (see Subsection 1.2.1) have been used to probe subsurface regions in an attempt to observe flow fields in the presence of emerging magnetic structures (Kosovichev, 2009; Kosovichev et al., 2018), with Ilonidis et al. (2011) demonstrating that a signal can be detected for up to one or two days before the emergence of the region onto the solar surface.

1.2 Solar Dynamics

Internal solar dynamics describe the complex structure of plasma flows in the convective interior of the Sun, which act to generate and regulate the solar dynamo. The two main global regimes of these flows are characterized by differential rotation (Subsection 1.2.2) and meridional circulation (Subsection 1.2.3). The most effective tool to observe the action of these flows directly in the solar interior is through the lens of helioseismology, as described in Subsection 1.2.1.

1.2.1 Helioseismology

Helioseismology has evolved into one of the pillars of heliophysics ever since 5-minute oscillations were first measured on the solar surface nearly 60 years ago (Leighton et al., 1962; Claverie et al., 1979). The interior of the solar convective zone forms a

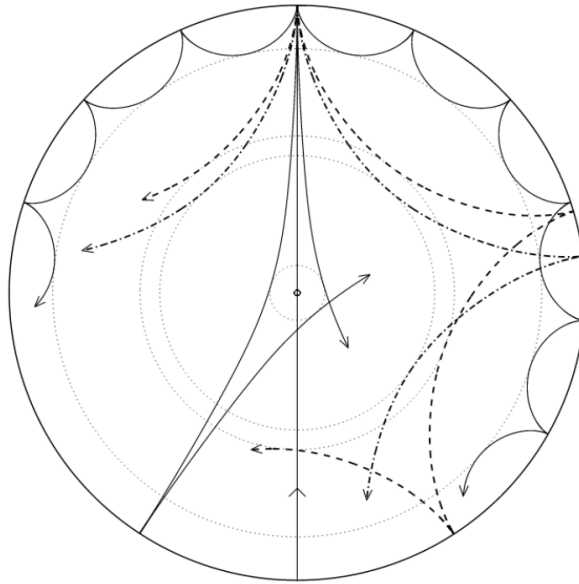


Figure 1.5 A representation of the path of acoustic rays traveling through the solar interior.

Source: adapted from Christensen-Dalsgaard (2014).

resonant cavity for acoustic waves called “p-modes”. These acoustic modes are a rich source of information—allowing for some of the most precise measurements of internal solar dynamics that are currently available. They have become an indispensable tool in measuring internal solar rotation (Duvall et al., 1984; Schou et al., 1998; Howe et al., 2011) as well as meridional circulation (Giles et al., 1997; Zhao & Kosovichev, 2004). Comprehensive overviews on the application and history of global and local helioseismology techniques can be found in Christensen-Dalsgaard (2002); Di Mauro (2003); Gizon & Birch (2005).

The Michelson Doppler Imager (MDI) (Scherrer et al., 1995) of the Solar and Heliospheric Observatory (SOHO) (Domingo et al., 1995), its successor—the Helioseismic and Magnetic Imager (HMI) (Scherrer et al., 2012) aboard the Solar Dynamics Observatory (SDO) spacecraft (Pesnell et al., 2012), as well as the Global Oscillation Network Group (GONG) (Harvey et al., 1996) have been instrumental in

providing the long-term observational Doppler data needed to analyze these internal flow structures using helioseismology techniques.

1.2.2 Differential rotation

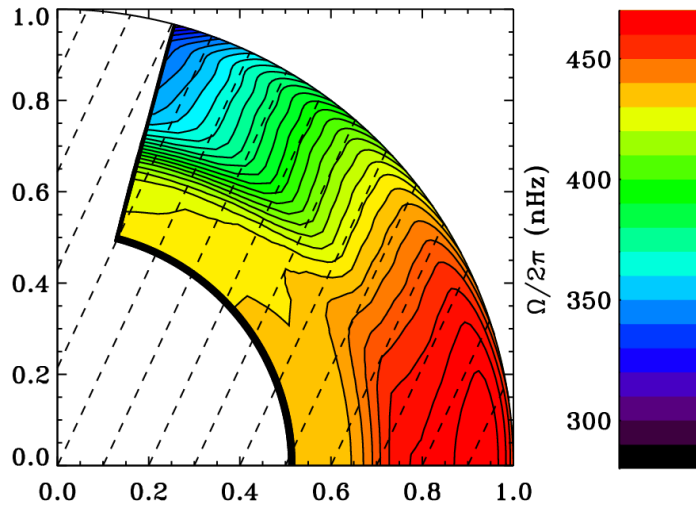


Figure 1.6 The contour of rotational frequency in the Sun. The profile of differential rotation shows a substantial acceleration near the equator, within the convection zone. *Source: adapted from Matilsky et al. (2020).*

Solar rotation is a deceptively complex part of interconnected flow structure throughout the Sun’s interior. Understanding the global interplay of the variation in rotation rates is vital to creating accurate mean-field models of the solar dynamo and flow dynamics (Kitchatinov, 2013). The solar surface shows a pattern of differential rotation (Snodgrass & Ulrich, 1990) which varies from its period at the equator (~ 24 days) to near the poles (~ 30 days). This pattern is mimicked throughout the convective interior (upper 30% of the solar radius), with a slight maximum in the velocity of subsurface layers ($\sim 0.95R_{\odot}$). These rates begin to converge at the interface between the radiative and convective layers (the “tachocline”, see Kosovichev (1996)) where the differential rotation is coupled to a solid core rotating at rate of ~ 430 nHz. Helioseismology has offered a wealth of information about solar rotation,

however, uncertainties remain in inversion results near the poles. Disagreement can be seen between measurements from GONG, MDI and HMI (Schou et al., 2002; Howe et al., 2011); the recent Solar Orbiter mission (Müller et al., 2020), however, hopes to provide observational data that can help address these discrepancies. The rotation rate of the solar core also remains a mystery, with measurements of low-degree modes ($l = 1 - 4$) ranging from significantly lower rates (BiSON, Chaplin et al. (1996)) to much higher ones (IRIS, Lazrek et al. (1996)). Recent measurements of internal gravity modes or “g-modes” have also implied rotation rates more than twice as fast as previous estimates (Fossat et al., 2017).

1.2.3 Meridional circulation

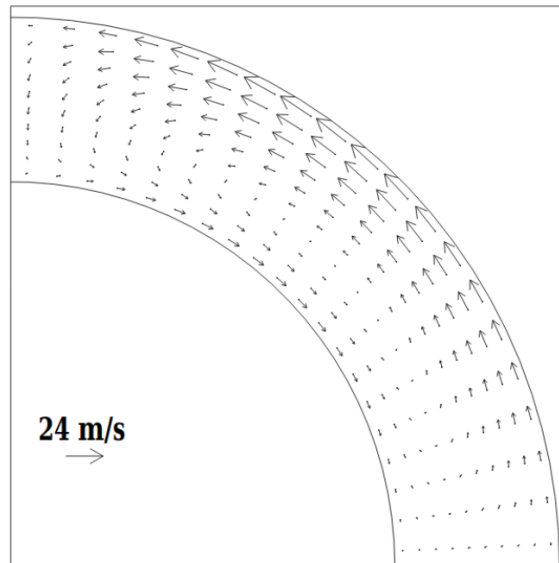


Figure 1.7 A simple model of meridional circulation in the convection zone, consistent with the continuity of mass flows in the Sun.

Source: adapted from Giles (2000).

Meridional circulation is characterized by poleward flows (20 m s^{-1}) in each hemisphere, seen in the Doppler measurements of the solar surface (Duvall, 1979; Hathaway, 1996; Ulrich, 2010). These mass flows operate as large circulation cells, redistributing angular momentum and magnetic flux (Hathaway et al., 2003)

throughout the convective interior. Local helioseismology techniques (Christensen-Dalsgaard, 2002; Gizon & Birch, 2005) have been an indispensable tool with which to probe the structure of these flows, providing consistent measurements of subsurface layers ($> 0.96R_{\odot}$) (e.g., Giles et al., 1997; Zhao & Kosovichev, 2004; Komm et al., 2015; Jackiewicz et al., 2015; Bogart et al., 2015; Böning et al., 2017; Lin & Chou, 2018). Attempting to resolve deeper structures, however, has been much more difficult.

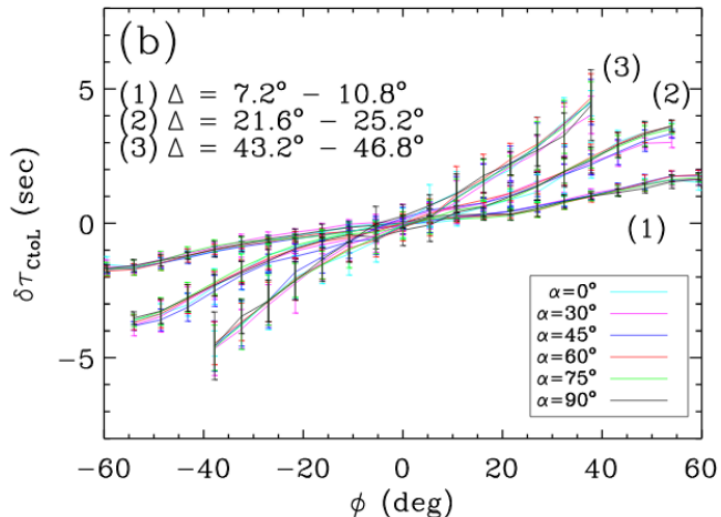


Figure 1.8 Travel-time differences in the cross-correlation of acoustic oscillations (see Section 4.2 for more details), demonstrating the systematic center-to-limb effect, where ϕ is the distance from the center of the observed solar disk. Δ represents ranges of acoustic ray travel distance along the solar surface and α is the angle from a horizontal line drawn through the disk center.

Source: adapted from Chen (2019).

Measurements can be affected by systematic errors, such as center-to-limb (CtoL) variations in travel-time measurements (Zhao et al., 2012; Chen, 2019). This systematic error is an order of magnitude larger than travel-time differences due to meridional circulation, making it difficult to minimize errors when attempting to remove it. The basis of this effect is poorly understood—potentially considered to be a result of projection effects decreasing the resolution near the limb. Analyzing simulated foreshortening on remapped HMI data, however, has shown that this is

most likely not the case (Zhao et al., 2016). Baldner & Schou (2012) suggested that near-surface convection may cause a phase shift in acoustic modes, varying with the line-formation height. A detailed analysis of the effect of granulation on acoustic modes was made by Schou (2015), measuring a strong correlation, although a full quantitative characterization of the effect has yet to be achieved. Removing it from measurements of meridional circulation is a difficult task, however, new empirical approaches in disentangling the error using frequency-dependent analysis have shown some success (e.g., Chen & Zhao, 2018; Rajaguru & Antia, 2020).

Another significant systematic error results from the interference of what appear to be effective downflows in surface magnetic regions (see Liang & Chou (2015)). These regions can be masked out (Liang & Chou, 2015; Chen & Zhao, 2017, 2018; Lin & Chou, 2018; Chen, 2019; Gizon et al., 2020), however, this results in a reduction of available observational data. Drawing meaningful conclusions from smaller samples can often be difficult as weak flows deep in the solar interior are obscured by a realization noise (Gizon & Birch, 2004), resulting from the turbulent nature of convection near the solar surface.

There is currently no consensus on the exact structure and location of the return flow of meridional circulation. Although historically thought to sit at the base of the tachocline ($\sim 0.72 R_{\odot}$, see Giles (2000)), recent estimates show a much shallower return flow (from ~ 40 to ~ 70 Mm in depth; Mitra-Kraev & Thompson (2007); Hathaway (2012), respectively). Double- or multi-cell models have also been proposed from analysis of MDI, HMI, and GONG data (Zhao et al., 2013; Schad et al., 2013; Kholikov et al., 2014; Böning, 2018; Lin & Chou, 2018; Chen, 2019). Similar results can be seen in numerical, convectively driven, magnetohydrodynamic (MHD) and hydrodynamic (HD) simulations (Brun & Toomre, 2002; Miesch et al., 2006; Guerrero et al., 2013; Matilsky et al., 2019). Recent analysis of MDI and GONG data, however, has reasserted the single-cell structure (Gizon et al., 2020), typically employed by

mean-field models of the Sun (Rempel, 2005; Hotta & Yokoyama, 2011; Küker et al., 2011; Kitchatinov, 2013) and other late-type stars (Kitchatinov & Olemskoy, 2012).

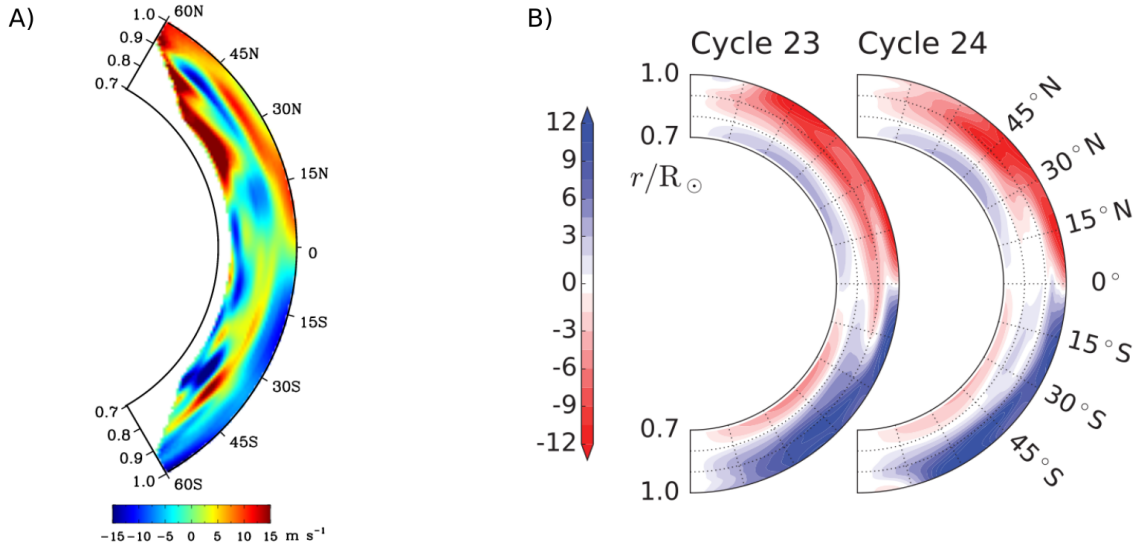


Figure 1.9 The latitudinal velocities (u_{θ} in m s^{-1}) that characterize meridional circulation. A) Inversion results of HMI data, implying a two-cell structure.

Source: adapted from Zhao et al. (2013).

B) Inversion results of MDI and GONG data, implying a one-cell meridional structure.

Source: adapted from Gizon et al. (2020).

The convectively-driven hydrodynamic models of Guerrero et al. (2013); Gastine et al. (2014); Käpylä et al. (2014); Featherstone & Miesch (2015) explore single/multi-cell circulation regimes constrained by anti-Solar and Solar profiles of differential rotation. In these models, non-diffusive turbulent Reynolds stresses, or “gyroscopic pumping” (the Λ -effect, Ruediger (1989); Kitchatinov & Rudiger (1993)), play a critical role connecting angular momentum transport to transitions between meridional circulation regimes (Kitchatinov, 2013). Altering the direction of the Λ -effect directly (Bekki & Yokoyama, 2017) has been shown to form counter-rotation cells in the lower convection zone; Pipin & Kosovichev (2018) demonstrate that radial variations of the Coriolis number near the tachocline can be a potential physical source of this sign inversion.

1.3 Global Modeling - Overview and Motivation

Global modeling has played a key role in exploring the interactions of differential rotation, meridional circulation, and the solar dynamo in chaotic interconnected systems. Without the ability to observe the solar interior directly, 3D models generate a laboratory environment that can be used to recreate and better understand the complex dynamics that characterize the Sun’s internal structure. The work presented in this dissertation focuses on the results and implications of global magnetohydrodynamic (MHD) modeling (Subsection 1.3.1) as well as the eventual need for more dynamic models with a greater range in simulation regimes—motivating the development of a new global linear model (Subsection 1.3.2) that will become a basis for future investigations.

1.3.1 MHD modeling

Non-linear global convectively-driven magnetohydrodynamic (MHD) modeling has attempted to answer some of the outstanding questions on the nature of the solar cycle by incorporating realistic conditions of observable solar parameters in simulations of internal solar dynamics (Brun et al., 2004; Ghizaru et al., 2010; Racine et al., 2011; Cossette et al., 2013; Nelson et al., 2013; Augustson et al., 2015; Guerrero et al., 2016; Cossette et al., 2017; Warnecke, 2018; Guerrero et al., 2019). Even though there has been enormous progress since the seminal work of Gilman & Miller (1981), models are not yet able to successfully reproduce many solar cycle properties; migration patterns of the surface field as well as the non-axisymmetric dynamo coupled with solar-like differential rotation and meridional circulation has yet to be naturally simulated in a satisfactory way. Recently, it has become apparent that limiting the simulated domain to the convective interior may be insufficient, with Guerrero et al. (2016) demonstrating the substantial effect of the tachocline layer on the long-term evolution of the magnetic solar cycle. The addition of this

sub-adiabatic region under the convection zone sees a dramatic increase in the period of the dynamo cycle, pushing it from a time-frame of years (see also Augustson et al., 2015; Warnecke, 2018) to that of decades, storing a strong oscillatory magnetic field below the tachocline. The work presented in this dissertation focuses on the extension of various regimes of the same model (EULAG-MHD, see Section 2.1) to the solar surface, where the beginnings of a near-surface shear layer (NSSL) can be seen in higher Rossby number regimes. High levels of shear are instrumental in generating large-scale toroidal fields, seen dominating the surface and the base of the tachocline in previous models (Guerrero et al., 2016). These simulations exhibit solar cycles that strongly rely on varying regions of shear as well as turbulent helicities to generate large-scale poloidal fields. The structure of the subsurface rotational shear plays a key role in shaping the emergence of the solar magnetic field in the form of the butterfly diagram (Brandenburg, 2005), and introducing changes to this subsurface boundary layer appears to modify the parity of the solution.

Global convectively driven MHD models focus on the incompressible region of the convection zone, omitting many important physical consequences of compressibility in the overshoot layer underneath the tachocline, as well as near-surface regions. An extension of these models is necessary for the next generation of global simulations to faithfully reproduce features of the solar cycle. In the following section (Subsection 1.3.2), the formulation and use-case is presented for a new linear compressible model, whose computational techniques will become the basis for future investigations in the development of a compressible non-linear convectively-driven MHD model.

1.3.2 Acoustic modeling

A complete picture of mass flows inside of the Sun continues to be elusive. In order to raise the reliability of inferences made through helioseismology, further

constraints on the understanding of inversion results are necessary. The application of “forward-modeling” presents an opportunity to test helioseismology techniques under tightly controlled approximate solar conditions. Since the seminal work of Jensen et al. (2003), numerical acoustic solar models have been used to simulate subsurface sound speed perturbations (Parchevsky & Kosovichev, 2007; Parchevsky et al., 2014). Three-dimensional (3D) cartesian models of the solar atmosphere have been employed to validate local time-distance measurements in regimes of convection (Braun et al., 2007) and magnetic fields (Cameron et al., 2008; Khomenko et al., 2009; Parchevsky & Kosovichev, 2009; Felipe et al., 2016). The need to simulate larger interconnected hydrodynamic structures led to the development of global spherical models (Hanasoge et al., 2006, 2007; Hartlep et al., 2008, 2013; Papini et al., 2015; Gizon et al., 2017) that have been integral in validating inversion techniques. Global acoustic codes can be used to simulate large numbers of varying structures, providing a baseline for expected travel-time difference measurements. Such models (Hartlep et al., 2013) have been used in conjunction with inversion techniques in order to support inferences of a double-cell meridional structure (Zhao et al., 2013; Chen, 2019) from HMI observations, as well as more recent reassertions of the single-cell model (Gizon et al., 2020) on MDI and GONG data.

Such discrepancies present a clear role for forward-modeling to play in outlining the boundaries of possible inferences from helioseismology techniques. A detailed systematic examination of a variety of meridional circulation profiles is required to constrain interpretations made from observations. In order to address some of these issues, as well as to set up a foundation for future investigations, this dissertation presents the formulation and application of the GALE (Global Acoustic Linearized Euler) code. This efficient and flexible pseudo-spectral algorithm computes stochastically excited oscillations over a wide range of static or dynamic 3D background velocity fields—mimicking the effect of realization noise seen in obser-

vations. Important insights can be made by simulating acoustic interactions with profiles of meridional circulation and differential rotation coupled together using mean-field or MHD/HD models. These simulations can be used as a tool to lend confidence to various inferences made through helioseismic inversions (Kitchatinov, 2013), as well as aid in the analysis of systematic errors. The physical basis of the CtoL effect (described in Subsection 1.2.3) remains a mystery, however, such acoustic models provide the flexibility to test effects of projection, as well as allow for the sampling of velocity perturbation at arbitrary heights in the model atmosphere, under the effect of near-surface models of convection.

1.4 Outline

This dissertation focuses on the presentation of two main subjects: global MHD modeling and global acoustic modeling. An overview of these models, results from their analyses, and discussions of their impacts on the current state of solar physics are organized as follows.

Chapter 2 contains the formulation of the EULAG-MHD code (Section 2.1). This chapter presents an analysis of the extension of global anelastic MHD models towards near-surface layers, exploring the substantial impacts of altering profiles of convection and shear on the parity of the global dynamo (Section 2.3). A discussion of the implications of these results and the future of global MHD modeling is presented in Section 2.4.

Chapter 3 contains the numerical formulaion and computational set-up of the GALE code. An overview and derivation of the governing equations is presented in Sections 3.1 and 3.2, respectively. Section 3.6 contains the numerical method employed in the computation of the governing equations, including the pseudo-spectral formulation, discretization methods, numerical solvers, and the parallelization technique used for distributed computing. A validation of the

computational methods can be found Section 3.7, reproducing the solar power spectrum, measuring frequency splittings due to differential rotation, as well as a power-map analysis of sound speed perturbations.

Chapter 4 focuses on the helioseismic analysis of radial velocity perturbations generated by the GALE code. The local helioseismology technique of deep focusing, used to infer internal background flows in the model, can be found in Section 4.2. This chapter explores the application of the GALE code in a forward-modeling capacity, testing the helioseismic signatures of various profiles of meridional circulation generated by physics-based mean-field models. An analysis of the difference between signatures of single-cell and double-cell meridional circulation as well as the effect of realization noise on the ability to distinguish between these regimes can be found in Section 4.4

Chapter 5 contains a substantive discussion of the results presented in this dissertation, along with their implications on the current state of solar modeling for both non-linear and acoustic global algorithms. Section 5.3 describes future plans for the GALE code, including a derivation of a linearized MHD extension (Subsection 5.3.1) which will be used to model the helioseismic signatures of internal magnetic structures. The details on the development of a fully non-linear compressible MHD model, employing the computational techniques used in the GALE code, can be found Subsection 5.3.2.

Appendix A presents a derivation of the vector spherical harmonic (VSH) and tensor spherical harmonic (TSH) coordinate bases used in the pseudo-spectral formulation of the governing equations in the GALE code. The definition of the divergence and curl of vector and tensor spherical harmonics can be found in Section A.4 and Section A.5, respectively.

Appendix B contains the definitions of the recursion relations used to compute functions in the frequency space of the spherical harmonic decomposition. Relations

derived for trigonometric functions can be found in Subsection B.2.1, and for transverse derivatives along the model surface in Subsection B.2.2.

CHAPTER 2

GLOBAL MHD MODELING WITH EULAG

2.1 Model Description

EULAG-MHD (Smolarkiewicz & Charbonneau, 2013) is the magnetohydrodynamic extension of the hydrodynamic model EULAG (EULerian/semi-LAGrangian fluid solver) predominantly used in atmospheric and climate research (Prusa et al., 2008). It is a versatile numerical solver, well adapted to simulating high-Reynolds number anelastic flows found in the majority of the solar interior. EULAG is powered by a nonoscillatory forward-in-time MPDATA method (Multidimensional Positive Definite Advection Transport Algorithm; see Smolarkiewicz (2006) for an overview)—a nonlinear second-order-accurate iterative implementation of the elementary first-order-accurate flux-form upwind scheme.

The leading truncation terms of MPDATA have been shown to act as an effective subgrid-scale (SGS) turbulence (Smolarkiewicz & Prusa, 2002). Typically, solar modeling has relied on explicit SGS turbulence models to simulate the transfer and dissipation of energy below the inertial subrange, such as the large eddy simulation (LES) model (Lilly, 1966). A newer class of LES methods has also been implemented with the dynamic Smagorinsky model (Germano et al., 1991; Nelson et al., 2013; Wray et al., 2015), increasing the accuracy of turbulent dissipation calculations. EULAG offers an alternative to these classic methods by exploiting the so-called “implicit large eddy simulation” (ILES) approach (Grinstein et al., 2007), which achieves a similar goal while obviating the need for evaluating higher-order differential operators. Other nonoscillatory advection schemes possess the ILES property, and generally have proven to be effective through a large range of scales and physical scenarios, from laboratory to stellar (Grinstein et al., 2007). In contrast to the prescription of

filter length scales in classic LES, the MPDATA-based ILES is parameter free and adaptive to the regularity of the solution (Margolin et al., 2006), within the scales of the grid resolution (Margolin et al., 2002; Domaradzki et al., 2003; Kühnlein et al., 2019). ILES has been applied in EULAG in order to model global solar convection, comparing results with explicitly filtered spectral methods (Elliott & Smolarkiewicz, 2002). EULAG has been tested for various solar regimes, reproducing hydrodynamic effects observed on the Sun, such as breaking the Taylor-Proudman balance, as well as inducing differential rotation (Guerrero et al., 2013). This model has been augmented for simulating the global solar magnetic dynamo in EULAG-MHD (Smolarkiewicz & Charbonneau, 2013), adding an ideal MHD component, and employing it in the study global magnetic dynamics (Ghizaru et al., 2010; Racine et al., 2011).

EULAG-MHD is described in full detail by Smolarkiewicz & Charbonneau (2013), and its conservative properties are thoroughly discussed by Cossette et al. (2017). This section (Section 2.1) will only briefly summarise the mathematical formulation and specific setup, following Guerrero et al. (2016). The governing equations (Equations (2.1)-(2.4)) assume the anelastic formulation of Lipps & Hemler (1982). They are solved in a global spherical shell $0 \leq \phi \leq 2\pi$, $0 \leq \theta \leq \pi$, from the radiative interior at $0.61R_\odot$ to the surface at $0.97R_\odot$. The grid resolution $128 \times 64 \times 64$ in ϕ , θ and r , respectively, corresponds to that of previous long-term EULAG-MHD simulations of stellar climates (Guerrero et al., 2013, 2016). The governing equations are:

$$\nabla \cdot (\rho_s \mathbf{u}) = 0 , \quad (2.1)$$

$$\frac{D\mathbf{u}}{Dt} + 2\boldsymbol{\Omega} \times \mathbf{u} = -\nabla \left(\frac{p'}{\rho_s} \right) + \mathbf{g} \left(\frac{\Theta'}{\Theta_s} \right) + \frac{1}{\mu_0 \rho_s} (\mathbf{B} \cdot \nabla) \mathbf{B} , \quad (2.2)$$

$$\frac{D\Theta'}{Dt} = -\mathbf{u} \cdot \nabla \Theta_e - \frac{\Theta'}{\tau} , \quad (2.3)$$

$$\frac{D\mathbf{B}}{Dt} = (\mathbf{B} \cdot \nabla) \mathbf{u} - \mathbf{B} (\nabla \cdot \mathbf{u}) . \quad (2.4)$$

In Equations (2.1)-(2.4), $D/Dt = \partial/\partial t + \mathbf{u} \cdot \nabla$, where \mathbf{u} denotes the flow velocity, and $\boldsymbol{\Omega} = \Omega_0(\cos \theta, -\sin \theta, 0)$ is the angular velocity of the rotating reference frame ($\Omega_0 = 2.6 \times 10^{-6}$). p and Θ mark pressure and potential temperature, with the latter essentially equivalent to the specific entropy of an ideal gas via $ds = c_p d \ln \Theta$ where c_p is a specific heat at constant pressure. Primes refer to perturbations about a static ambient state assumed to satisfy the generic Lipps-Hemler equations, an asymptotic expansion about the hydrostatic isentropic background state (denoted by the subscript “s”) under gravitational acceleration $\mathbf{g} \propto r^{-2}$; see Cossette et al. (2017) for a substantive discussion. The evolution of the magnetic field, \mathbf{B} , is governed by the induction equation (Equation (2.4)) in the classic ideal MHD limit, where the momentum equation (Equation (2.2)) includes the magnetic tension ($\mu_0^{-1}(\mathbf{B} \cdot \nabla)\mathbf{B}$) portion of the Lorentz force, with the magnetic pressure subsumed in p' (Smolarkiewicz & Charbonneau, 2013). The explicit viscous tensor and the magnetic dissipation term are disregarded in favor of the ILES dissipative action of MPDATA (Ghizaru et al., 2010).

In this formulation, convection is primarily driven by the advection of a non-isentropic ambient potential temperature (Θ_e , Equation (2.3)). This ambient state can be used to create super-adiabatic entropy gradients that simulate heat flux from the bottom boundary. If left to evolve naturally, convection will tend to balance out any entropy gradient in the ambient state. To offset fluid homogenization, the Newtonian cooling term (second term on the right hand side (RHS) of Equation (2.3)) relaxes potential temperature perturbations to zero, driving the system towards a balanced statistical equilibrium. In these simulations, the timescale of the relaxation is set at $\tau = 1.036 \times 10^8 \text{ s} \approx 3.3 \text{ yr}$, a value that is compatible with the solar rotation rate (Guerrero et al., 2016). This timescale is sufficiently short, so that any explicit effects of heat diffusion or radiative heat transfer can be omitted in global energetic balance considerations (Cossette et al., 2013). The boundary conditions are

impermeable and stress-free for the velocity field and stop the radial flux of potential temperature perturbations. The magnetic field is assumed to be entirely radial at both boundaries.

2.2 Modifying the NSSL

The ambient state is computed for the polytropic stratification of an ideal gas under hydrostatic equilibrium,

$$\begin{aligned}\frac{\partial T_e}{\partial r} &= -\frac{g}{R(m+1)}, \\ \frac{\partial \rho_e}{\partial r} &= -\frac{\rho_e}{T_e} \left(\frac{g}{R} - \frac{\partial T_e}{\partial r} \right),\end{aligned}$$

where R is the specific gas constant and $m(r)$ is the polytropic index function, set to force entropy gradients in the model. A full review of this ambient state is presented by Guerrero et al. (2013).

Previous works with EULAG-MHD (Guerrero et al., 2016, 2019) have shown the effect that the tachocline has on global solar models. This layer of shear at the radiative boundary begins to play a fundamental role in the storage and generation of the global magnetic field, going as far as significantly altering the time-scale of the solar cycle by decades. Another interesting development in these simulations is the formation of a near-surface shear layer (NSSL) in models with different rotational periods. In these previous works, the characteristics of convective motions were solely defined by this rotational period.

Forcing the formation of a NSSL allows for a more in-depth study of the global impacts of this boundary layer. This section details the profile of several simple functions of thermodynamic ambient states that generate diverse regimes of near-surface convection. Simple models of convective acceleration and deceleration offer the chance to explore the contribution of near-surface stratification to the global

distribution of angular momentum and the evolution of magnetic solar cycles. To that end, the three following models are employed (simulations ns1, ns2 and ns3), each having three distinct global layers: the radiation zone, convection zone, and the near-surface boundary layer. This is done using a polytropic index function with two step functions and three polytropic indices (m_{rz} , m_{cz} , and m_{ns}), respectively representing the aforementioned layers;

$$m(r) = m_{rz} + \frac{m_{cz} - m_{rz}}{2} \left[1 + \operatorname{erf} \left(\frac{r - r_{tac}}{w_t} \right) \right] + \frac{m_{ns} - m_{cz}}{2} \left[1 + \operatorname{erf} \left(\frac{r - r_{ns}}{w_{ns}} \right) \right].$$

The radial position of the tachocline is set at $r_{tac} = 0.72R_{\odot}$ and the transition width is $w_t = 0.015R_{\odot}$. The radiative interior index is set to $m_{rz} = 2$, creating a strongly stable subadiabatic layer; the convection zone index is set to $m_{cz} = 1.499978$ to simulate a slightly superadiabatic convective envelope. The near-surface step is centered at $r_{ns} = 0.95R_{\odot}$ with a transition width of $w_{ns} = 0.015R_{\odot}$. Three different near-surface convection profiles are used, with polytropic indices: $m_{ns1} = 1.499975$, $m_{ns2} = 1.5$, and $m_{ns3} = 1.8$. The graph of the resulting potential temperature profiles for the three ambient states is shown in Figure 2.1.

In the first model (ns1), an ambient state of slightly increased convective strength was implemented, enhancing less rotationally constrained motions near the surface and inducing the formation of a well defined near-surface shear layer. The second case, ns2, exhibits a surface entropy gradient of a hydrostatic polytrope at the edge of a stable non-convective profile ($m = 1.5$). This profile is not strong enough to fully suppress convection, but it does decrease the velocity gradient of flows near the surface. In the last simulation, ns3, a stable subadiabatic layer is created, decreasing convective motions in a low density region. This mimics a vacuum boundary for the magnetic field near the surface; a regime previously tested by Warnecke et al. (2013). The models are all started with an unmagnetized ambient state and are initiated with

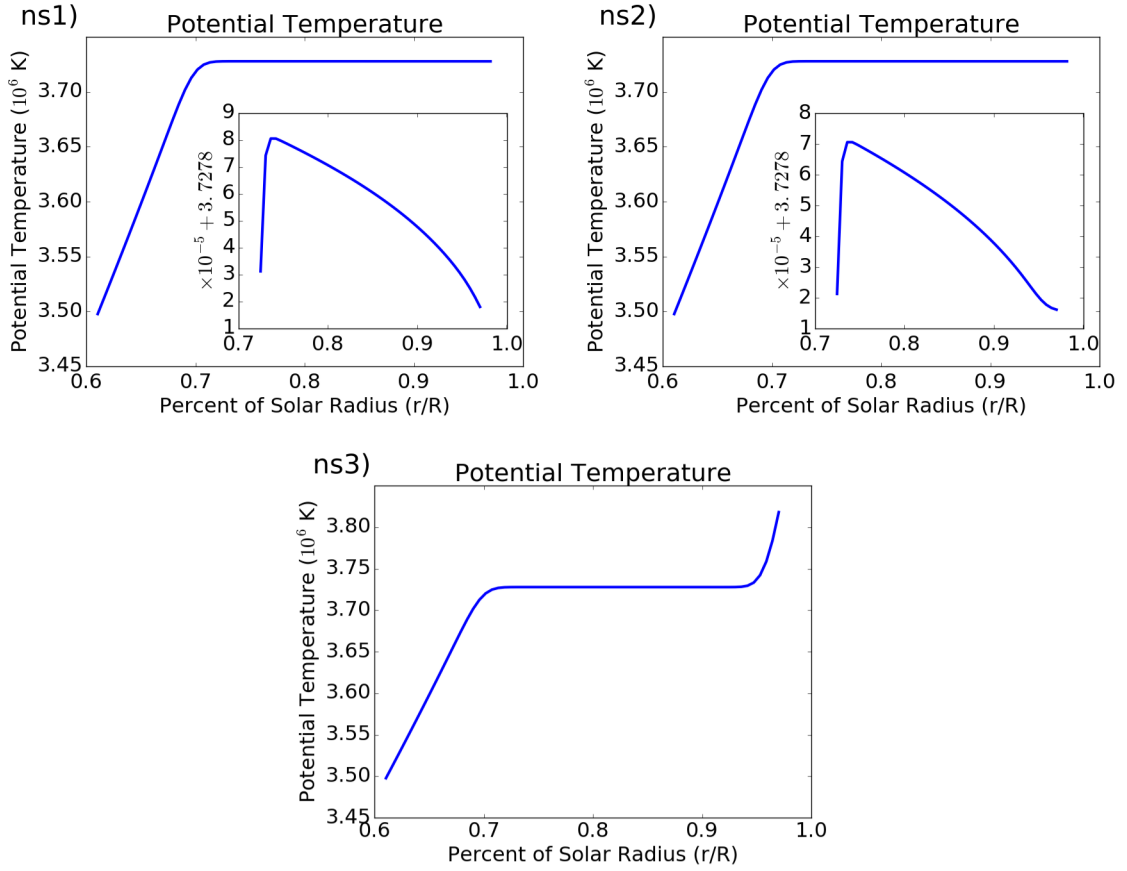


Figure 2.1 Profiles of ambient states of the potential temperature (Θ_e) for simulations: ns1, ns2, and ns3. In ns1, $m_{ns1} = 1.499975$, slightly increasing convection near the surface. In ns2, $m_{ns2} = 1.5$, the super-adiabatic zone is slightly altered to decrease the rate of convection. Finally, in ns3, $m_{ns3} = 1.8$. In this case convection is suppressed at the surface.

Source: adapted from Stejko et al. (2020).

the same set of random white noise as well as perturbations of potential temperature and divergence-free velocity. The models are evolved until the dependent variables reach a statistically stable equilibrium.

2.3 Results

Each simulation is evolved for several hundred years, after which the last three polarity reversals are analyzed with oscillatory periods of the large-scale magnetic field of ~ 30 yrs for ns1, ~ 20 yrs for ns2, and ~ 40 yrs for ns3. Each model develops unique

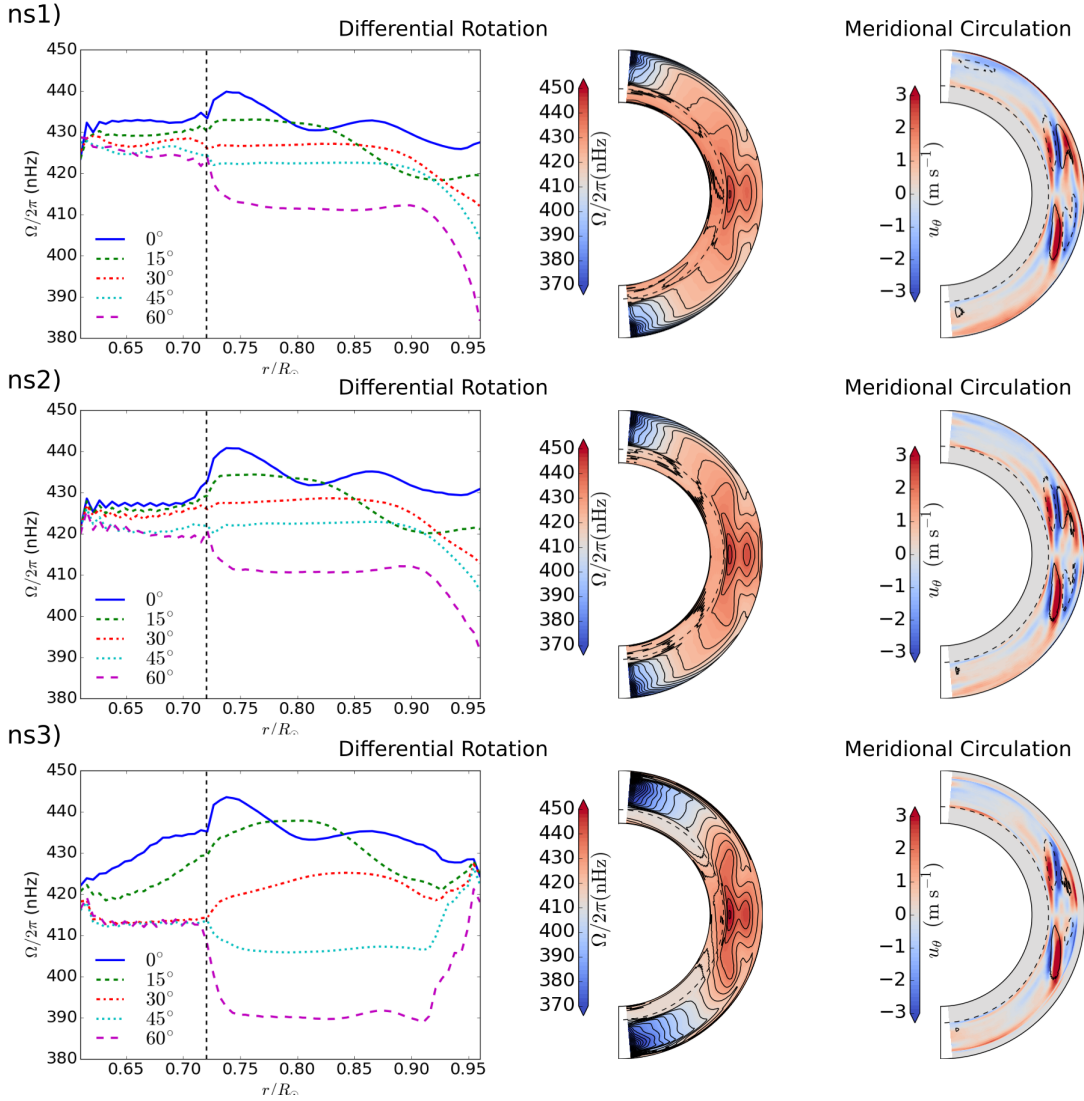


Figure 2.2 The time averaged (over three dynamo cycles) and azimuthally-averaged differential rotation and meridional circulation profiles: ns1, ns2, and ns3, from top to bottom. The left-hand side shows the angular velocity at various latitudes as a function of radius. The center column contains a contour plot of this differential rotation in the meridional plane. The right-hand side shows the meridional circulation in the same plane, where colored contours show the speed of latitudinal flows; the dashed and solid contours outline clockwise and counter-clockwise poloidal circulation.

Source: adapted from Stejko et al. (2020).

rotational hydrodynamic structures and global magnetic profiles; Figure 2.2 presents the time-averaged (over three magnetic cycles) and azimuthally-averaged differential rotation profile along with the meridional circulation.

All three simulations exhibit profiles which appear to be similar to the solar model (RC02), discussed by Guerrero et al. (2016); there are, however, a few notable differences. The effect of suppressed surface convection is immediately obvious in the velocity profile of ns3, where large differences with the other two models begin to develop. A buildup of rotational velocity near the equator can be observed above the tachocline, with less angular momentum being carried into the radiative interior as well as being excluded from the surface. This model also exhibits strong latitudinal variance of rotational frequency, displaying significant gradation in the differential rotation profile—extending well into the radiative interior. The subsurface region of simulation ns3 manifests a strong positive shear, in contrast with the other two models, ns1 and ns2. The most significant differences are found below the tachocline, where angular momentum transfer fails to penetrate, especially at higher latitudes, and maintains the models’ initial rotation rate ($\Omega/2\pi \approx 413$ nHz).

The models of slightly increased (ns1) and suppressed (ns2) convection rates, predictably, look similar, with certain exceptions. The rotation rate of the radiative interior exhibits the greatest differences between the two models, with simulation ns1 reaching an average angular frequency of ~ 430 nHz as compared to ~ 425 nHz of simulation ns2. Significant differences can also be observed in the rate of rotational frequency observed at higher latitudes. Even though these results do not closely match helioseismic inferences of internal solar rotation rates (Schou et al., 1998), the models do show clear conical iso-contours as opposed cylindrical ones, breaking the Taylor-Proudman balance at the upper latitudes. Rotational frequency in the convection zone (Figure 2.2), however, still shows a shallow break in differential rotation near the equator, aligned along the rotational axis.

One of the largest effects of the subsurface acceleration can be seen in its impact on the levels of shear experienced at the tachocline (Figure 2.3), decreasing positive levels of shear near the equator and increasing negative shear near the poles. The

result is a changing focus of the Ω -effect, concentrating greater action into higher latitudes of model ns1.

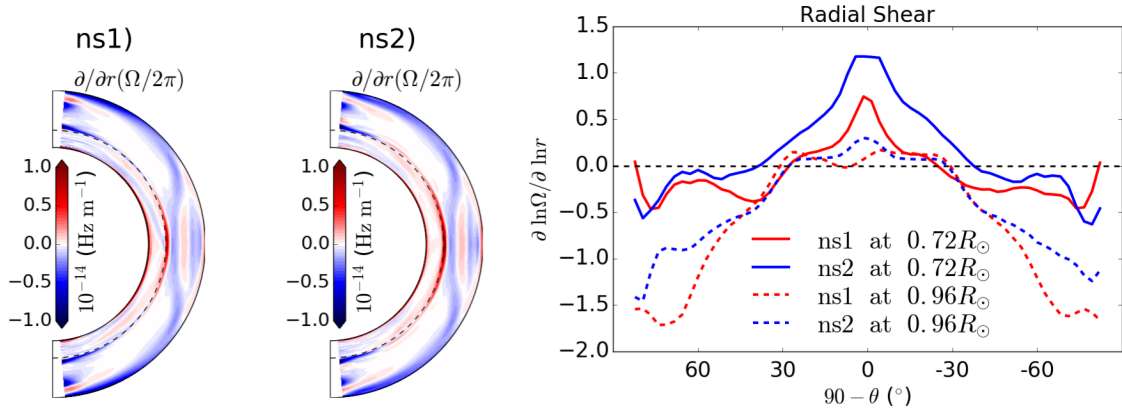


Figure 2.3 Radial shear profiles of simulations ns1 (left panel) and ns2 (middle), characterized by the radial derivative of the angular velocity. The largest noticeable differences are of the shear experienced at the tachocline and at the poles near the surface (right), an effect consistent with the observed differences in the models’ rate of angular momentum distribution into the radiation zone (Figure 2.2).

Source: adapted from Stejko et al. (2020).

The shear profiles of these models (ns1, ns2) are structurally similar to those expected from helioseismic inferences (Schou et al., 1998), with a few significant differences. The bulk of the convection zone contains contours of shear at low latitudes—matching the axis-aligned contour in differential rotation, breaking the conical differential rotational cell seen in Figure 2.2. This is most likely a consequence of the models limited ability to fully break the Taylor-Proudman balance. Near the model surface there is more deviation from observed solar rotation, where a consistent shear ($\partial \ln \Omega / \partial \ln r = -1$) has been observed up to $\sim 60^\circ$ latitude (Barekat et al., 2014). Even though near-surface shear in the ns1 and ns2 models hovers around this value, it begins to diverge at low latitudes—becoming positive (see right panel of Figure 2.3). Such an acceleration has not been observed in recent hydrodynamic simulations of near-surface gradation (Matilsky et al., 2019), where different density contrasts are modeled in an attempt to generate solar-like near-surface shear.

Their model with large density stratification results in negative surface shear at equatorial latitudes. Models ns1 and ns2, in comparison, implement various potential temperature contrasts in the attempt to create rotationally unconstrained flows. Increasing the density contrast might allow this region to break up the axis-aligned structures of shear and induce the development of negative radial shear at equatorial latitudes. These models also do not consider the top 3% of the solar surface—a turbulent region of a large density stratification where the time-scale of convective motions is considerably shorter than that of solar rotation.

An interesting feature is exhibited in model ns1, where the rotation of the radiation zone is not completely hemispherically symmetric, unlike the two others—a possible structural consequence of the differences in the development of their respective dynamo profiles. This effect is also apparent in the distribution of shear (Figure 2.3), which shows a small asymmetrical tilt towards the northern hemisphere.

All three models exhibit a meridional circulation pattern observed in previous EULAG-MHD models (Guerrero et al., 2016). The only noticeable difference is a slight poleward increase in meridional velocity at higher latitudes, primarily on the surface of model ns1. These meridional profiles show the formation of a two cell structure, recently observed by helioseismology (Zhao et al., 2013); these cells are, however, confined to low latitudes and aligned with the rotational axis—similar profiles have been previously observed in other global anelastic models (e.g., Brun & Toomre, 2002; Featherstone & Miesch, 2015; Matilsky et al., 2019).

The perturbative rms velocity ($u'_{rms} = \sqrt{u'_r + u'_\theta + u'_\phi}$) can give some insight into the turbulent structure of the models, shown in Figure 2.4. Model ns3 shows a significant drop in turbulent velocity near the surface, consistent with the strong subadiabatic gradient that was induced. In models ns1 and ns2, the differences are rather small with only the obvious slight changes near the surface. The turbulent u'_{rms} is largely isotropic in these models, with the exception of the region near the surface

where the boundary condition transforms the radial velocity (and its perturbative component) into horizontal flows.

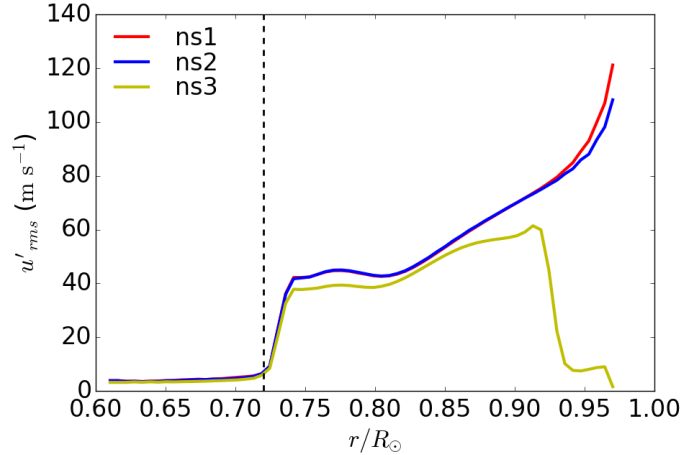


Figure 2.4 Radial profile of the rms velocity (u'_{rms}). Models ns1 and ns2 are very similar, showing an increasing turbulence near the surface. In model ns3, the subadiabatic gradient effectively quenches strong turbulence deep into the convection zone.

Source: adapted from Stejko et al. (2020).

These relatively small differences in convective structures result in large impacts on emerging mean flows and global magnetic fields. The time evolution of the magnetic dynamo over the course of three cycles is shown in Figure 2.5, plotting a cross section of the azimuthally averaged toroidal magnetic field, \overline{B}_ϕ , near the model surface ($\sim 0.95R_\odot$), at the tachocline ($\sim 0.72R_\odot$), as well as a radial cross section at a latitude of 45° .

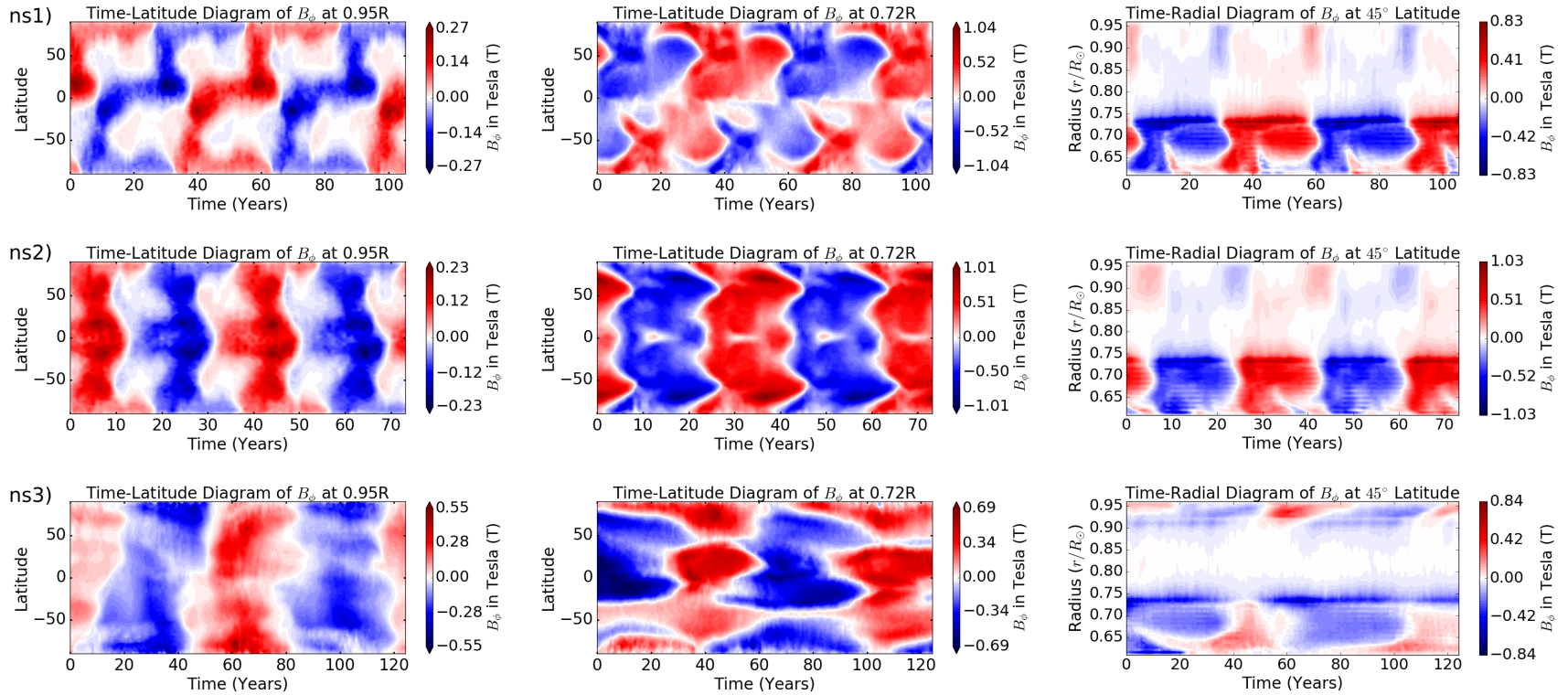


Figure 2.5 The time-latitude diagrams of the magnetic field (B_ϕ measured in Tesla) for simulations ns1, ns2, and ns3 (from top to bottom) at $0.95 R_\odot$ (left) and $0.72 R_\odot$ (center), as well as the time-radius diagram at a 45° latitude (right). ns1) With slightly increased convection, the beginnings of a staggered anti-symmetric magnetic cycle start to form. ns2) The field follows a distinct pattern, but the anti-symmetric nature is lost. ns3) The convection profile is altered such that the field is unstable and non-uniform, but with a well defined cyclical pattern.

Source: adapted from Stejko et al. (2020).

Model ns3 exhibits the largest difference in its profile of polarity reversals, where the pattern of the global magnetic field cannot seem to find a definite symmetric hemispheric structure, as well as exhibiting the longest periodic evolution of its dynamo cycle (~ 40 yrs). Even in the absence of turbulent activity in the upper convection zone, a strong magnetic field is still being generated and stored, loosely connected with strong fields below the tachocline. These fields still undergo regular polarity reversals—but without any defined pattern or symmetric structure. The models with slightly suppressed (ns2) and slightly increased convection (ns1), however, both exhibit regular cyclic patterns, with large differences in the time-scale of their evolution as well as the nature of their symmetries. The toroidal field profile of model ns2 looks similar to the solar model RC02 (with no alterations of the subsurface boundary) described by Guerrero et al. (2016), showing minimal structural effects of its slightly suppressed convective motions. The most significant difference appears to be with the increased convection model (ns1), where the emerging global magnetic field begins to shift from the equatorial symmetry seen in profile ns2 to an offset, staggered near anti-symmetry, exhibiting a more solar-like hemispheric polarity.

2.3.1 Mean-field analysis

An in-depth analysis of the dynamo characteristics that result in the large structural differences in models ns1 and ns2 can be done with a mean-field analysis, starting with the induction equation (Equation (2.4)) rewritten into its mean-field form (Moffatt, 1978),

$$\frac{\partial \overline{\mathbf{B}}}{\partial t} = \nabla \times (\overline{\mathbf{u}} \times \overline{\mathbf{B}} + \overline{\mathcal{E}}), \quad \text{where:} \quad \overline{\mathcal{E}} = \overline{\mathbf{u}' \times \mathbf{B}'}$$

The mean-field terms (denoted by the overline) are averaged over their longitude, with primed terms being the perturbation from this average. Using the first-order smoothing approximation (FOSA), the turbulent induction, $\overline{\mathcal{E}}$ (excluding any triple correlation terms and third-order derivatives), can be written in the manner of Brandenburg & Subramanian (2005), with the turbulent transport coefficients defined as:

$$\begin{aligned} \overline{\mathcal{E}}_i &= (\alpha_k + \alpha_m)\overline{B}_j - \eta_t \frac{\partial \overline{B}_j}{\partial x_k}; & \alpha_k &= -\frac{1}{3}\tau_{corr}(\overline{\boldsymbol{\omega}' \cdot \mathbf{u}'}), \\ & & \alpha_m &= \frac{1}{3}\tau_{corr}(\overline{\mathbf{j}' \cdot \mathbf{B}'}), \\ & & \eta_t &= \frac{1}{3}\tau_{corr}(\overline{\mathbf{u}'^2}), \end{aligned} \quad (2.5)$$

where $\boldsymbol{\omega}' = \nabla \times \mathbf{u}'$ is the turbulent vorticity and $\mathbf{j}' = \nabla \times \mathbf{B}'$ is a perturbation of the induced current. τ_{corr} is defined as the correlation time of turbulent motions. The correlation time can be computed using the spectral approach outlined by Guerrero et al. (2019), where the turbulent energy spectra is used to compute the integral length scale ($l(r) = r \int E(r, k)k^{-1}dk / \int E(r, k)dk$) as a function of radius. This approach breaks down, however, in the region below the tachocline ($r < 0.72R_\odot$), where convective turbulence is effectively quenched (Figures 2.4, 2.6). The Alfvén velocity of strong magnetic fields stored in the region can be used to compute the correlation time of the current helicity. Two length scales (l_k, l_m) are computed from their respective kinetic and magnetic energy spectra ($E(u'), E(B')$) and the resulting correlation times are calculated as follows: $\tau_k = l_k/u'_{rms}$, $\tau_a = l_m/v_a$, where the Alfvén velocity is defined as: $v_a = B'_{rms}/\sqrt{\mu_0\rho_e}$. The resulting correlation times are presented on the right-hand side of Figure 2.6.

These profiles display little indication as to the cause of the evident shift in the emergence of the global magnetic field between models ns1 and ns2, with only slight differences in turbulent diffusivity (η_t) and correlation time (τ_{corr}) in areas directly

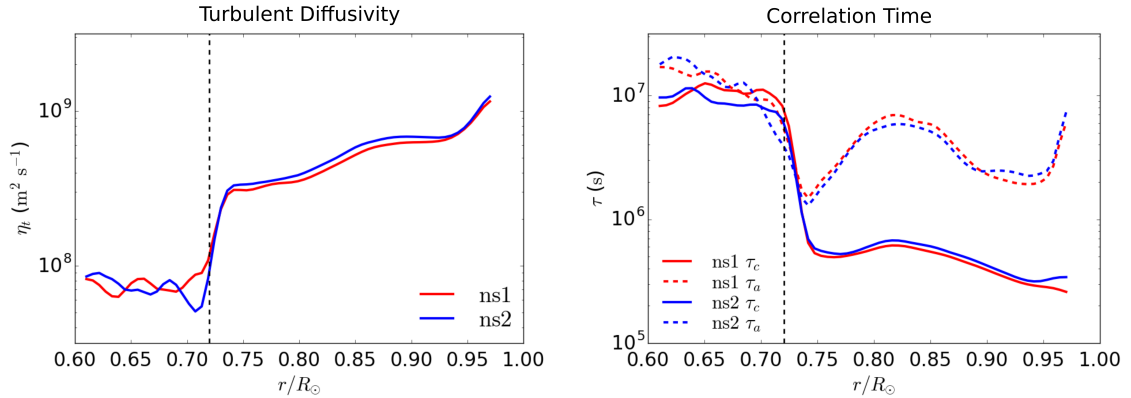


Figure 2.6 Left: radial dependence of the turbulent diffusivity, η_t , and right: the Alfvén (dashed lines) and kinetic (solid) correlation times, τ_a and τ_k , as defined by the first-order smoothing approximation (FOSA, Equation (2.5)).

Source: adapted from Stejko et al. (2020).

below the tachocline. More differences in the interplay of turbulent coefficients can be explored in contour plots (Figures 2.7, 2.8) of the global magnetic fields during their transition from one polarity to another, sampled at $t = 25, 35, 45$, and 55 years for simulation ns1, and $t = 33, 41, 45$, and 53 years for simulation ns2, along with the corresponding levels of turbulent kinetic and magnetic α -effects, α_k and α_m ; see Equation (2.5).

The transition snapshots (Figures 2.7, 2.8) exhibit clear differences between the models, specifically in the asymmetry of the evolving field in model ns1 (Figure 2.7); the mean poloidal field, $\overline{\mathbf{B}}_p = (\overline{B}_r, \overline{B}_\theta, 0)$, begins its reversal at the tachocline, extending into the radiation zone (yr. 35) in the region of minimal hydrodynamic shear between the radiation and convection zones (see also Figure 2.2). A strong poloidal field of a single polarity proceeds to encompass the entire radiation zone, accompanied by the development of strong toroidal fields (B_ϕ) under the tachocline in hemispherically anti-symmetric bands. This evolution is followed by much weaker fields in the convection zone. The convectively suppressed model (ns2, Figure 2.8) experiences the opposite pattern of development, where a single symmetric toroidal field (\overline{B}_ϕ) band encompasses both hemispheres, with two hemispherically reflected

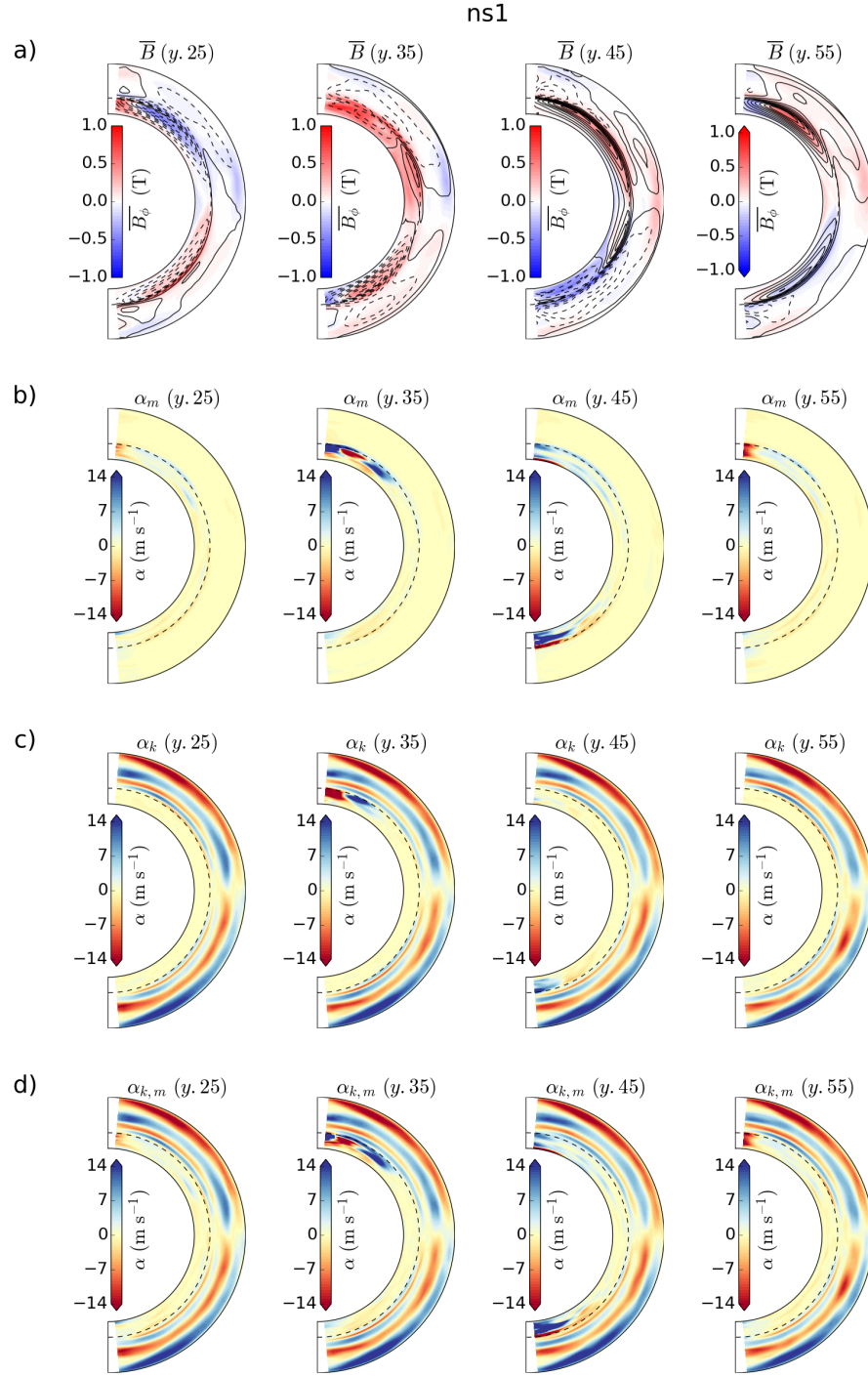


Figure 2.7 Snapshots of polarity reversal for model ns1. a) The toroidal magnetic field (\overline{B}_ϕ) exhibited by the colored contour; the poloidal magnetic field (\overline{B}_p) drawn by the solid/dashed contour lines. b) The magnetic turbulent transport coefficient α_m . c) The kinetic turbulent transport coefficient α_k . d) A summation of the two coefficients.

Source: adapted from Stejko et al. (2020).

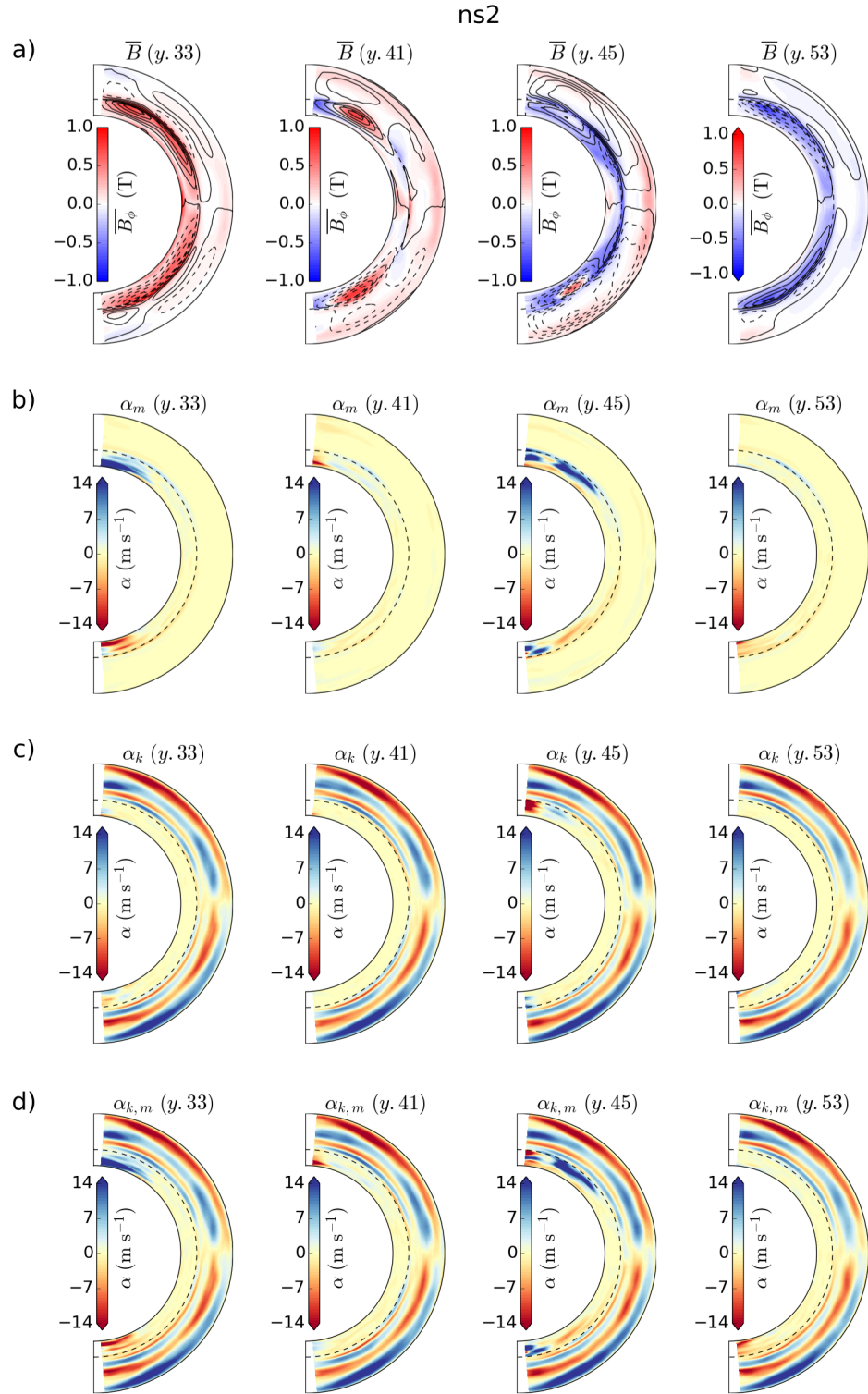


Figure 2.8 Same as Figure 2.7 for simulation ns2.
 Source: adapted from Stejko et al. (2020).

anti-symmetric poloidal field cells developing (yr. 45) at low latitudes at the base of the tachocline.

The kinetic α -effect is maintained almost entirely consistently over polarity reversals in ns1 and ns2; α_k emerges in hemispherically anti-symmetric bands near the surface, followed by a reversal at further depths. In the convection zone, α_k appears to dominate α_m by an order of magnitude. Similar turbulent transport coefficient profiles in EULAG-MHD models are explored in further detail by Guerrero et al. (2019), while the effectiveness of the first-order smoothing approximation (FOSA) is thoroughly investigated by the test-field method of Warnecke et al. (2018). Over the course of the polarity reversals, the region underneath the tachocline experiences the greatest deviation in its pattern of activity as well as the strongest manifestation of the turbulent α -effect. A relevant parameter for the evolution of the global magnetic field seems to be the high level of current helicity (α_m) generated underneath the tachocline. Due to the large values of τ_a in the radiation zone, the magnetic α -effect is dominant in the region, intermittently reaching levels much higher than kinetic turbulent helicity in the convection zone. These cyclonic motions are prominent during periods of transition when strong toroidal fields encompass the tachocline and radiation zone at higher latitudes. Figures 2.7 and 2.8 suggest that α_m is the potential source of the large variations observed in the models. The aggregate effects of turbulence in this region can be seen in the average of the magnetic turbulent coefficient (α_m) over these polarity reversals (Figure 2.9).

These simulations see an α_m term with an opposite sign begin to emerge at the poles with a very weak, but noticeable, onset in the suppressed model ns2. This term grows to a large field source in ns1, more than three times as strong as the bands of opposing helicities extended into the lower latitudes of the radiation zone. These polar helicities are the strongest contributors to the α -effect at and underneath the

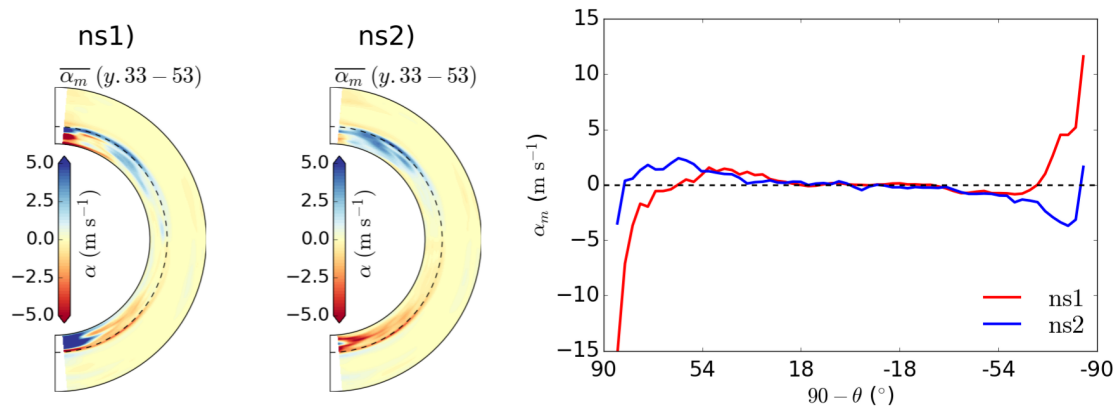


Figure 2.9 The magnetic turbulent transport coefficient, α_m , computed from the current helicity in the FOSA (Equation (2.5)). There are significant differences between the two models, denoted by the emergence of strong helicities near the poles of model ns1.

Source: adapted from Stejko et al. (2020).

tachocline. During polarity reversals, these regions intermittently become the single strongest turbulent sources of the poloidal magnetic field in these models.

2.4 Discussion

The simulations presented in this chapter are a continuation of previous work done with EULAG-MHD (Ghizaru et al., 2010; Guerrero et al., 2013, 2016, 2019), simulating solar convection, rotation, turbulence, and dynamo action in the numerical viscosity regime of the MPDATA algorithm.

In the study of solar convection, the results of models ns1, ns2, and ns3 illustrate the relevance of the stratification in the near-surface layer. Recent simulations done by Hotta et al. (2019) (without rotation and magnetic field) show that the near-surface region does not affect the amplitude of the convective motions in the deep interior. The results of these simulations, however, suggest that, for rotating hydro-magnetic convection, small convective acceleration close to the surface was sufficient to impact the redistribution of angular momentum, especially into the radiative zone. For simulations ns1 and ns2 there is a marked increase in the levels of rotational frequency,

while for simulation ns3, where the surface flows were quenched, the rotational frequency of the radiation zone remained the same as that of the reference frame (especially at higher latitudes).

The largest hydrodynamic impact at the tachocline is a movement away from the strongest velocity gradients found at the equator in simulation ns2, along with the solar rotation model RC02 in Guerrero et al. (2016), to stronger velocity gradients near the poles in simulation ns1 (Figure 2.3). In ns1, the angular frequency of the radiative layer begins to approach that of the convection zone near the equator, similar to the helioseismic inferences of solar observations (Schou et al., 1998).

These models develop dynamo cycles rooted in the area underneath the tachocline ($r < 0.72R_\odot$), with strong magnetic fields generated and stored in the radiation zone (Figure 2.5). The magnetic fields in these regions undergo a much lower rate of turbulent diffusivity (Figure 2.6), extending the lifetime of their cycle. High levels of α_m and shear at the tachocline (Figure 2.3) allow these regions to become strong sources of poloidal/toroidal transitions (Figures 2.7, 2.8).

The source of variance in hemispheric parity between models ns1 and ns2 (Figure 2.5) is not entirely clear; all of the models' parameters, except for the near-surface boundary, are identical. There are, however, notable differences in the development of tachoclinic shear (Figure 2.3) as well as substantial differences in the development of current helicity, and therefore α_m (Figure 2.9)—appearing as emerging turbulent sources near the poles of an opposing sign to the helicity that covers the rest of the hemisphere. These differences occur in regions of large hydrodynamic variations, exhibited by increasing rates of rotational frequency (Figure 2.2) from ns2 to ns1 (~ 425 nHz to ~ 430 nHz) and evident when comparing rotation rates near the poles; acceleration appears to filter up the latitudes in concert with increased convection rates near the surface.

The source of the strong current helicities and their orientation is not yet entirely

clear, however, it is notable that they are generated directly over the poles, where the Coriolis force has little influence on the orientation of the turbulent vorticity. It is also telling that these helicities are more strongly generated in a regime of increased polar downflow, following the increased subsurface convection in simulation ns1. As the majority of the impact of turbulent coefficients is shifted towards higher latitudes, they may result in a more stable manifestation of the dipolar global magnetic dynamo.

It is apparent that the NSSL and the tachocline appear to play a much more significant role in defining the structure of the global magnetic field than previously assumed. The overshoot layer underneath the tachocline and the solar subsurface layer in particular contain compressive effects that may be lost in the anelastic approximation of Boussinesq-type models such as EULAG and other convectively-driven global MHD models (Brun et al., 2004; Nelson et al., 2013; Augustson et al., 2015). Furthermore, the high velocity flows near the solar surface limit the computational domain of these models. In order to address these issues, and move towards a new generation of global algorithms that can more accurately simulate these neglected regions, this dissertation presents the development of a global acoustic model (Chapter 3). The computational techniques validated by this model will become the basis for a future global non-linear compressible algorithm, purpose-built to extend the computational domain to the solar surface and beyond.

CHAPTER 3

GLOBAL ACOUSTIC MODEL

3.1 Summary of the Governing Equations

A summary of the governing equations for the GALE code is presented as follows: mass continuity in Equation (3.1), the divergence of the conservation of momentum in Equation (3.2), and the conservation of energy in Equation (3.3). The definitions for terms used in these formulae as well as the conventions for linearizing the fields can be found in Subsection 3.1.1. Υ is defined as the divergence of the momentum field ($\Upsilon = \nabla \cdot \rho \mathbf{u} = \nabla \cdot \mathbf{m}$) and pseudo-forces relating to rotation in a non-inertial reference frame are grouped in the term R'_Υ ($R'_\Upsilon = -\nabla \cdot (\rho' \boldsymbol{\Omega} \times (\boldsymbol{\Omega} \times \mathbf{r})) - \nabla \cdot (2\boldsymbol{\Omega} \times \mathbf{m}')$). The definition of the source function (S) can be found in Section 3.4. These linearized governing equations are solved on a fully global 3D grid, $0 < r < 1.0007R_\odot$, $0 < \theta < \pi$, $0 < \phi \leq 2\pi$, over background field terms derived from the standard solar model S (Christensen-Dalsgaard et al., 1996).

$$\frac{\partial \rho'}{\partial t} + \Upsilon' = 0, \quad (3.1)$$

$$\frac{\partial \Upsilon'}{\partial t} + \nabla : (\mathbf{m}' \tilde{\mathbf{u}} + \tilde{\rho} \tilde{\mathbf{u}} \mathbf{u}') = -\nabla^2 (p') - \nabla \cdot (\rho' \tilde{g}_r \hat{\mathbf{r}}) + R'_\Upsilon + \nabla \cdot S \hat{\mathbf{r}}, \quad (3.2)$$

$$\frac{\partial p'}{\partial t} = -\frac{\Gamma_1 \tilde{p}}{\tilde{\rho}} \left(\nabla \cdot \tilde{\rho} \mathbf{u}' + \rho' \nabla \cdot \tilde{\mathbf{u}} - \frac{p'}{\tilde{p}} \tilde{\mathbf{u}} \cdot \nabla \tilde{\rho} + \tilde{\rho} \mathbf{u}' \cdot \frac{N^2}{\tilde{g}_r} \hat{\mathbf{r}} \right). \quad (3.3)$$

3.1.1 Linearized field formulation

The governing equations (Equations (3.1)-(3.3)) are linearized by splitting the field terms into a base component (tilde) and a perturbation from that base (prime). The scale of the perturbation terms is denoted by the small number $\epsilon \ll 1$. The split field is defined as:

$$\begin{aligned}
\rho &= \tilde{\rho} + \epsilon \rho' , & \Gamma_1 &= \Gamma_1 , \\
p &= \tilde{p} + \epsilon p' , & \mathbf{g} &= \tilde{g}_r \hat{\mathbf{r}} , \\
\mathbf{u} &= \tilde{\mathbf{u}} + \epsilon \mathbf{u}' , & &
\end{aligned} \tag{3.4}$$

where ρ is the density, p is the thermodynamic pressure, and \mathbf{u} is the velocity vector. The Cowling approximation is employed in this formulation, making the assumption that gravitational perturbations will be significantly smaller than corresponding perturbations in the density profile (Cowling, 1941). In the adiabatic approximation (Christensen-Dalsgaard, 2014), the time-scale of heat transfer is much smaller than the oscillation period and is therefore neglected, resulting in an adiabatic ratio (Γ_1) that is constant in time.

3.2 Derivation

The governing equations are derived from the general form of the Navier-Stokes equations. The following sections demonstrate the linearization of mass continuity (Subsection 3.2.1), the conservation of momentum (Subsection 3.2.2), and the conservation of energy (Subsection 3.2.3).

3.2.1 Mass continuity

Mass continuity in the form of Equation (3.1) can be derived from the standard form of the Navier-Stokes continuity (Equation (3.5)).

$$\frac{\partial \rho}{\partial t} + \nabla \cdot \rho \mathbf{u} = 0 . \tag{3.5}$$

Using the split field formulation defined in Subsection 3.1.1, the field terms can be rewritten in the following manner.

$$\frac{\partial}{\partial t} (\tilde{\rho} + \epsilon \rho') + \nabla \cdot (\tilde{\rho} \tilde{\mathbf{u}} + \epsilon \tilde{\rho} \mathbf{u}' + \epsilon \rho' \tilde{\mathbf{u}} + \underline{\epsilon^2 \rho' \mathbf{u}'}) = 0 .$$

Since the magnitude of the perturbations ($\epsilon \ll 1$) is very small, square terms (ϵ^2), underlined in the above formula, can be disregarded. The field is then split into a continuity of base flow and a continuity of the perturbations from that base flow.

$$\frac{\partial \tilde{\rho}}{\partial t} + \nabla \cdot \tilde{\rho} \tilde{\mathbf{u}} = 0 , \quad \frac{\partial \rho'}{\partial t} + \nabla \cdot (\tilde{\rho} \mathbf{u}' + \rho' \tilde{\mathbf{u}}) = 0 .$$

Rewriting the divergence of momentum field perturbations as $\Upsilon' = \nabla \cdot \mathbf{m}' = \nabla \cdot (\tilde{\rho} \mathbf{u}' + \rho' \tilde{\mathbf{u}})$, results in the final form of the mass continuity (Equation (3.1)).

$$\frac{\partial \rho'}{\partial t} + \Upsilon' = 0 .$$

3.2.2 Conservation of momentum

The governing equation for the conservation of momentum (Equation (3.2)) is derived from the general form of the well-known Cauchy momentum equation in its conservation form in a rotating non-inertial reference frame:

$$\frac{\partial \rho \mathbf{u}}{\partial t} + \nabla \cdot (\rho \mathbf{u} \mathbf{u}) = -\nabla p - \rho \mathbf{g} - \rho \boldsymbol{\Omega} \times (\boldsymbol{\Omega} \times \mathbf{r}) - 2 \boldsymbol{\Omega} \times \rho \mathbf{u} , \quad (3.6)$$

where $\mathbf{u} \mathbf{u}$ is the velocity dyad. This equation is linearized using the formulation defined in Subsection 3.1.1. Any square (ϵ^2) or cubic (ϵ^3) perturbation terms can be omitted due to negligible contributions.

$$\begin{aligned} \frac{\partial}{\partial t} (\tilde{\rho} \tilde{\mathbf{u}} + \epsilon \tilde{\rho} \mathbf{u}' + \epsilon \rho' \tilde{\mathbf{u}}) + \nabla \cdot (\tilde{\rho} \tilde{\mathbf{u}} \tilde{\mathbf{u}} + \epsilon (\tilde{\rho} \tilde{\mathbf{u}}) \mathbf{u}' + \epsilon (\tilde{\rho} \mathbf{u}' + \rho' \tilde{\mathbf{u}}) \tilde{\mathbf{u}}) = -\nabla (\tilde{p} + \epsilon p') \\ - (\tilde{\rho} + \epsilon \rho') \tilde{g}_r \hat{\mathbf{r}} - (\tilde{\rho} + \epsilon \rho') (\boldsymbol{\Omega} \times (\boldsymbol{\Omega} \times \mathbf{r})) - 2 (\boldsymbol{\Omega} \times (\tilde{\rho} \tilde{\mathbf{u}} + \epsilon (\tilde{\rho} \mathbf{u}' + \rho' \tilde{\mathbf{u}}))) . \end{aligned}$$

Separating the perturbative flow field from the base, and shortening the perturbation of the momentum field to $\mathbf{m}' = \tilde{\rho}\mathbf{u}' + \rho'\tilde{\mathbf{u}}$, results in the following formula for the conservation of momentum.

$$\frac{\partial \mathbf{m}'}{\partial t} + \nabla \cdot (\mathbf{m}'\tilde{\mathbf{u}} + \tilde{\rho}\tilde{\mathbf{u}}\mathbf{u}') = -\nabla(p') - \rho'\tilde{g}_r\hat{\mathbf{r}} - \rho'(\boldsymbol{\Omega} \times (\boldsymbol{\Omega} \times \mathbf{r})) - 2(\boldsymbol{\Omega} \times \mathbf{m}') . \quad (3.7)$$

In order to ease the computational cost of this acoustic algorithm, the field can be split into two parts: a solenoidal momentum field component and a potential momentum field component. Solenoidal contributions to the perturbation field are significantly smaller and are concentrated in different scales from the potential flow field, as such, the solenoidal contributions can be omitted using the following split-field formulation:

$$\rho\mathbf{u} = \mathbf{m} = \nabla \times \boldsymbol{\Psi} + \nabla\Phi = \mathbf{m}_s + \mathbf{m}_p .$$

The solenoidal momentum field (\mathbf{m}_s) is defined as the curl of some vector potential field $\boldsymbol{\Psi}$, and the potential momentum field (\mathbf{m}_p) is the divergence of another scalar potential momentum field Φ . The field is split into two orthogonal parts ($\nabla \times \mathbf{m}_p = 0$ and $\nabla \cdot \mathbf{m}_s = 0$) and the potential flow is isolated by taking the divergence of the perturbation of the Cauchy conservation of momentum equation (Equation (3.7)) where, $\nabla \cdot \rho\mathbf{u} = \nabla \cdot \mathbf{m} = \nabla^2\Phi = \Upsilon$.

$$\begin{aligned} \frac{\partial \Upsilon'}{\partial t} + \boldsymbol{\nabla} : (\mathbf{m}'\tilde{\mathbf{u}} + \tilde{\rho}\tilde{\mathbf{u}}\mathbf{u}') &= -\nabla^2(p') \\ &- \nabla \cdot (\rho'\tilde{g}_r\hat{\mathbf{r}}) - \nabla \cdot (\rho'\boldsymbol{\Omega} \times (\boldsymbol{\Omega} \times \mathbf{r})) - \nabla \cdot (2\boldsymbol{\Omega} \times \mathbf{m}') . \end{aligned}$$

This is the full form of the governing equation for potential momentum conservation (Equation (3.2)) where “ $\boldsymbol{\nabla} :$ ” is defined as the divergence dyad.

3.2.3 Conservation of energy

The final governing equation (Equation (3.3))—the conservation of energy—is defined by the following thermodynamic equation of state for the solar interior from the formulation of Cox & Giuli (1968).

$$\frac{1}{\Gamma_3 - 1} \left(\frac{Dp}{Dt} - \frac{\Gamma_1 p}{\rho} \frac{D\rho}{Dt} \right) = \rho \frac{DQ}{Dt} ,$$

$$\text{where:} \quad \Gamma_1 = \left(\frac{\partial \ln \rho}{\partial \ln p} \right)_{ad} , \quad \Gamma_3 - 1 = \left(\frac{\partial \ln T}{\partial \ln \rho} \right)_{ad} .$$

This relation, where Q is heat added to the system, can be rewritten in Eulerian form with total material derivatives ($Df/Dt = \partial f/\partial t + \mathbf{u} \cdot \nabla f$). In the adiabatic approximation (Christensen-Dalsgaard, 2014), the assumption that heat transfer is negligible within the time scale of the period of acoustic oscillations can be employed ($DQ/Dt = 0$).

$$\frac{\partial p}{\partial t} + \mathbf{u} \cdot \nabla p = \frac{\Gamma_1 p}{\rho} \left(\frac{\partial \rho}{\partial t} + \mathbf{u} \cdot \nabla \rho \right) .$$

Using the acoustic formulation outlined in Subsection 3.1.1, the adiabatic relation is linearized as follows:

$$\left(\tilde{\rho} \frac{\partial \tilde{p}}{\partial t} + \epsilon \left(\tilde{\rho} \frac{\partial p'}{\partial t} + \rho' \frac{\partial \tilde{p}}{\partial t} \right) + \tilde{\rho} \tilde{\mathbf{u}} \cdot \nabla \tilde{p} + \epsilon (\rho' \tilde{\mathbf{u}} \cdot \nabla \tilde{p} + \tilde{\rho} (\tilde{\mathbf{u}} \cdot \nabla p' + \mathbf{u}' \cdot \nabla \tilde{p})) \right) = \Gamma_1 \left(\left(\tilde{p} \frac{\partial \tilde{\rho}}{\partial t} + \epsilon \left(\tilde{p} \frac{\partial \rho'}{\partial t} + p' \frac{\partial \tilde{\rho}}{\partial t} \right) + \tilde{p} \tilde{\mathbf{u}} \cdot \nabla \tilde{\rho} + \epsilon (p' \tilde{\mathbf{u}} \cdot \nabla \tilde{\rho} + \tilde{p} (\tilde{\mathbf{u}} \cdot \nabla \rho' + \mathbf{u}' \cdot \nabla \tilde{\rho})) \right) \right) .$$

Separating perturbations from the base flow results in a linear equation for the conservation of energy.

$$\tilde{\rho} \frac{\partial p'}{\partial t} + (\rho' \tilde{\mathbf{u}} \cdot \nabla \tilde{p} + \tilde{\rho} (\tilde{\mathbf{u}} \cdot \nabla p' + \mathbf{u}' \cdot \nabla \tilde{p})) = \Gamma_1 \left(\tilde{p} \frac{\partial \rho'}{\partial t} + (p' \tilde{\mathbf{u}} \cdot \nabla \tilde{\rho} + \tilde{p} (\tilde{\mathbf{u}} \cdot \nabla \rho' + \mathbf{u}' \cdot \nabla \tilde{\rho})) \right). \quad (3.8)$$

In order to avoid convective instabilities in the model, Equation (3.8) can be rewritten in terms of the Brunt-Väisälä frequency (N^2 , see Section 3.3). Plugging in mass continuity (Equation (3.1)) and rearranging terms leaves a formula that can be used to manually alter convection without the need to change background field terms ($\tilde{\rho}$, \tilde{p} , Γ_1).

$$\frac{1}{\tilde{p}\Gamma_1} \frac{\partial p'}{\partial t} + \frac{1}{\tilde{\rho}} \nabla \cdot (\tilde{\rho} \mathbf{u}' + \rho' \tilde{\mathbf{u}}) = -\mathbf{u}' \cdot \left(\frac{1}{\Gamma_1 \tilde{p}} \nabla \tilde{p} - \frac{1}{\tilde{\rho}} \nabla \tilde{\rho} \right) - \tilde{\mathbf{u}} \cdot \left(-\frac{1}{\tilde{\rho}} \left(\nabla \rho' + \frac{p'}{\tilde{p}} \nabla \tilde{\rho} \right) \right).$$

Substituting in N^2 and rearranging terms further results in the final form of the governing relation for pressure (Equation (3.3)).

$$\frac{\partial p'}{\partial t} = -\frac{\Gamma_1 \tilde{p}}{\tilde{\rho}} \left(\nabla \cdot \tilde{\rho} \mathbf{u}' + \rho' \nabla \cdot \tilde{\mathbf{u}} - \frac{p'}{\tilde{p}} \tilde{\mathbf{u}} \cdot \nabla \tilde{\rho} + \tilde{\rho} \mathbf{u}' \cdot \frac{N^2}{g} \hat{\mathbf{r}} \right).$$

3.3 Brunt-Väisälä Frequency

Buoyancy throughout the solar interior is characterized by the Brunt-Väisälä frequency (N^2), where

$$N^2 = g \left(\frac{1}{\Gamma_1} \frac{\partial \ln p}{\partial r} - \frac{\partial \ln \rho}{\partial r} \right). \quad (3.9)$$

The governing equations become unconditionally unstable in regions where this term is negative ($N^2 < 0$). In order to avoid such instabilities, the conservation of energy (Equation (3.1)) is derived as a function of the Brunt-Väisälä frequency—the slightly negative values of this term are set to zero directly, obviating the need to alter

background profiles of pressure (p), density (ρ), or the adiabatic ratio (Γ_1) as in similar convectively stable models of Hanasoge et al. (2006); Parchevsky & Kosovichev (2007); Hartlep et al. (2008). Altering the algorithm to maintain stability may introduce small deviations in mode frequencies (Papini et al., 2014); however, it is still accurate enough to simulate inferences of flows in the convective interior using helioseismology techniques.

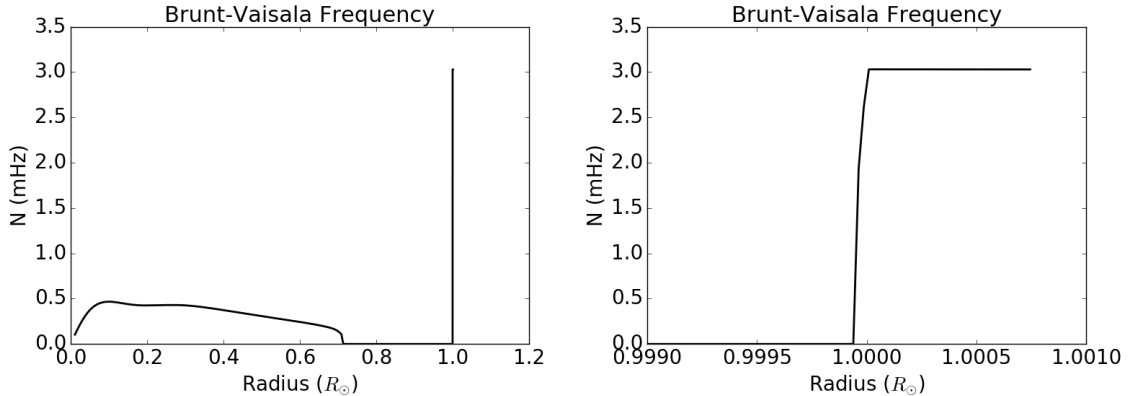


Figure 3.1 The altered background profile of the Brunt-Väisälä frequency, where slightly negative values in the convection zone are set to zero. An isothermal buffer layer is extended above the model surface to $\sim 1.0007R_\odot$.

3.4 Acoustic Oscillation Source Function

The source of acoustic oscillations is modeled as a radially directed force ($S\hat{r}$) in the conservation of momentum (Equation (3.2)). The structure of the source function is formulated in a similar manner to Hanasoge et al. (2006), where a thin shallow layer simulates the region responsible for the excitation of solar p-modes, see Goldreich et al. (1994), Stein & Nordlund (2001). The source is modeled as a radial Gaussian function with a standard deviation of $\sigma = 0.0001R_\odot \sim 69.6$ km, centered at $\mu = 0.9995R_\odot$.

The full time-dependent source profile is generated using another Gaussian function in frequency space, centered at $\mu = 3.2$ mHz, with a standard deviation of $\sigma = 1$ mHz—simulating the power peak of observed solar oscillations. In

order to mimic a stochastic excitation of acoustic modes (Woodard, 1984), the frequency-dependent Gaussian function is multiplied by a random number at each frequency interval ($f_s = 1/\Delta t$), as shown in Figure 3.2. Applying a Fourier transform to this spectrum produces a time-dependent profile, of which a unique one is generated for every harmonic degree and azimuthal order (l, m) in the spherical harmonic decomposition of the source function ($S = \sum_{lm} a_{lm} Y_{lm}$). The stochastic nature of the source profile forms the basis for simulating realization noise present in solar observations—inextricably tied to the turbulent convection that excites acoustic signals in the solar interior.

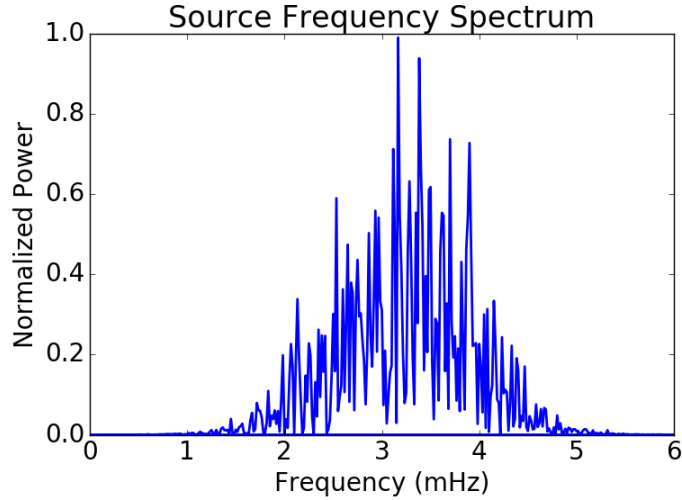


Figure 3.2 An example of the frequency spectrum that characterizes the time-dependent profile of the source of acoustic oscillations near the surface of the model; such a unique random profile is generated for every spherical harmonic degree and azimuthal order (l, m) of the source function.

3.5 Damping Layer

The boundaries of the model are solved as simple reflective walls with a zero velocity perturbation condition ($\mathbf{u}' = 0$). In order to avoid non-physical surface reflections from affecting internal acoustic mode frequencies, a buffer zone is extended past the

model surface up to $\sim 1.0007R_\odot$. This layer contains an exponentially increasing damping factor (σ) which can be expressed in the governing equations as follows:

$$\frac{\partial \rho'}{\partial t} = -\Upsilon' - \sigma \rho', \quad \frac{\partial \Upsilon'}{\partial t} = -\nabla^2 p' + \mathcal{Y} - \sigma \Upsilon', \quad \frac{\partial p'}{\partial t} = \mathcal{P} - (\sigma - \alpha) p'. \quad (3.10)$$

This simplified form of the governing Equations (3.1)-(3.3) aggregates external force contributions in the conservation of momentum (Equation (3.2)) into \mathcal{Y} , and the momentum field variables along with the Brunt-Väisälä term in the conservation of energy (Equation (3.3)) into \mathcal{P} . The pressure term in the RHS of Equation (3.3) is treated separately, with background field terms defined as $\alpha = \Gamma_1 \tilde{\rho}^{-1} \tilde{\mathbf{u}} \cdot \nabla \tilde{\rho}$, and grouped with the damping term (σ). To avoid precision errors when computing the damping term, it is solved implicitly in the time-discretization scheme using the integrating factor method. This layer serves to simulate the escape of acoustic oscillations above the cutoff frequency (> 5 mHz), into the solar atmosphere.

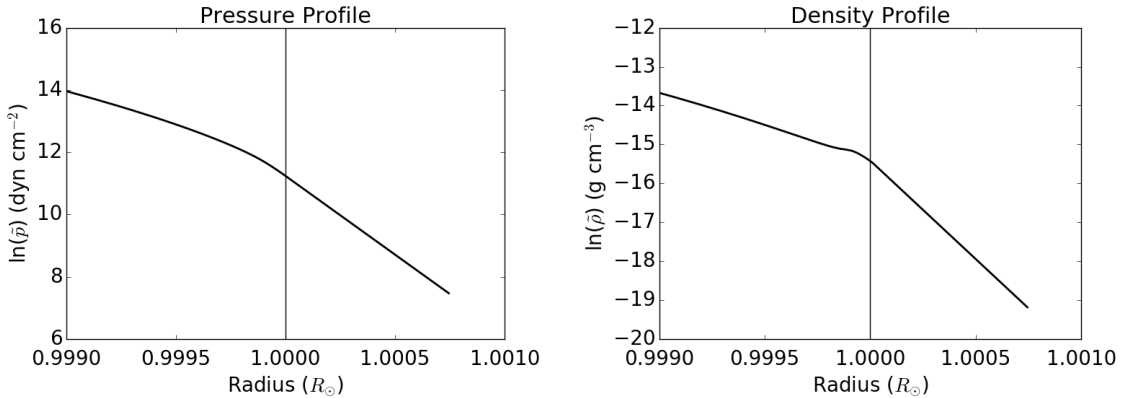


Figure 3.3 The background profiles of pressure (left) and density (right). A buffer layer is extended past the surface of the model (vertical line), where profiles of pressure and density fall exponentially at a rate defined by a constant pressure scale height, see Equation (3.11).

The buffer zone is isothermal, with background field terms of sound speed ($c^2 = \Gamma_1 \tilde{p} / \tilde{\rho}$), gravity ($\tilde{g}_r \hat{\mathbf{r}}$) and Brunt-Väisälä frequency (N^2 , see Figure 3.1)

remaining constant throughout the layer. Profiles of pressure (\tilde{p}) and density ($\tilde{\rho}$) fall exponentially at a rate defined by a constant pressure scale height in the buffer zone (Hanasoge et al., 2006), as shown in Equation (3.11) and Figure 3.3.

$$\begin{aligned} \tilde{p} &= \tilde{p}(R_\odot) \exp\left(\frac{R_\odot - r}{H_p(R_\odot)}\right), \\ \tilde{\rho} &= \tilde{\rho}(R_\odot) \exp\left(\frac{R_\odot - r}{H_p(R_\odot)}\right). \end{aligned} \quad R_\odot \leq r \leq 1.0007R_\odot \quad (3.11)$$

3.6 Numerical Method

This section contains the numerical method and computational set-up for the GALE code. The governing equations are solved using a pseudo-spectral technique, with second-order finite-difference methods implemented in time (Subsection 3.6.1) and in the radial direction (Subsection 3.6.2). Field terms along the surface of the sphere are decomposed into spherical harmonic coefficients with differentiation done using spectral methods in frequency space (Subsection 3.6.3). The Poisson solver used to implicitly compute the potential flow (Φ , used to recompute the velocity field) is described in Subsection 3.6.4. In order to include the contributions of the material derivative dyad in the conservation of momentum (Equation (3.2)), a pseudo-spectral formulation of the divergence in a tensor spherical harmonic basis is defined in Subsection 3.6.5. The derivation of a basic stability condition for the method can be found in Subsection 3.6.7, and the parallelization technique is described in Subsection 3.6.8.

3.6.1 Temporal discretization

The time-discretization scheme used in governing Equations (3.1)-(3.3) is a combination of forward and backward Euler schemes. A first order-accurate backward Euler scheme is used to help maintain stability when computing the contributions

of the potential flow field to perturbations of pressure (Equation (3.1)). A combination of forward and backward Euler schemes for the conservation of momentum (Equation (3.2)) and continuity (Equation (3.1)), respectively, form a second order-accurate central finite-difference scheme that computes oscillatory perturbations in the potential flow field.

$$\begin{aligned}
\Upsilon'^{(n+1)} &= e^{-\sigma\Delta t}\Upsilon'^{(n)} - \Delta te^{-\sigma\Delta t} [\nabla^2 p'^{(n)} - \mathcal{Y}^{(n)}(\rho', \mathbf{u}')] , \\
\rho'^{(n+1)} &= e^{-\sigma\Delta t}\rho'^{(n)} - \Delta t\Upsilon'^{(n+1)} , \\
p'^{(n+1)} &= e^{-(\sigma-\alpha)\Delta t}p'^{(n)} + \Delta t\mathcal{P}^{(n+1)}(\rho', \mathbf{u}') .
\end{aligned} \tag{3.12}$$

The governing equations are written using the condensed form introduced in Equation (3.10), where aggregate terms in the conservation of momentum and the conservation of energy relations are denoted by \mathcal{Y} , \mathcal{P} , and α . The integrating factor method is used to implicitly compute the contributions of the damping term (σ), see Section 3.5.

3.6.2 Radial discretization and differentiation

Spatial differentiation in the radial direction is done on a discrete grid, employing finite-difference methods. A one-dimensional (1D) representation of the radial mesh is shown in Figure 3.4, where the subscript “ k ” denotes discrete mesh points from $k = 1$ to $k = K$. The distance between two points, e.g., $k - 1$ and k , is represented by Δr_k .

In order to compute the radial component of the Laplacian (∇^2) in Equation (3.2), the following second order-accurate central finite-difference scheme (Equation (3.13)) can be used.

$$\frac{\partial}{\partial r} \left(r^2 \frac{\partial f}{\partial r} \right) = \frac{2}{\Delta r_k + \Delta r_{k+1}} \left(r_{k+0.5}^2 \frac{f_{k+1} - f_k}{\Delta r_{k+1}} - r_{k-0.5}^2 \frac{f_k - f_{k-1}}{\Delta r_k} \right) . \tag{3.13}$$

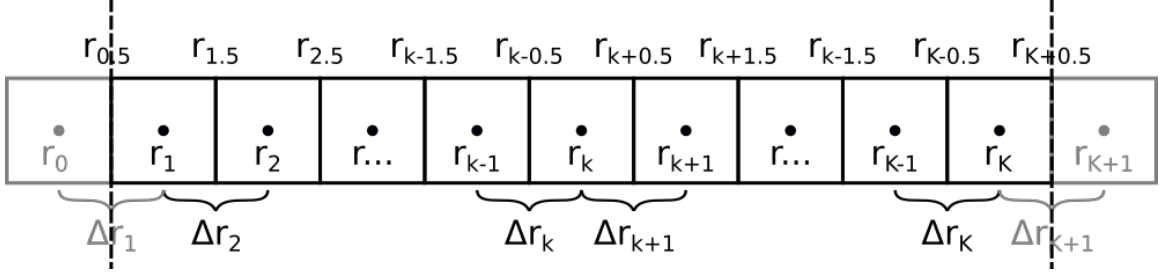


Figure 3.4 A 1D representation of the radial grid, where discrete mesh points are denoted by the subscript “ k ”. r_0 and r_{k+1} represent ghost points outside of the model boundaries that may be used during finite-difference computations.

Computations of divergence ($\nabla \cdot$) and gradient (∇) can be accomplished with the following second order-accurate polynomial central finite-difference scheme (Equation (3.14)) for first radial derivatives.

$$\frac{\partial f}{\partial r} = -\frac{\Delta r_{k+1}}{\Delta r_k(\Delta r_{k+1} + \Delta r_k)} f_{k-1} + \frac{\Delta r_{k+1} - \Delta r_k}{\Delta r_{k+1} \Delta r_k} f_k + \frac{\Delta r_k}{\Delta r_{k+1}(\Delta r_{k+1} + \Delta r_k)} f_{k+1} . \quad (3.14)$$

The precision of these methods and their agreement with theoretical computations of eigenmodes is well within an acceptable range for modeling and testing local heliosesimology techniques throughout the convective interior. While higher order-accurate schemes may be more precise, employing a non-uniform grid with large variations in spacing will diminish any improvements that could be expected.

The radial grid used in this model (Figure 3.5) is spaced evenly with respect to acoustic travel time ($\int 1/c_s dr$), allowing for the computation of acoustic oscillations across large variations in sound speed (c_s). While this grid is effective at capturing effects throughout the majority of the model interior, pressure and density scale heights begin to drop off faster than sound speed closer to the model surface ($r > 0.99R_\odot$). In order to properly resolve the effects of the Brunt-Väisälä frequency (N^2 , Equation (3.9)), a logarithmic pressure grid spaced evenly in $\ln(p)$ (e.g., Hanasoge

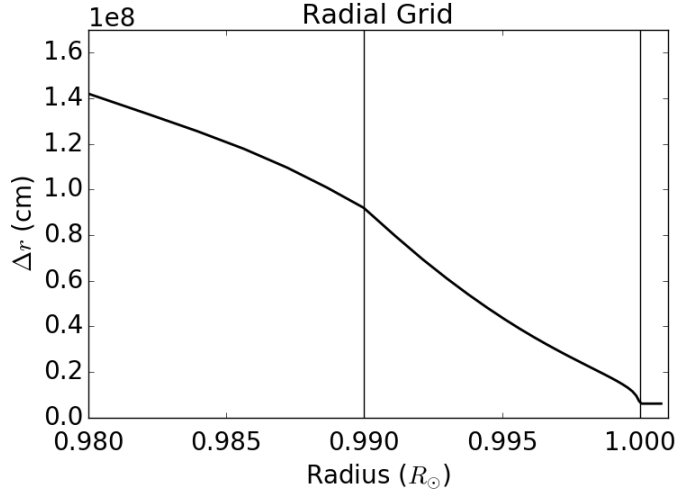


Figure 3.5 The distance between radial grid points in cm. Spacing is even with respect to acoustic travel time ($\int 1/c_s dr$) between $0 < r < 0.99R_\odot$. The grid is switched to a spacing even with the drop in logarithmic pressure ($\ln \hat{p}$) between $0.99R_\odot < r < R_\odot$. In the isothermal buffer layer above the model surface ($R_\odot < r < 1.0007R_\odot$) a uniform spacing is implemented.

et al., 2006) is substituted for this region. In the isothermal buffer layer above the model surface (Section 3.5), grid spacing becomes uniform.

3.6.3 Spherical harmonic decomposition and differentiation

Transverse discretization is done through spherical harmonic decomposition using the Libsharp spherical harmonic library (Reinecke & Seljebotn, 2013). The spectral resolution is defined by the maximum allowable quantum number ($l_{max}(r)$) at each radial point. This value controls the mesh size of the Gauss-Legendre grid, containing $N_\phi = 3l_{max}$ azimuthal grid points and $N_\theta = 3l_{max}/2$ latitudinal grid points—chosen so as to avoid aliasing during spherical harmonic decomposition. The azimuthal mesh points (N_ϕ) are spaced at even intervals between $0 < \phi \leq 2\pi$, while the latitudinal points (N_θ) are placed at the roots of the corresponding Legendre polynomial between $0 < \theta < \pi$. To avoid oversampling at high latitudes the Libsharp library natively implements polar optimisation, or the “reduced Gauss-Legendre grid”.

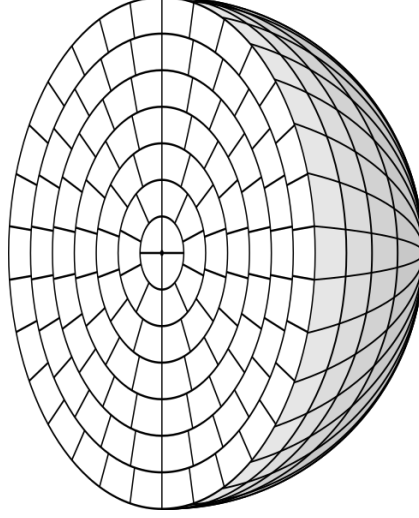


Figure 3.6 A representation of the 3D structure of the model grid. The resolution tangent to the surface of the sphere is defined by the maximum allowable quantum number ($l_{max}(r)$) at each radial point—controlling the mesh size of the Gauss-Legendre grid, containing $N_\phi = 3l_{max}$ azimuthal grid points and $N_\theta = 3l_{max}/2$ latitudinal grid points.

Differentiation along the surface of the sphere (θ, ϕ) can be accomplished with a spectral method. In the spherical harmonic decomposition, the transverse portion of the Laplacian ($\nabla_{\theta\phi}$) is defined by the following simple relation.

$$\nabla_{\theta\phi} Y_{lm} = -l(l+1)Y_{lm} .$$

The first derivatives ($\sin\theta(\partial/\partial\theta), \partial/\partial\phi$) can also be computed in spherical harmonic space, using the recursion relations derived in Appendix B, Equations (B.13), (B.15), respectively.

$$\sin\theta \frac{\partial Y_{lm}}{\partial\theta} = l \sqrt{\frac{(l-m+1)(l+m+1)}{(2l+3)(2l+1)}} Y_{l+1,m} - (l+1) \sqrt{\frac{(l-m)(l+m)}{(2l-1)(2l+1)}} Y_{l-1,m} .$$

$$\frac{\partial Y_{lm}}{\partial\phi} = im Y_{lm} .$$

3.6.4 Numerical solver of the potential field

Solving for the potential flow field ($\mathbf{m}_p = \nabla \cdot \Phi$, Subsection 3.2.2) will allow for the computation of velocity and density fields used in the governing equations (\mathbf{u}' , ρ'). The spherical harmonic decomposition (Subsection 3.6.3) of the divergence of the momentum field ($\Upsilon = \nabla^2 \Phi$) can be used to create 1D radial equations for each azimuthal order and harmonic degree (l, m).

$$\Upsilon = \sum_{l=0}^{l_{max}} \sum_{m=-1}^l \frac{1}{r^2} \left[\frac{\partial}{\partial r} \left(r^2 \frac{\partial \Phi_{lm}}{\partial r} \right) - l(l+1)\Phi_{lm} \right] Y_{lm} . \quad (3.15)$$

A series of 1D implicit numerical solvers of Poisson's equation can be used to compute the potential flow field (Φ) from the divergence of the momentum field (Υ). Using the central finite-difference method defined in Subsection 3.6.2, Equation (3.13), the Laplacian (Equation (3.15)) can be discretized as:

$$r_{k,lm}^2 \Upsilon_{k,lm} = \frac{2}{\Delta r_k + \Delta r_{k+1}} \left(r_{k+0.5}^2 \frac{\Phi_{k+1,lm} - \Phi_{k,lm}}{\Delta r_{k+1}} - r_{k-0.5}^2 \frac{\Phi_{k,lm} - \Phi_{k-1,lm}}{\Delta r_k} \right) - l(l+1)\Phi_{k,lm} , \quad (3.16)$$

where k is the radial index. Separating, rearranging, and grouping terms of the same radial index on the RHS of Equation (3.16), leaves the following discrete radial function.

$$r_{k,lm}^2 \Upsilon_{k,lm} = a_{k,lm} \Phi_{k-1,lm} + b_{k,lm} \Phi_{k,lm} + c_{k,lm} \Phi_{k+1,lm} , \quad (3.17)$$

The following set of equations compute the LU-decomposition (\mathbf{K}_{LU}) from the band-storage matrix \mathbf{K} (Equation (3.19)).

$$\mathbf{K}_{\text{LU}} = \begin{bmatrix} 0 & \beta_1 & c_1 \\ \alpha_2 & \beta_2 & c_2 \\ \vdots & \vdots & \vdots \\ \alpha_{K-1} & \beta_{K-1} & c_{K-1} \\ \alpha_K & \beta_K & 0 \end{bmatrix}, \quad \text{where:} \quad \begin{aligned} \beta_1 &= b_1 \\ \alpha_k &= \frac{a_k}{\beta_{k-1}} \\ \beta_k &= b_k - \alpha_k c_{k-1} \end{aligned}$$

Breaking the matrix (\mathbf{K}_{LU}) into its lower (\mathbf{L}) and upper components (\mathbf{U}) results in a linear system of equations that can be iteratively computed using forward- and backward-substitution.

$$\mathbf{K}\Phi = r^2\Upsilon, \quad \Rightarrow \quad \begin{cases} \mathbf{L}y = r^2\Upsilon, \\ \mathbf{U}\Phi = y. \end{cases} \quad (3.20)$$

The following set of equations solve the lower matrix (\mathbf{L} , Equation (3.20)) for the dependent variables y_k .

$$\begin{aligned} y_1 &= r_1^2 \Upsilon_1, \\ y_k &= r_k^2 \Upsilon_k - \alpha_k y_{k-1}. \end{aligned}$$

The upper matrix (\mathbf{U} , Equation (3.20)) can now be computed for the potential flow field (Φ_k).

$$\begin{aligned} \Phi_K &= \frac{r_K^2 \Upsilon_K}{\beta_K}, \\ \Phi_k &= \frac{y_k - c_k \Phi_{k+1}}{\beta_k}. \end{aligned}$$

This set of equations gives a solution for every radial layer of the Poisson function ($\Upsilon = \nabla^2 \Phi$). This method is iterated over every spherical harmonic quantum number (l, m) for the full solution of the potential flow field.

3.6.5 Material derivative dyad

The material derivative in the governing equation for the conservation of momentum (Equation (3.2)) can be written in its Cauchy conservation form as the linearized dyad $\nabla \cdot \mathbf{N}$, where

$$\mathbf{N} = \rho' \tilde{\mathbf{u}} \tilde{\mathbf{u}} + \tilde{\rho} \mathbf{u}' \tilde{\mathbf{u}} + \tilde{\rho} \tilde{\mathbf{u}} \mathbf{u}' .$$

In order to compute the divergence of this term in spherical harmonic coefficient space, a change of basis is required. The tensor spherical harmonic (TSH) basis defined in Appendix A, Section A.2, can be employed to convert this dyad (\mathbf{N}) into a form that will easily lend itself to the computation of derivatives tangent to the surface of the sphere with recursion relations. Using the definition of a field in the TSH basis (Equation (A.23)), the dyad can be expanded as:

$$\mathbf{N} = \sum_{m=-lmax}^{lmax} \sum_{l=|m|}^{lmax} (N_{lm}^{L_0} \mathbf{T}_{lm}^{L_0} + N_{lm}^{E_1} \mathbf{T}_{lm}^{E_1} + N_{lm}^{B_1} \mathbf{T}_{lm}^{B_1} + N_{lm}^{T_0} \mathbf{T}_{lm}^{T_0} + N_{lm}^{E_2} \mathbf{T}_{lm}^{E_2} + N_{lm}^{B_2} \mathbf{T}_{lm}^{B_2}) .$$

$N_{lm}^{L_0}$ is the fully radial component (N^{rr}) and $N_{lm}^{T_0}$ is the transverse ($N^{\theta\theta}$, $N^{\phi\phi}$) portion of the trace. $N_{lm}^{E_1}$ and $N_{lm}^{B_1}$ represent the mixed radial/transverse components ($N^{r\theta}$, $N^{r\phi}$), $N_{lm}^{E_2}$ and $N_{lm}^{B_2}$ are symmetric transverse traceless components. Using the definition of the divergence of a dyad in the TSH basis (Equation (A.44)), the three resulting components can be written as the following set of 1D radial partial differential equations for every spherical harmonic degree and azimuthal order (l, m).

$$\begin{aligned}
[\nabla \cdot \mathbf{N}]_{lm}^r &= \frac{1}{r^2} \frac{\partial}{\partial r} (r^2 N_{lm}^{L_0}) - \frac{1}{r} (l(l+1)N_{lm}^{E_1} + N_{lm}^{T_0}) , \\
[\nabla \cdot \mathbf{N}]_{lm}^{(1)} &= -l(l+1) \left[\frac{1}{r^3} \frac{\partial}{\partial r} (r^3 N_{lm}^{E_1}) + \frac{1}{r} \left(\frac{N_{lm}^{T_0}}{2} - (l-1)(l+2)N_{lm}^{E_2} \right) \right] , \\
[\nabla \cdot \mathbf{N}]_{lm}^{(2)} &= -l(l+1) \left[\frac{1}{r^3} \frac{\partial}{\partial r} (r^3 N_{lm}^{B_1}) - \frac{(l-1)(l+2)}{r} N_{lm}^{B_2} \right] .
\end{aligned}$$

The three orthogonal components ($[\nabla \cdot \mathbf{N}]^r$, $[\nabla \cdot \mathbf{N}]^{(1)}$, $[\nabla \cdot \mathbf{N}]^{(2)}$) form a 3D coordinate system using the vector spherical harmonic basis (VSH) basis outlined in Appendix A, Section A.1;

$$\nabla \cdot \mathbf{N} = \sum_{m=-lmax}^{lmax} \sum_{l=|m|}^{lmax} \left([\nabla \cdot \mathbf{N}]_{lm}^r \mathbf{Y}_{lm} + [\nabla \cdot \mathbf{N}]_{lm}^{(1)} \mathbf{\Psi}_{lm} + [\nabla \cdot \mathbf{N}]_{lm}^{(2)} \mathbf{\Phi}_{lm} \right) .$$

\mathbf{Y}_{lm} , $\mathbf{\Psi}_{lm}$, and $\mathbf{\Phi}_{lm}$ represent the radial and two transverse spherical harmonic unit vectors, respectively. The divergence of the material derivative ($\nabla : \mathbf{N}$) in this basis is defined by the 1D radial PDE—Equation (A.40) in Appendix A.

$$\nabla : \mathbf{N} = \sum_{m=-lmax}^{lmax} \sum_{l=|m|}^{lmax} \left(\frac{1}{r^2} \frac{\partial}{\partial r} (r^2 [\nabla \cdot \mathbf{N}]_{lm}^r) - \frac{l(l+1)}{r} [\nabla \cdot \mathbf{N}]_{lm}^{(1)} \right) Y_{lm} . \quad (3.21)$$

The scalar divergence of the linearized material derivative dyad (Equation (3.21)) can be plugged into the conservation of momentum (Equation (3.2)), capturing the effects of a compressible background momentum field on the potential flow.

3.6.6 Rotating reference frame

The governing equations (Equations (3.1)-(3.1)) can be solved in a non-inertial rotating reference frame, whose angular velocity ($\boldsymbol{\Omega}$) is defined in spherical coordinates as:

$$\boldsymbol{\Omega} = \Omega \cos(\theta) \hat{\mathbf{r}} + \Omega \sin(\theta) \hat{\boldsymbol{\theta}} . \quad (3.22)$$

The pseudo-forces relating to rotation in the conservation of momentum (Equation (3.2)) are grouped into R'_{Υ} , consisting of the Coriolis force ($R'_C = 2\boldsymbol{\Omega} \times \mathbf{m}'$) and Centrifugal force ($R'_F = \rho' \boldsymbol{\Omega} \times (\boldsymbol{\Omega} \times \mathbf{r})$), where $R'_{\Upsilon} = -\nabla \cdot R'_F - \nabla \cdot R'_C$.

Using the definition of angular velocity (Equation (3.22)), the Centrifugal force can be expressed in spherical coordinates as follows.

$$R'_F = \rho' \boldsymbol{\Omega} \times (\boldsymbol{\Omega} \times \mathbf{r}) = -\rho' r \Omega^2 \sin^2 \theta \hat{\mathbf{r}} - \rho' r \Omega^2 \sin \theta \cos \theta \hat{\boldsymbol{\theta}} . \quad (3.23)$$

A coordinate transformation into the VSH basis can be performed using Equations (A.14), (A.15) in Appendix A.

$$\begin{aligned} R'^r_F &= -\rho' r \Omega^2 \sin^2 \theta , \\ \nabla_{\theta\phi}^2 R'^{\eta'}_F &= -r \Omega^2 \left[\cos \theta \left(\sin \theta \frac{\partial \rho'}{\partial \theta} \right) + 2\rho' - 3\rho' \sin^2 \theta \right] , \\ \nabla_{\theta\phi}^2 R'^{\mu'}_F &= r \Omega^2 \cos \theta \frac{\partial \rho'}{\partial \phi} . \end{aligned}$$

The transverse derivatives and trigonometric functions can be computed in frequency space, using the recursion relations derived in Appendix B. The Coriolis force can be similarly expressed in spherical coordinates.

$$R'_C = 2\boldsymbol{\Omega} \times \mathbf{m}' = 2\Omega m^\phi \sin \theta \hat{\mathbf{r}} - 2\Omega m^\phi \cos \theta \hat{\boldsymbol{\theta}} + (2\Omega m^\theta \cos \theta - 2\Omega m^r \sin \theta) \hat{\boldsymbol{\phi}} . \quad (3.24)$$

Performing another coordinate transformation (Equations (A.14), (A.15)) on the Coriolis force (Equation (3.24)) results in the following set of VSH coefficients.

$$\begin{aligned}
R_C^r &= 2\Omega m^\phi \sin \theta , \\
\nabla_{\theta\phi}^2 R_C^\eta &= \frac{1}{\sin \theta} \frac{\partial}{\partial \theta} (\sin \theta (-2\Omega m^\phi \cos \theta)) + \frac{1}{\sin \theta} \frac{\partial}{\partial \phi} (2\Omega m^\theta \cos \theta - 2\Omega m^r \sin \theta) , \\
\nabla_{\theta\phi}^2 R_C^\mu &= \frac{1}{\sin \theta} \frac{\partial}{\partial \theta} (\sin \theta (2\Omega m^\theta \cos \theta - 2\Omega m^r \sin \theta)) + \frac{1}{\sin \theta} \frac{\partial}{\partial \phi} (2\Omega m^\phi \cos \theta) .
\end{aligned}$$

The transverse relations (R_C^η, R_C^μ) can be written in a form that is consistent with the recursion relations defined in Appendix B, by multiplying both sides of the functions by $\sin^2 \theta$, and rearranging terms.

$$\begin{aligned}
R_C^r &= 2\Omega m^\phi \sin \theta , \\
\sin^2 \theta \nabla_{\theta\phi}^2 R_C^\eta &= -2\Omega \cos \theta \left(\sin \theta \frac{\partial}{\partial \theta} (m^\phi \sin \theta) \right) + 2\Omega \sin^2 \theta (m^\phi \sin \theta) \\
&\quad + 2\Omega \frac{\partial}{\partial \phi} (m^\theta \cos \theta \sin \theta - m^r \sin^2 \theta) , \\
\sin^2 \theta \nabla_{\theta\phi}^2 R_C^\mu &= 2\Omega \sin \theta \frac{\partial}{\partial \theta} (m^\theta \cos \theta \sin \theta - m^r \sin^2 \theta) + 2\Omega \cos \theta \frac{\partial}{\partial \phi} (m^\phi \sin \theta) .
\end{aligned}$$

After solving for the Coriolis terms in frequency space, they can be transformed back into real space and divided by $\sin^2 \theta$, resulting in the final forms of the pseudo-force contributions in a rotating reference frame. The divergence of these terms can be taken simply by plugging them into the definition for the divergence in the VSH basis (Section A.4).

3.6.7 Stability and CFL condition

In order to perform the stability analysis and derive an approximate Courant-Friedrichs-Lewy (CFL) condition for the time-discretization scheme, the following simplified form of the governing equations (Equations (3.1)-(3.3)) is employed.

$$\begin{aligned}\frac{\partial \rho'}{\partial t} &= -\Upsilon' , \\ \frac{\partial \Upsilon'}{\partial t} &= -\nabla^2 c^2 \rho' .\end{aligned}\tag{3.25}$$

The conservation of energy (Equation (3.3)) is omitted in favor of the simple adiabatic relation for pressure perturbations, $p' = c^2 \rho'$. Background flows are removed under the assumption that they are significantly smaller than the sound speed (c), and will not affect the stability of the algorithm in the model interior. Furthermore, since sound speed only has a radial dependence and the radial grid is spaced evenly with respect to acoustic travel time (Subsection 3.6.2), the sound speed can be treated as a constant without a significant loss in precision. The simplified governing equations (Equations (3.25)) can now be combined to form the 3D wave equation for density perturbations.

$$\frac{\partial^2 \rho'}{\partial t^2} = c^2 \nabla^2 \rho' .\tag{3.26}$$

This wave equation (Equation (3.26)) can be written out in a finite-difference form that is consistent with the time-discretization scheme employed in the model (Subsection 3.6.1).

$$\frac{\rho'^{(n+1)} - 2\rho'^{(n)} + \rho'^{(n-1)}}{(\Delta t)^2} = \frac{c^2}{r^2} \frac{\partial}{\partial r} \left(r^2 \frac{\partial \rho'^{(n)}}{\partial r} \right) - \frac{l(l+1)c^2}{r^2} \rho'^{(n)} .$$

This function can be rewritten under the assumption that density perturbations take the form of the solution to the 1D radial wave equation $\left(\rho'^{(n)}(r) = \rho'_{lm}^{(n)} Y_{lm} e^{ikr} \right)$ on the discrete intervals of the radial grid. Furthermore, the transformation of this wave due to sphericity is assumed to be minimal on the order of the grid size, allowing for the omission of the imaginary term—leaving the following governing equation.

$$\frac{\rho'_{lm}{}^{(n+1)} - 2\rho'_{lm}{}^{(n)} + \rho'_{lm}{}^{(n-1)}}{(\Delta t)^2} = -c^2 k^2 \rho'_{lm}{}^{(n)} - \frac{l(l+1)c^2}{r^2} \rho'_{lm}{}^{(n)} . \quad (3.27)$$

The terms of the wave equation (Equation (3.27)) can then be rearranged as:

$$\rho'_{lm}{}^{(n+1)} + a\rho'_{lm}{}^{(n)} + \rho'_{lm}{}^{(n-1)} = 0 , \quad \text{where} \quad a = \left[(\Delta t)^2 c^2 \left(k^2 + \frac{l(l+1)}{r^2} \right) - 2 \right] .$$

This equation is rewritten under the assumption that each subsequent time-step can be expressed as a function of a previous time-step and some amplification factor

$$(\rho'_{lm}{}^{(n+1)} = z\rho'_{lm}{}^{(n)}):$$

$$z^2 \rho'_{lm}{}^{(n-1)} + za\rho'_{lm}{}^{(n-1)} + \rho'_{lm}{}^{(n-1)} = 0 .$$

The amplification factor can then be solved using the quadratic equation.

$$z = \frac{-a \pm \sqrt{a^2 - 4}}{2} . \quad (3.28)$$

For damping to occur, the amplification factor must be complex, leaving the following condition on the terms inside of the square root.

$$a^2 - 4 < 0 .$$

Written out in full form, this condition results in the maximum time-step allowed to maintain stability.

$$\Delta t < \frac{2}{c \left(k^2 + \frac{l(l+1)}{r^2} \right)^{1/2}} ,$$

where the wavenumber k can be estimated for each grid point as $k = \pi/\Delta r$.

3.6.8 Parallelization

In order to increase the speed of the computation of the governing equations (Equations (3.1)-(3.3)), the load can be distributed over several processors working in parallel. Computations occur in two main regimes: real-space computation and frequency-space computation in the spherical harmonic decomposition.

Real-space computations include instances of multiplying and dividing flow field variables. This work is done on the Gauss-Legendre 3D mesh grid (Subsection 3.6.3), covering the full sphere in the azimuth ($0 \leq \phi \leq 2\pi$) with N_ϕ grid points, and the latitude ($0 \leq \theta \leq \pi$) with N_θ grid points. The resolution of each radial layer is controlled independently and real-space computations are done on each layer separately.

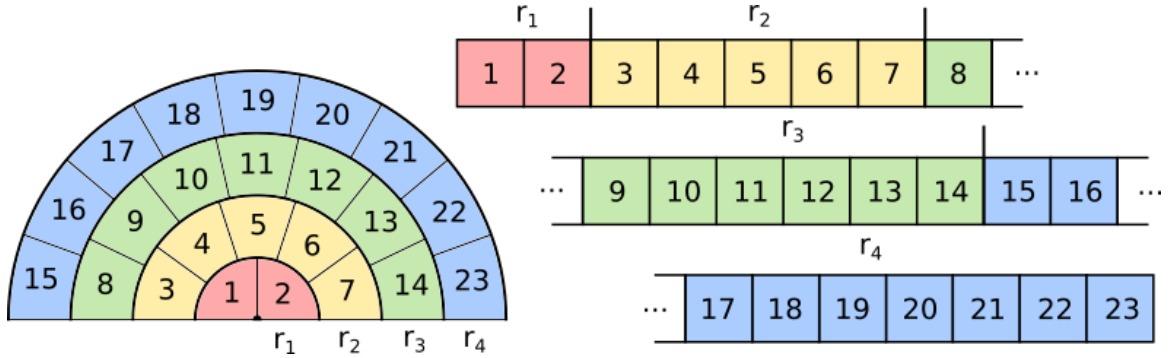


Figure 3.7 A representation of real-space mesh-point storage in memory; a 1D array of contiguous radial layer grid points ($N_\phi \times N_\theta$) are stored consecutively for each radial layer from the center outwards.

The structure of the real-space variable array is demonstrated in Figure 3.7, where each colored radial slice represents the full 2D surface grid ($N_\phi \times N_\theta$) stored as a 1D array with the resolution changing as a function of radius. The full 3D mesh is stored in memory as a single 1D array, where each surface grid is stored contiguously. This 1D array is then separated into some number of chunks of as equal size as possible

and distributed to the various compute ranks, as demonstrated in Figure 3.8. Each radial slice must be stored in its entirety in order to perform real-space computations and subsequent spherical harmonic analysis and decomposition.

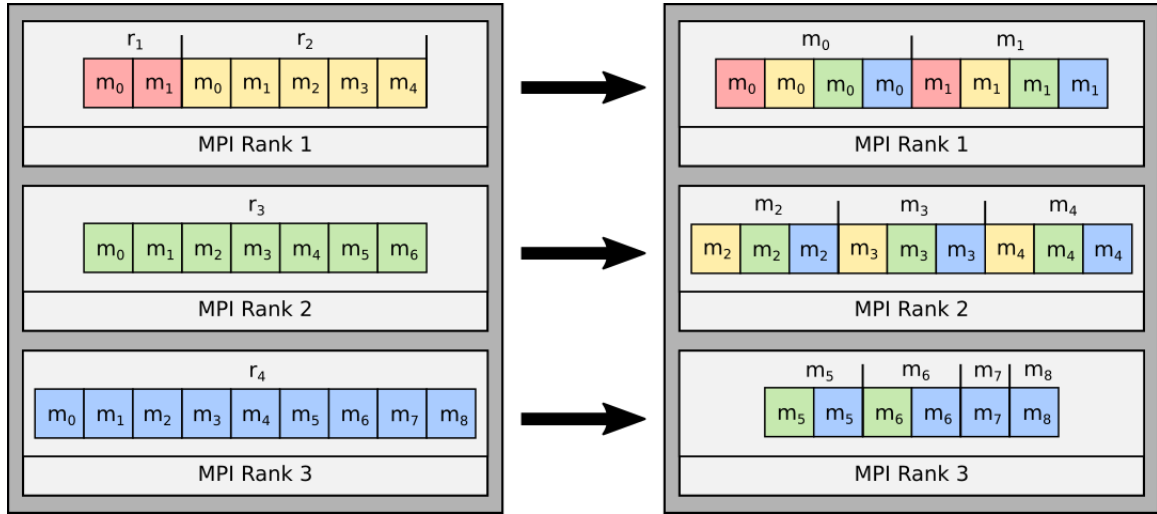


Figure 3.8 A symbolic representation of memory arrangement across compute ranks, showing the transformation between contiguous surface grids at each radial layer (left) to models separated by azimuthal quantum numbers (m) containing every radial grid-point (right).

Frequency-space computations in the spherical harmonic decomposition include solving the time-discretized functions (Subsection 3.6.1, Equations (3.12)) as well as computing the potential field using the numerical solver for Poisson’s equation (Subsection 3.6.4). These computations can be performed for each spherical harmonic degree (l) and azimuthal order (m) individually, but require access to all of their radial grid points. This can be achieved through spherical harmonic decomposition of the real-space variables in their compute ranks, as demonstrated symbolically in Figure 3.8, where, on the left hand side, each radial surface grid is transformed and stored as a 1D array of contiguous azimuthal orders (m). These 1D arrays are then broken up by that order and redistributed among the compute ranks, forming contiguous segments of radial grids for each spherical harmonic quantum number individually.

3.7 Model Validation

This section presents a validation of the computational techniques employed in the GALE code (Section 3.6). The accuracy of the computation of acoustic oscillations throughout the solar model is tested by comparing them with theoretically computed acoustic eigenmodes in Subsection 3.7.1. The computation of the material derivative (see Subsection 3.6.5) is validated by simulating differential rotation as a background velocity term, and measuring the resulting frequency shifts (Subsection 3.7.2). The detection of acoustic perturbation using a power-map analysis is tested at a high resolution in order to mimic observations of small-scale structures on the solar surface (Subsection 3.7.3).

3.7.1 Power spectrum

Acoustic oscillations on the solar surface can be decomposed into eigenmodes of radial velocity ($u'_r \hat{\mathbf{r}}$), representing standing waves throughout the solar interior. These modes can be conceptualized as a combination of the scalar spherical harmonic (Y_{lm}) with a frequency dependent radial order (ξ_n),

$$u'_r(r, \theta, \phi, t) = \sum_{n,l} \sum_{m=-l}^l \xi_n(r) Y_{lm}(\theta, \phi) e^{i\omega t}. \quad (3.29)$$

The power spectrum of these modes can be visualized using an $l-\nu$ diagram, showing continuous radial modes throughout the solar interior as a function of their frequency ($\omega = 2\pi\nu$) and spherical harmonic degree (l), Figure 3.9. The eigenmodes are excited in the frequency range determined by the source function (S , see Section 3.4). Setting negative values of the Brunt-Väisälä frequency to zero removes the convective instabilities that act as sources of acoustic perturbations normally seen below 2 mHz. The structure of the eigenmodes generated by the model shows a good agreement

with theoretical calculations of eigenmodes from the model S (Christensen-Dalsgaard et al., 1996), denoted by the dashed blue lines in Figure 3.9.

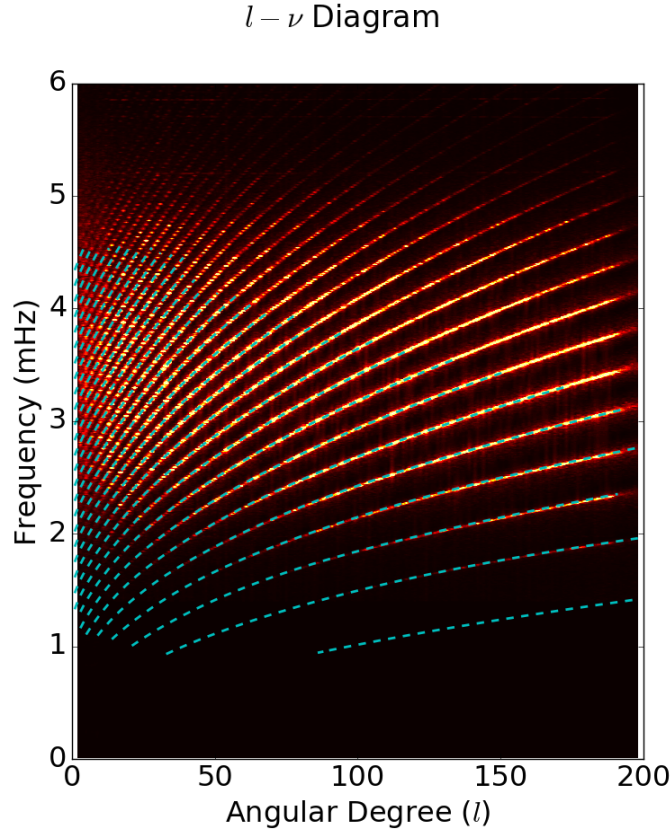


Figure 3.9 An $l - \nu$ diagram, showing the power spectrum of p-modes sampled 20 km above the model surface. Blue dashed lines represent theoretical predictions of eigenmodes made by the standard solar model S (Christensen-Dalsgaard et al., 1996). *Source: adapted from Stejko et al. (2021a).*

3.7.2 Rotation

In order to test the computation of the material derivative (Subsection 3.6.5), a simple model of differential rotation in a non-rotating reference frame can be implemented by defining the background velocity term as the angular frequency (Ω) derived from the mean-field model M1 described in Pipin & Kosovichev (2019) and shown in Figure 3.10.

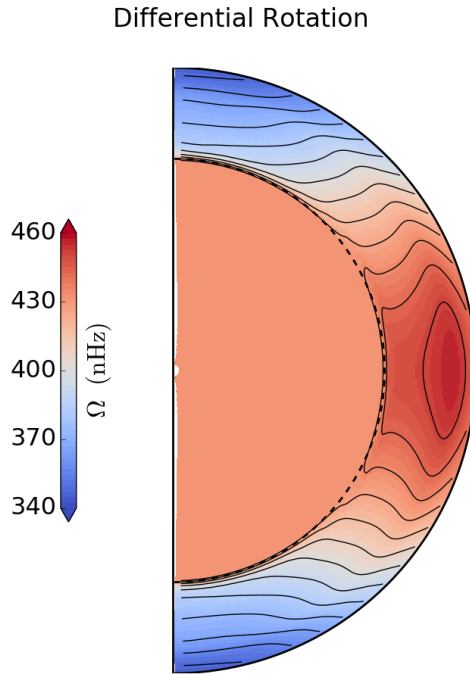


Figure 3.10 The angular frequency (Ω) profile derived from model M1, described in Pipin & Kosovichev (2019), showing differential rotation in the convection zone ($0.70R_{\odot} - 1.0007R_{\odot}$) with a solid rotating core ($< 0.70R_{\odot}$).
Source: adapted from Stejko et al. (2021a).

This simple azimuthal velocity flow field model creates easily detectable rotational splitting in the structure of the eigenmodes. The rotational profile will shift up the frequency of prograde modes and shift down the frequency of retrograde modes as a function of their azimuthal order (m). This shift can be visualized using an $m - \nu$ diagram of the power spectrum for spherical harmonic degree $l = 180$ (Figure 3.11), where the simulated modes reproduce the characteristic tilt due to the average rotation, along with the curvature created by the differential rotation in the convection zone. The blue dashed lines show frequency splittings calculated using helioseismic sensitivity kernels (Schou et al., 1998) for the M1 model (Pipin & Kosovichev, 2019).

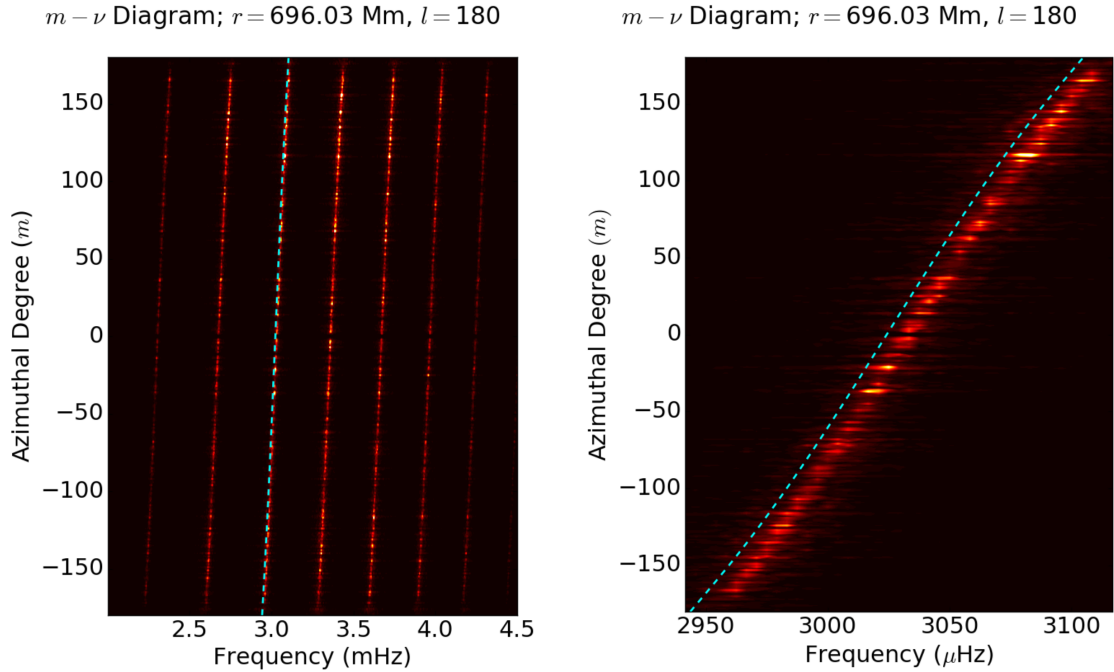


Figure 3.11 An $m - \nu$ diagram, showing the power spectrum of acoustic oscillation, sampled 30 km above the model surface, for spherical harmonic degree $l = 180$. Blue dashed lines represent frequency splittings calculated using helioseismic sensitivity kernels (Schou et al., 1998) for the M1 model (Pipin & Kosovichev, 2019).
Source: adapted from Stejko et al. (2021a).

3.7.3 Sound speed perturbations

The modeling of subsurface sound speed perturbations can be used as a general proxy for the measurement of magnetic flux emerging onto the solar surface (Hartlep et al., 2011; Ilonidis et al., 2013). In order to further validate the computational techniques presented here, this algorithm is used to simulate the observation of sound speed perturbations in a similar manner to the power-map analysis of the acoustic solar model presented in Hartlep et al. (2011). Such global acoustic models can be used as validation tools to test local helioseismology techniques used for the measurement of travel-time differences in the presence of emerging active regions (Ilonidis et al., 2013; Stefan et al., 2021). These regions can be simulated using the following 3D spherical

Gaussian perturbations (Equation (3.30)) in the background profiles of sound speed (c , in Equation (3.3)).

$$\frac{c(r, \theta, \phi)}{c_0} = 1 + A \exp \left(-\frac{(r(\theta - \theta_0))^2 + (r \sin \theta (\phi - \phi_0))^2 + (r - R_\odot + z_0)^2}{2w_0^2} \right), \quad (3.30)$$

where w_0 is the characteristic width of the 1D Gaussian function, θ_0 and ϕ_0 are the transverse coordinates of the perturbation, and z_0 is the depth from the solar surface. c_0 is the unperturbed solar sound speed profile.

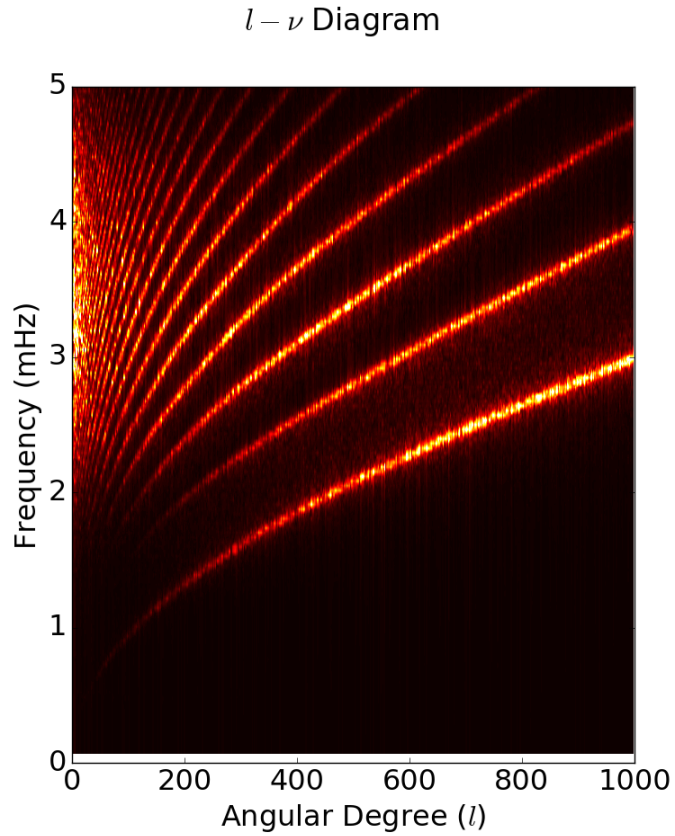


Figure 3.12 An $l - \nu$ diagram for a spectral resolution of $l_{max} = 1000$, showing the power spectrum of p-modes sampled 20 km above the model surface.

The analysis of active regions is performed on a scale of an order of magnitude smaller than investigations of global structures such as differential rotation and

meridional circulation; helioseismic measurements are taken from MDI data, with a spatial resolution of 0.12° per pixel and a time cadence of one minute. To match this resolution, the maximum spherical harmonic degree of the algorithm is set to $l_{max} = 1000$, corresponding to $N_\phi = 3000$ azimuthal, and $N_\theta = 1500$ latitudinal grid points. The data is saved every minute for 8 hours of model time—corresponding to approximately a day in computational walltime. The resulting $l-\nu$ diagram is shown in Figure 3.12.

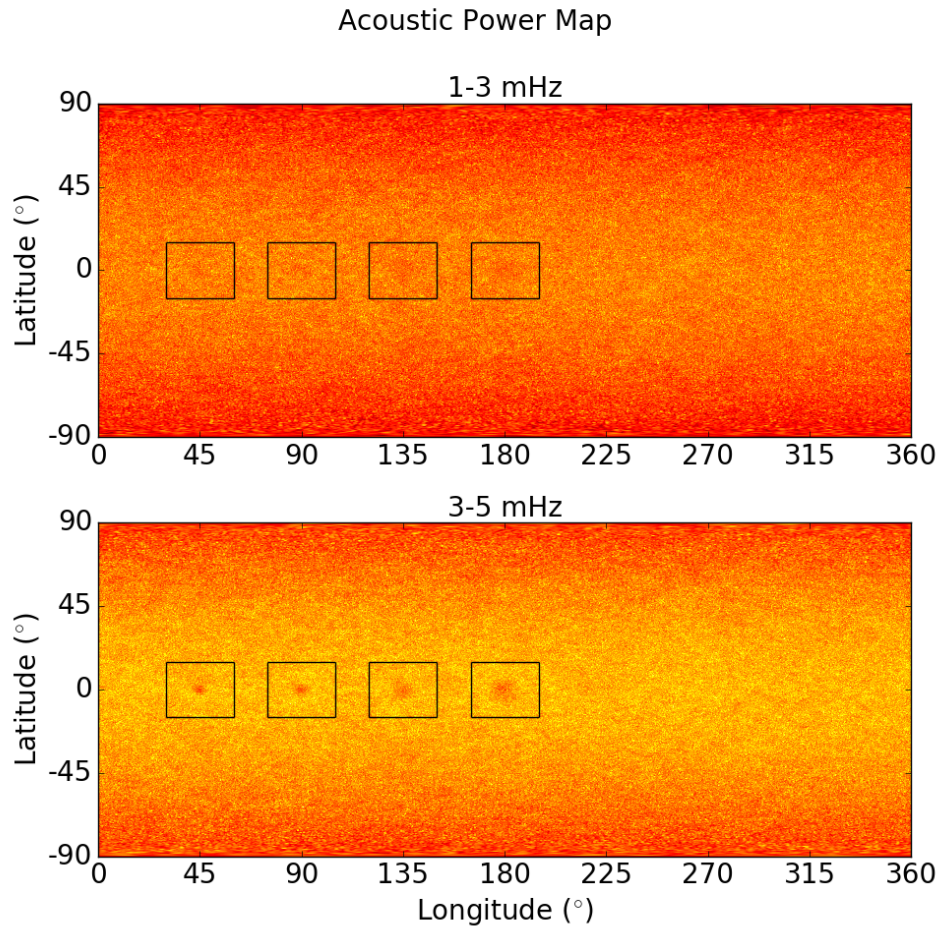


Figure 3.13 The acoustic power map generated by a summation of Fourier decomposed modes over the frequency intervals: 1-3 mHz (top) and 3-5 mHz (bottom), sampled 30 km above the solar surface. Boxes highlight four sound speed perturbations of varying widths, $w_0 = 20, 30, 40,$ and 50 Mm.

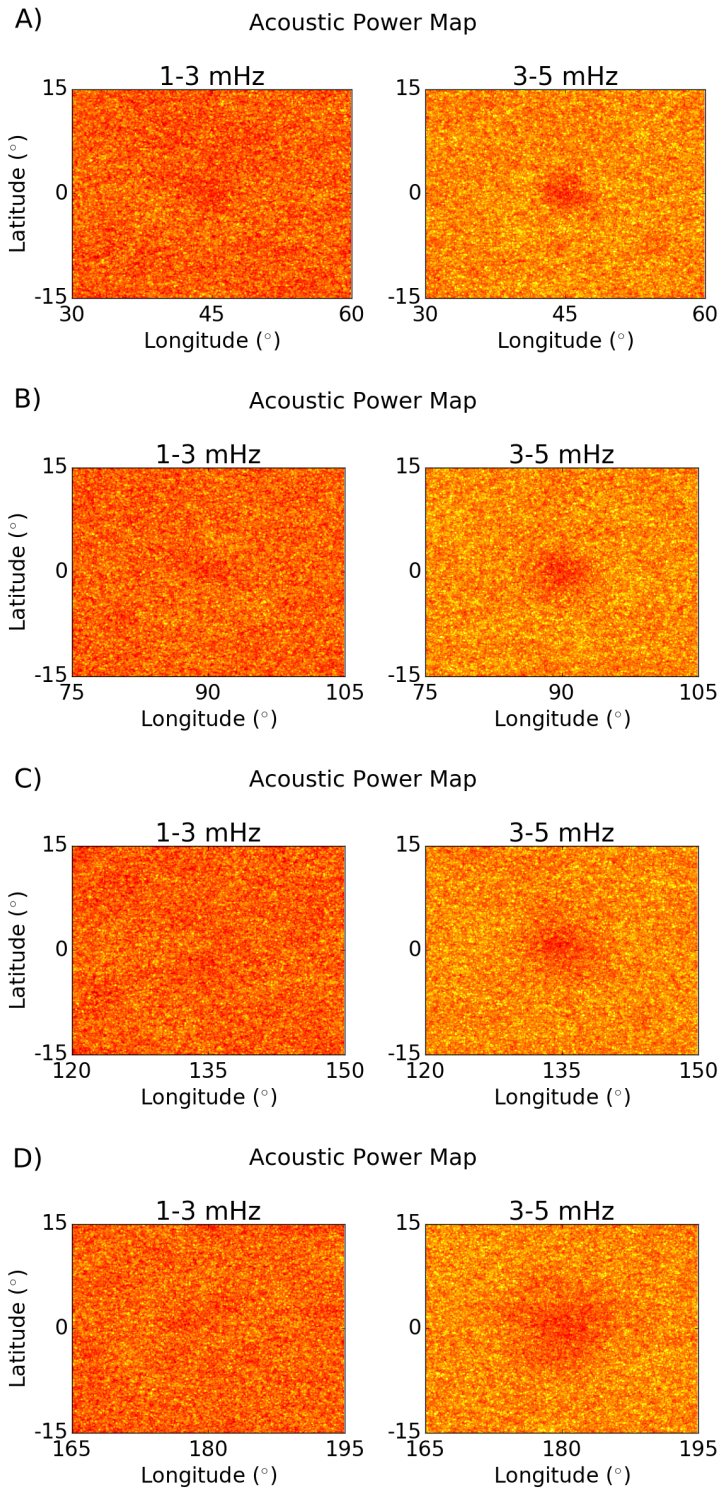


Figure 3.14 Acoustic power maps of sound speed perturbations, over the frequency intervals: 1-3 mHz (left) and 3-5 mHz (right), remapped into $30^\circ \times 30^\circ$ patches centered at the equator and the 45° (A), 90° (B), 135° (C), 180° (D) longitude, corresponding to a width of $w_0 = 20$ (A), 30 (B), 40 (C), 50 (D) Mm.

Four different active regions are tested, all corresponding to an amplitude of $A = -10\%$ and a width of $w_0 = 20, 30, 40,$ and 50 Mm. They are placed at varying depths of $z_0 = 10, 15, 20,$ and 25 Mm, at the equator and corresponding to a longitude of $\phi_0 = 45^\circ, 90^\circ, 135^\circ,$ and 180° , respectively. Acoustic perturbations can be detected on the solar surface using a power-map analysis of radial velocity perturbations (u'_r)—decomposed into Fourier modes and summed over frequency intervals (Hartlep et al., 2011; Toriumi et al., 2013). A synoptic power map for 1-3 mHz and 3-5 mHz can be seen in Figure 3.13.

These structures are visualized in detail in Figure 3.14, showing the two frequency ranges remapped into $30^\circ \times 30^\circ$ patches using Postel’s projection. These panels show the expected decrease in acoustic power footprints, corresponding to the varying width of the emerging sound speed perturbations—with the majority of the changes concentrated in the 3-5 mHz frequency range (Hartlep et al., 2011). These perturbations are representative of an approximate cross-section of strong active regions of various sizes, emerging onto the solar surface. This analysis reproduces the ability to detect relatively short-lived (~ 8 hours) structures using the power of acoustic modes.

The simulation presented in this section reproduces the results of the investigation of Hartlep et al. (2011), validating the methods used in this acoustic solar model, as well as serving as a foundation for testing the algorithm at high spectral resolutions. This analysis demonstrates potential uses for the code in the small-scale examination of near-surface active regions within a reasonable modeling time frame, something that has been too computationally expensive with previous iterations of global acoustic models.

CHAPTER 4

HELIOSEISMIC ANALYSIS

4.1 Model Parameters

Helioseismic analysis is performed on models of meridional circulation with the following parameter set-up. The spatial resolution of the model is set by the spherical harmonic degree $l_{max} = 200$. This value corresponds to an azimuthal resolution of $N_\phi = 600$ and a latitudinal resolution of $N_\theta = 450$, chosen to avoid aliasing errors during sampling. This resolution allows for the detection of signals throughout the convection zone to an upper limit of $\sim 0.96R_\odot$. The temporal cadence of the model is 3 seconds with data being saved at 1 minute intervals for a total of 67 hours (4000 minutes)—a time-scale too short to effectively resolve signals in the convection zone (Braun & Birch, 2008). The signal-to-noise ratio (SNR) can be improved by increasing the background velocities in the model by a factor of 36 (see Hartlep et al. (2013)), mimicking the SNR expected in approximately a decade of solar observations—within the operational time-frame of HMI.

4.2 Deep Focusing Method

Acoustic oscillations traveling through the solar interior are advected by regimes of mean mass-flows in the convection zone. Measuring perturbations on the solar surface allows for the application of local helioseismology techniques (see Gizon & Birch (2005)) in order to infer the structure of these internal flow velocities. This analysis employs the technique of deep focusing (Zhao et al., 2009; Charbonneau, 2010), in which radial velocity perturbations at two points on the model surface, separated by some angular distance (Δ), are cross-correlated. The resulting correlation signal forms the characteristic profile of a Gabor wavelet (Kosovichev & Duvall, 1997; Giles, 2000; Nigam et al., 2007), which can be described by the function:

$$\Psi(\tau, \Delta) \propto \sum_{\delta v} \cos \left[\omega_0 \left(\tau - \frac{\Delta}{v} \right) \right] \exp \left[-\frac{\delta \omega^2}{4} \left(\tau - \frac{\Delta}{u} \right)^2 \right]. \quad (4.1)$$

τ is the time-lag between the signals, ω_0 and $\delta\omega$ are the central frequency and width of the frequency filter respectively. $v = \omega/\sqrt{l(l+1)}$ is the horizontal phase velocity and $u = \partial\omega/\partial k_h$ is the horizontal group velocity. The function is summed over the narrow range of phase velocities δv . Fitting this function (Equation (4.1)) to the cross-correlated signal is done using the iterative Levenberg-Marquardt method, resulting in an estimate of the time-lag from the group and phase velocities.

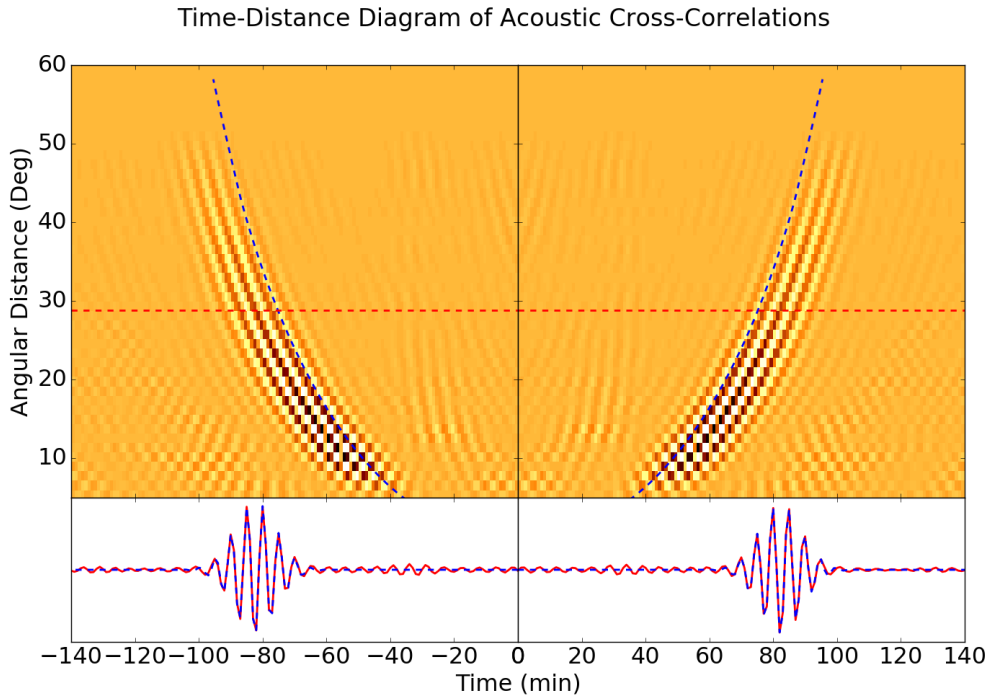


Figure 4.1 Time-distance diagram of the cross-correlation of radial velocity perturbations for a range of angular travel distances ($\Delta = 5^\circ - 60^\circ$), sampled 300 km above the solar surface. Bottom figures show a slice of the correlation signal at the red dashed line in the time-distance diagram, fit to a Gabor wavelet pattern (Equation (4.1)).

In order to measure the impact of meridional flow fields on acoustic rays, the time-lag (τ) of southward traveling waves is subtracted from their northward traveling counterparts ($\delta\tau_{NS}$). The ray-path approximation (Giles, 2000) then offers a basis for inferring the magnitude of the velocity field in the direction of the traveling acoustic ray (assuming the path of the ray Γ_0 remains unperturbed).

$$\delta\tau = -2 \int_{\Gamma_0} \frac{\mathbf{u} \cdot \mathbf{n}}{c^2} ds . \quad (4.2)$$

Although this function omits non-linear effects of large flow velocities, it serves as a basic approximation of travel-time differences—seen by the computed travel-time comparisons in Figure 4.12.

This method is applied to the surface mesh-grid of the model, sampled at approximately 300 km above the photosphere ($1.0004R_\odot$). Each pixel ($N_\theta \times N_\phi = 450 \times 600$) is treated as a center point around which cubic hermite splines are used to remap a $60^\circ \times 60^\circ$ patch into azimuthal equidistant coordinates (Postel’s projection) at a resolution of approximately 0.6° per pixel. Great circle distances (Δ) are selected at every interval (1.2°) from 0° to 60° , for which 30° wide sectors in the north and south (two pixels in radius) are averaged and cross-correlated with each other. This signal can be enhanced by averaging over every point in the longitude ($N_\phi = 600$) and smoothed by averaging $\pm 3^\circ$ (± 5 pixels) in the latitude. The data can be smoothed further by averaging the diameter of each great circle over $\pm 2.4^\circ$, where travel-time offsets are interpolated to an estimated time-lag using the ray-path approximation. The application of this method allows for the measurement of acoustic travel times and inferences of meridional velocities throughout the convection zone—from the convective-radiative interface at the tachocline ($0.70R_\odot$) to near the solar surface ($0.96R_\odot$). An illustration of the remapping and pixel selection technique, along with corresponding acoustic ray-paths through the model interior can be seen in Figure 4.2.

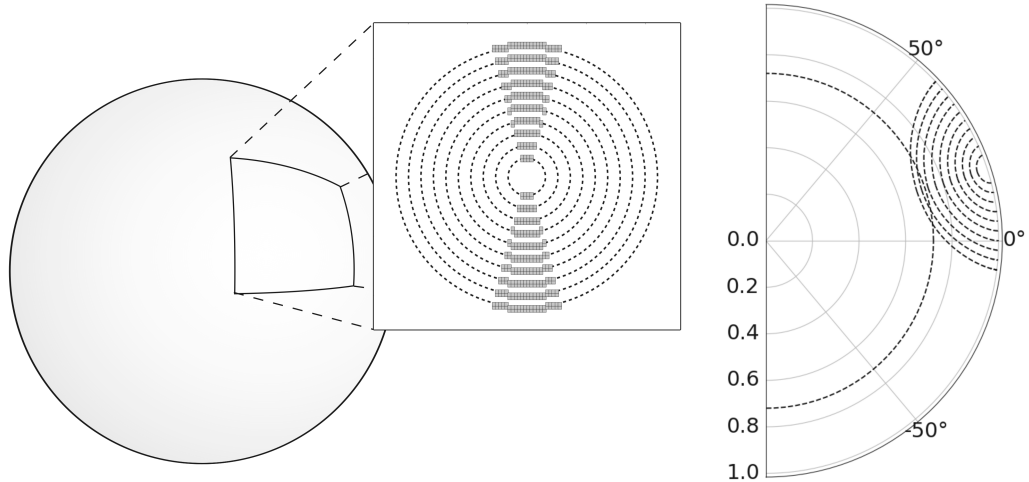


Figure 4.2 An illustration of the deep-focusing method. Left) A $60^\circ \times 60^\circ$ patch is remapped into azimuthal equidistant coordinates, pixels are selected in 30° wide northern and southern sectors (two pixels in radius). Right) The acoustic ray paths associated with the selected travel distances.

Source: adapted from Stejko et al. (2021b).

4.3 Measuring Acoustic Travel Times

In order to validate the computational techniques used in the GALE algorithm, the deep-focusing method is tested on the same simple model of shallow single-cell meridional circulation presented in Hartlep et al. (2013). Following their formulation, travel-time differences are taken from great circle distance intervals at $\Delta = 12^\circ, 18^\circ, 24^\circ, 30^\circ, 36^\circ$. The radial turning points of acoustic waves corresponding to each angular distance are $\sim 0.93, 0.89, 0.85, 0.81, 0.77, 0.72 R_\odot$, respectively. Figure 4.3 shows the meridional flow profile used in the model with dashed lines in the upper hemisphere corresponding to the ray paths for each great circle.

The travel-time differences ($\delta\tau_{NS}$) for each ring diameter are plotted as a function of latitude in Figure 4.4. These values are compared to theoretical travel-time differences (dashed lines in Figure 4.4) computed using the ray-path approximation (Equation (4.2)) employing the standard solar model S (Christensen-Dalsgaard et al., 1996). These travel-time differences show solid agreement with theoretical predictions

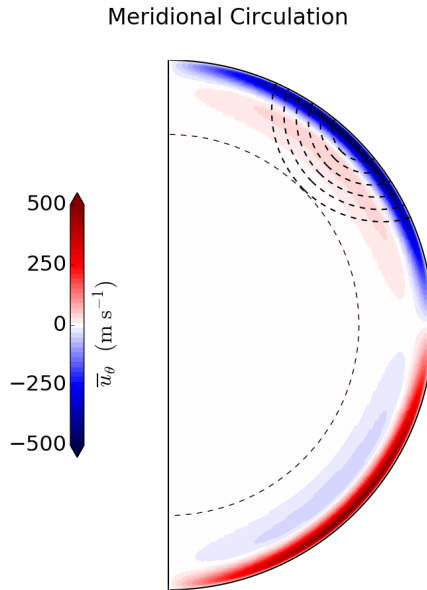


Figure 4.3 The latitudinal velocity (\tilde{u}_θ) of a single-cell model of meridional circulation (Hartlep et al., 2013). The dashed lines represent ray paths of acoustic oscillations (p-modes) between diameters of $\Delta = 12^\circ, 18^\circ, 24^\circ, 30^\circ, 36^\circ$ and 42° with radial turning points at depths: $\sim 0.93, 0.89, 0.85, 0.81, 0.77, 0.72 R_\odot$, respectively. Meridional circulation models are amplified by a factor of 36 (see Section 4.1).

Source: adapted from Stejko et al. (2021a).

as well as the analysis of Hartlep et al. (2013). These results show a key validation of the numerical procedure used to compute the model as well as the deep focusing techniques used to analyze the data. The error (σ_{NS}) is calculated using the procedure described in Subsection 4.3.1.

In order to increase the SNR in these measurements, a phase-speed filter can be applied—defined by a Gaussian function with a width of $\sigma = 0.05v_p$, where $v_p = \omega/L$ is the phase speed, see Nigam et al. (2007) for details. Under the application of this filter, the travel-time differences display high levels precision but do show a latitude-independent systematic offset for different ring diameters. This offset, which seems to have a maximum of approximately ± 1 s (Figure 4.5), is a characteristic of the realization noise in the model and can be removed by subtracting the phase-filtered noise profile for the same model with no background flows (Subsection 4.3.1).

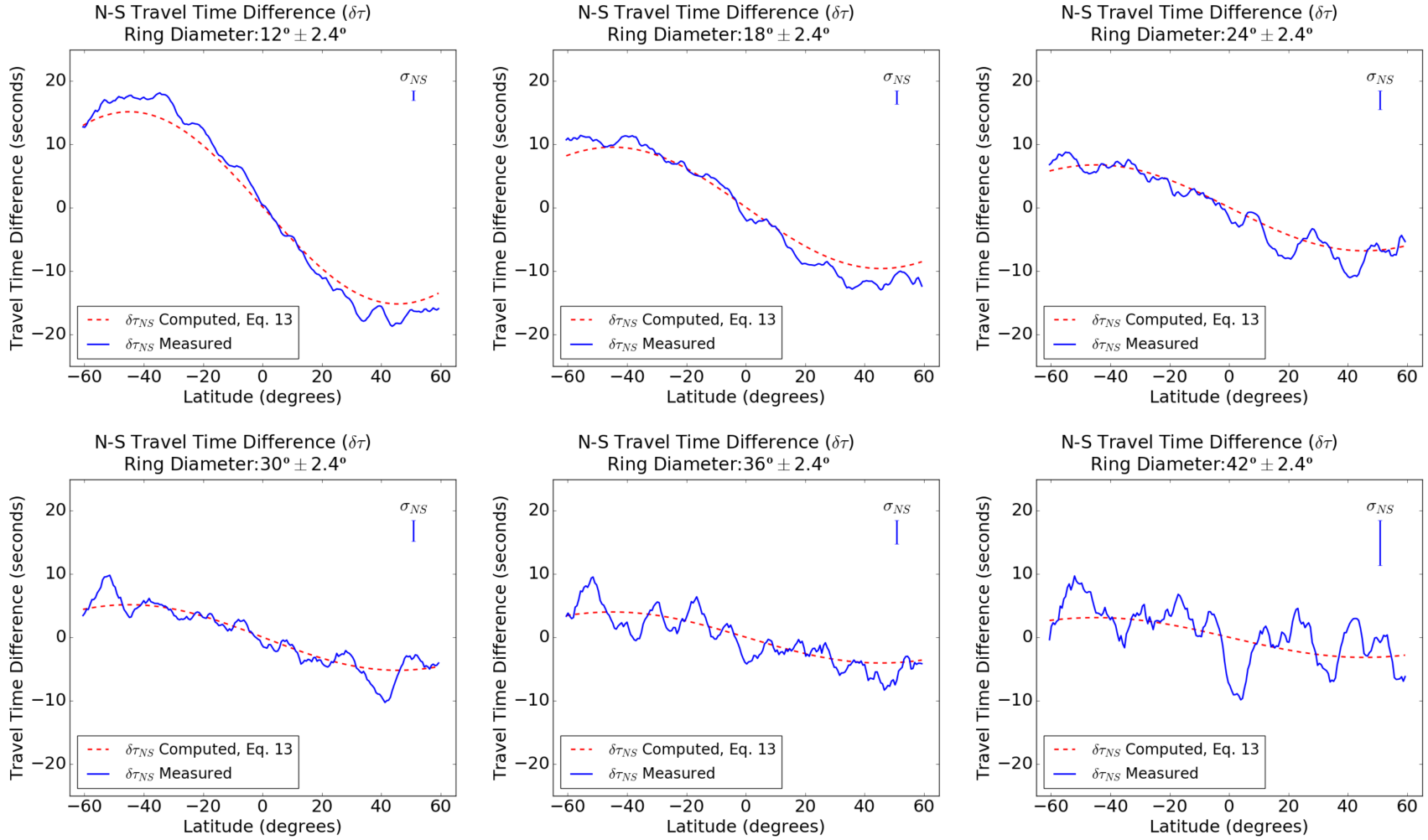


Figure 4.4 The N-S travel-time differences (δt_{NS}) as a function of latitude for six different depths: $\sim 0.93, 0.89, 0.85, 0.81, 0.77, 0.72 R_\odot$, corresponding to travel distances of $\Delta = 12^\circ, 18^\circ, 24^\circ, 30^\circ, 36^\circ$, and 42° , respectively. The signal is averaged over $\pm 3^\circ$ in latitude and $\pm 2.4^\circ$ in travel distance. Meridional circulation models are amplified by a factor of 36 (see Section 4.1).
Source: adapted from Stejko et al. (2021a).

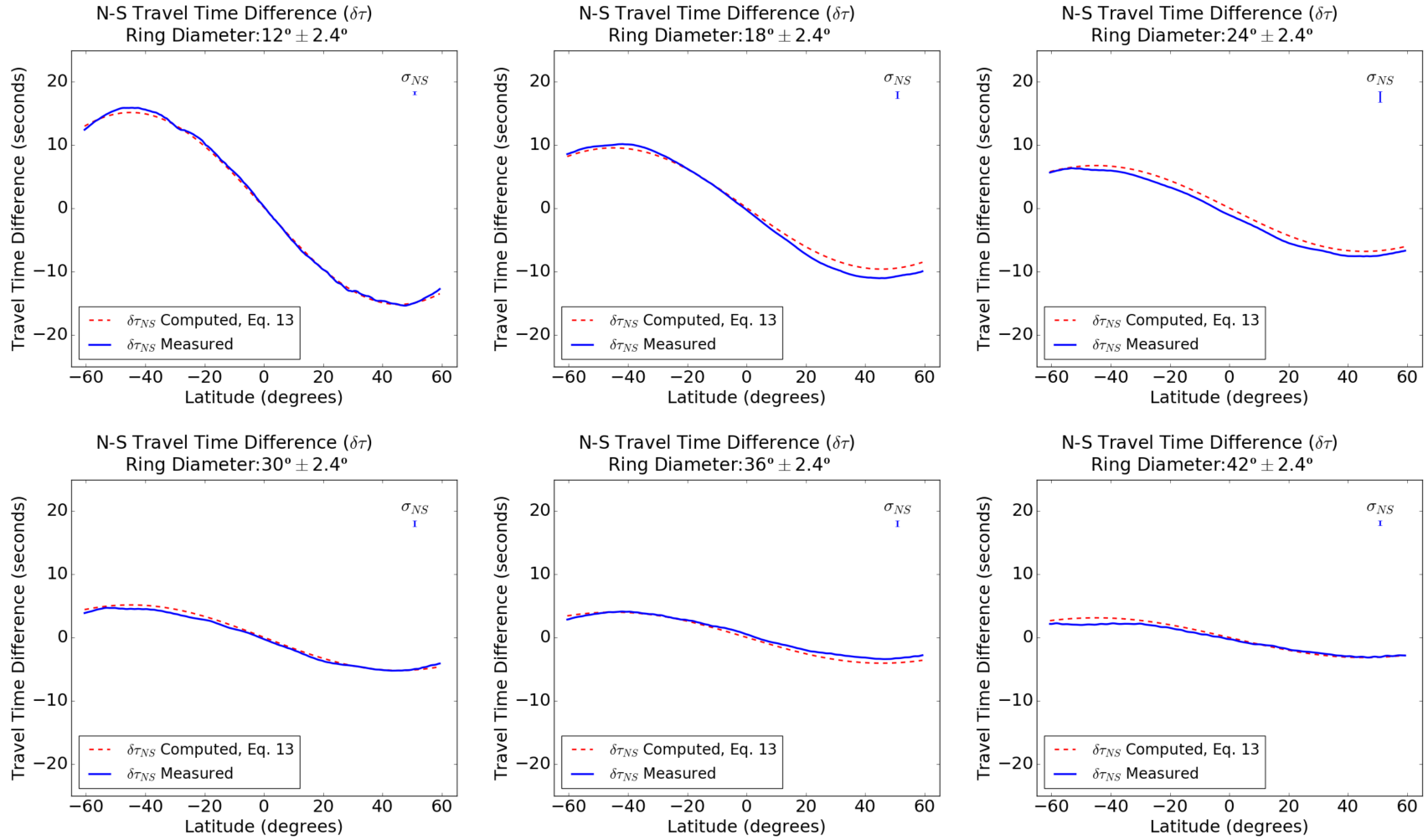


Figure 4.5 The N-S travel-time differences (δt_{NS}) under the application of a Gaussian phase-speed filter ($\sigma = 0.05v_p$) as a function of latitude for six different depths: $\sim 0.93, 0.89, 0.85, 0.81, 0.77, 0.72 R_\odot$, corresponding to travel distances of $\Delta = 12^\circ, 18^\circ, 24^\circ, 30^\circ, 36^\circ$, and 42° , respectively. The signal is averaged over $\pm 3^\circ$ in latitude and $\pm 2.4^\circ$ in travel distance. Meridional circulation models are amplified by a factor of 36 (see Section 4.1).

Source: adapted from Stejko et al. (2021a).

4.3.1 Characterizing noise

The error (σ_{NS}) is calculated using a separate model with no background flows; this reference model uses an identical source function (S , Section 3.4) and analysis sequence, producing the same error profile for each ring diameter (Figure 4.4). This error is characterized as the standard deviation of travel-time differences ($\delta\tau$) from zero in the reference model, taking the root-mean-square (RMS) over latitudinal grid points.

$$\sigma_{NS} = \sqrt{\frac{1}{N} \sum_{i=1}^N \delta\tau_i^2}. \quad (4.3)$$

The characteristic noise profiles seen in models without flows can be subtracted from measured travel-time differences (Figure 4.4) in order to remove some of the most significant impacts of realization noise on measurements (Hanasoge et al., 2007). This method of attenuating noise provides an opportunity to compare measurements made by computational helioseismology to estimates of the ray-path approximation. The resulting N-S travel-time profile is shown in Figure 4.6 for unfiltered measurements and in Figure 4.7 for measurements under the application of the phase-speed filter. These profiles show remarkable agreement with predictions made using the ray-path approximation (Equation (4.2)), implying that non-linear effects do not seem to have dramatic impacts on the measurement of travel times.

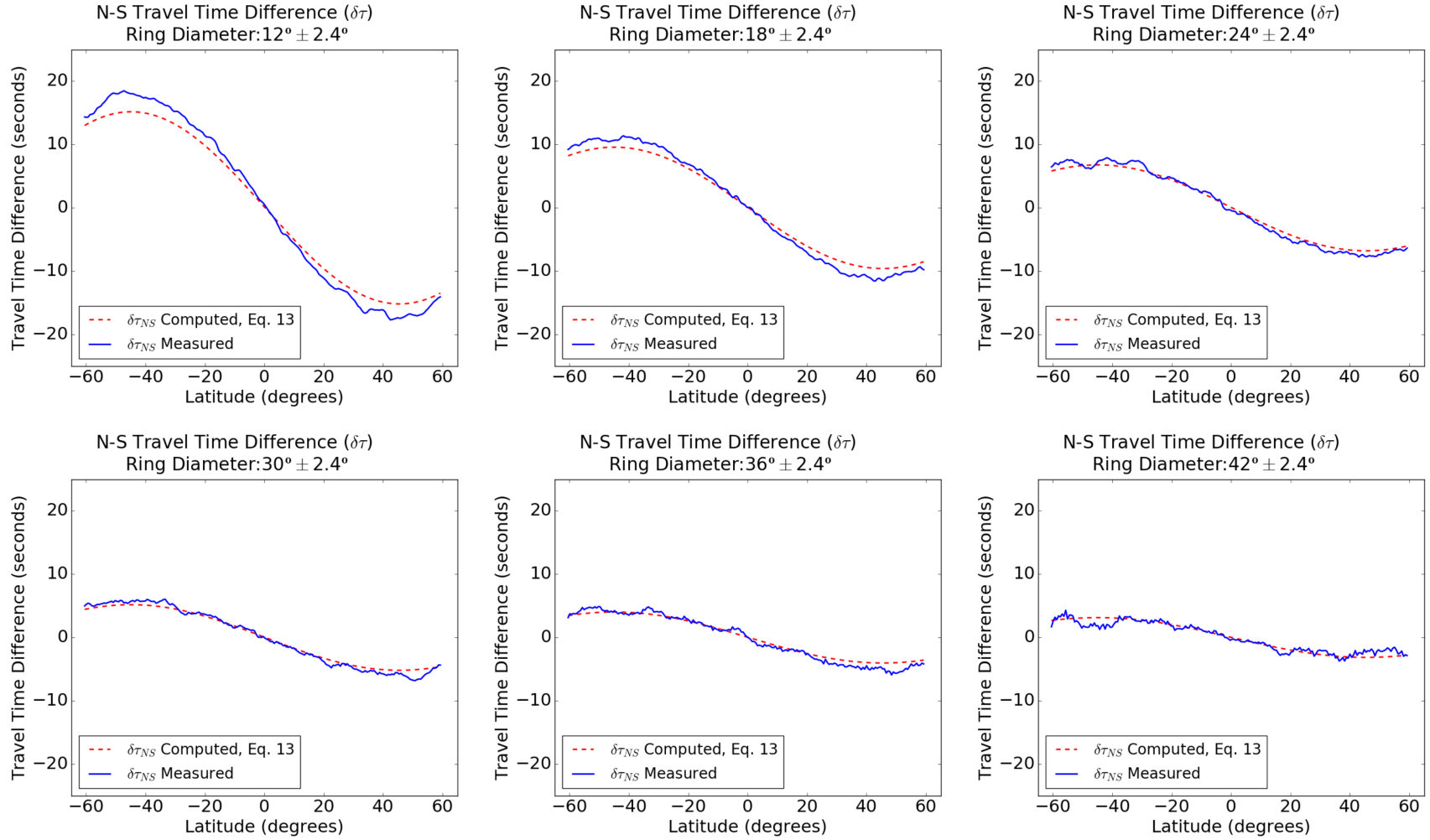


Figure 4.6 The N-S travel-time differences (δt_{NS}) with noise subtracted from the corresponding model with no flows. The travel-times are plotted as a function of latitude for six different depths: $\sim 0.93, 0.89, 0.85, 0.81, 0.77, 0.72 R_\odot$, corresponding to travel distances of $\Delta = 12^\circ, 18^\circ, 24^\circ, 30^\circ, 36^\circ$, and 42° , respectively. The signal is averaged over $\pm 3^\circ$ in latitude and $\pm 2.4^\circ$ in travel distance. Meridional circulation models are amplified by a factor of 36 (see Section 4.1).

Source: adapted from Stejko et al. (2021a).

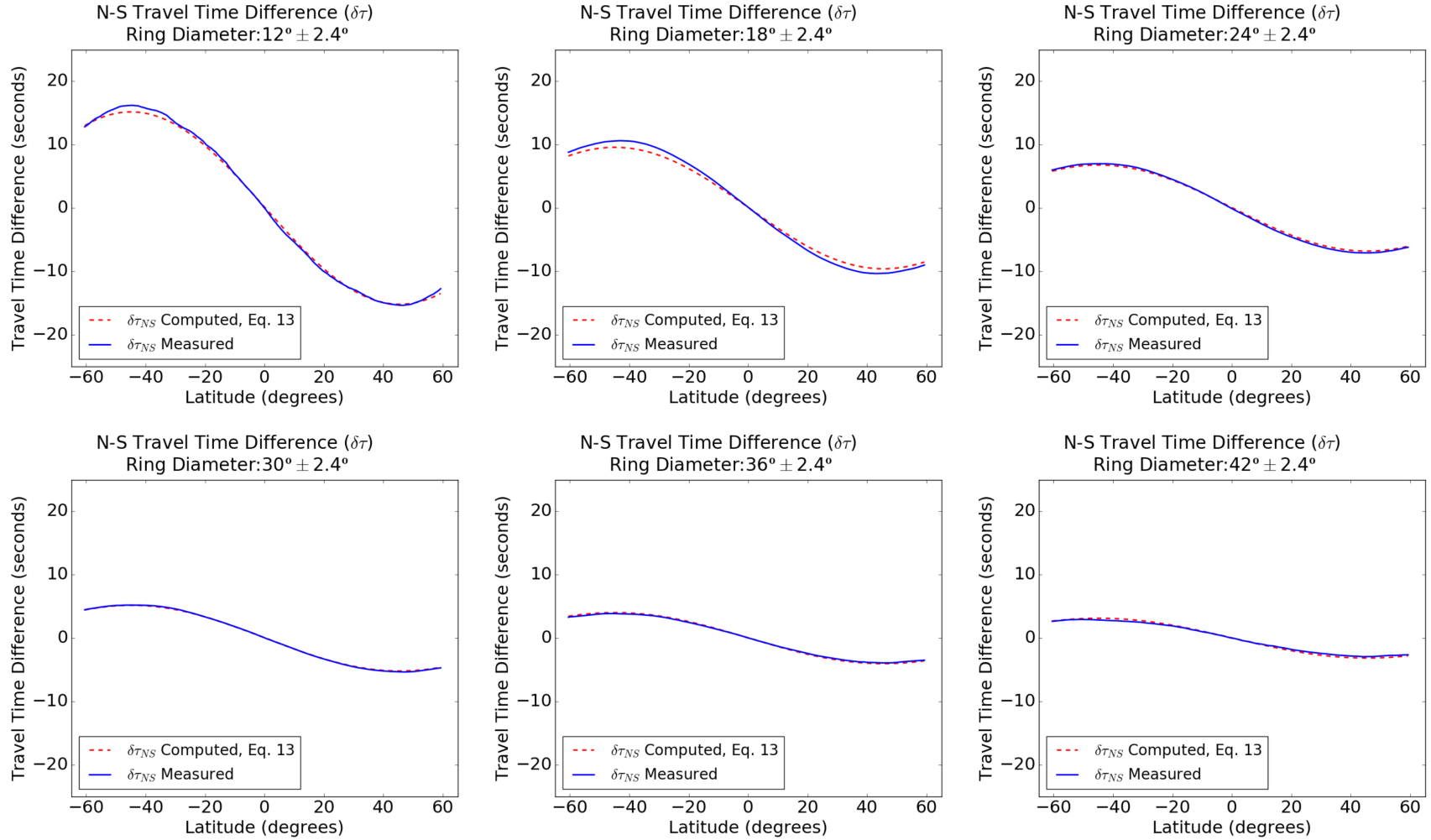


Figure 4.7 The N-S travel-time differences (δt_{NS}) under the application of a Gaussian phase-speed filter ($\sigma = 0.05v_p$) with noise subtracted from the corresponding model with no flows. The travel-times are plotted as a function of latitude for six different depths: $\sim 0.93, 0.89, 0.85, 0.81, 0.77, 0.72 R_\odot$, corresponding to travel distances of $\Delta = 12^\circ, 18^\circ, 24^\circ, 30^\circ, 36^\circ$, and 42° , respectively. The signal is averaged over $\pm 3^\circ$ in latitude and $\pm 2.4^\circ$ in travel distance. Meridional circulation models are amplified by a factor of 36 (see Section 4.1).

Source: adapted from Stejko et al. (2021a).

The error function (σ_{NS} , Equation (4.3)) provides a solid foundation for the characterization of realization noise at various acoustic travel depths. This error is shown as a function of travel distance (Δ) in Figure 4.8, along with travel-time differences ($\delta\tau$) from the reference model without background flows for five separate latitudinal averages ($30^\circ\text{N} - 50^\circ\text{N}$, $10^\circ\text{N} - 30^\circ\text{N}$, $10^\circ\text{S} - 10^\circ\text{N}$, $10^\circ\text{S} - 30^\circ\text{S}$, $30^\circ\text{S} - 50^\circ\text{S}$); errors are shown for both filtered and unfiltered signals (see Section 4.3). The cause of the apparent systematic error is unclear, however, the latitude-dependent offset is strongly linked to the structure of the source function (S , Section 3.4), with different random number seeds generating different error profiles. This effect deserves its own systematic investigation for varying parameters of source locations and structures.

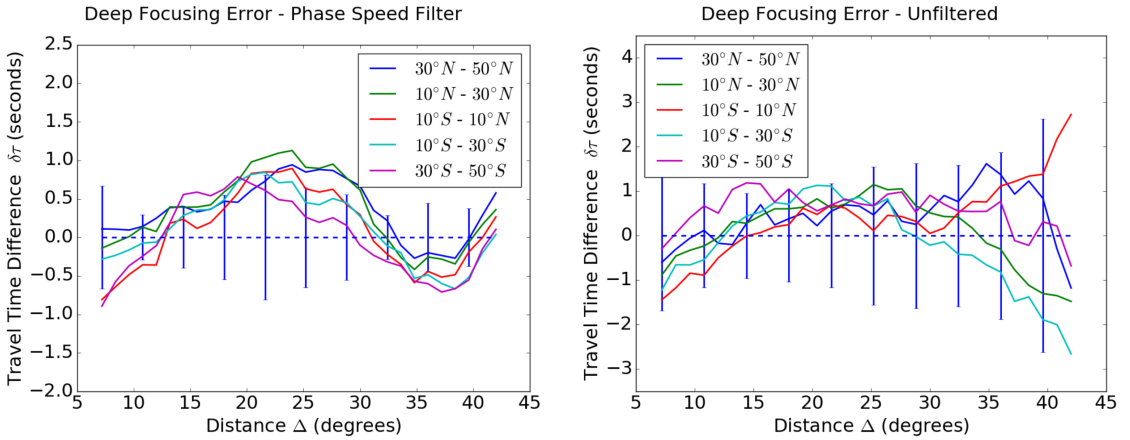


Figure 4.8 The error in travel-time differences ($\delta\tau$) as a function of travel distance (Δ) for five latitudinal averages spanning $30^\circ\text{N} - 50^\circ\text{N}$, $10^\circ\text{N} - 30^\circ\text{N}$, $10^\circ\text{S} - 10^\circ\text{N}$, $10^\circ\text{S} - 30^\circ\text{S}$, $30^\circ\text{S} - 50^\circ\text{S}$. Error bars show the standard deviation of the measured offset (σ_{NS} , Equation (4.3)) across the entire latitude. Left) Error for data analyzed with a Gaussian phase-speed filter ($\sigma = 0.05v_p$). Right) Error for unfiltered signal. *Source: adapted from Stejko et al. (2021a).*

Figure 4.8 shows similar systematic error structures in both the filtered and unfiltered signals. Moving towards greater depths, however, shows a significant increase in the noise of the unfiltered signal, concealing any potential offset. These results may have interesting implications for measuring meridional flow structures at

the base of the tachocline. The application of the phase-speed filter seems to have preserved signal quality relatively evenly throughout the convection zone, offering encouraging results for probing flows deep in the solar interior.

4.4 Analysis of Meridional Circulation

A useful application of this algorithm lies in the in-depth investigation of the propagation of acoustic waves over profiles of meridional circulation. This section explores measurements made from profiles of shallow and deep single-cell, as well as strong and weak double-cell regimes of meridional background flows—generated by the mean-field non-linear hydrodynamic and dynamo models of Pipin & Kosovichev (2018, 2019). The stochastic excitation of oscillations over background flows generated by these models allows for a systematic examination of realization noise in the helioseismic signatures generated by each regime. This investigation offers a baseline for the low-end of variance in travel-time measurements that characterize single-cell and double-cell meridional circulation—resulting from minimal parameter changes near the base of the tachocline. Previous conclusions on the nature of meridional circulation structure and the bounds of realization noise have been inferred with the aid of ad-hoc models (Zhao et al., 2013; Hartlep et al., 2013; Rajaguru & Antia, 2015; Chen, 2019; Gizon et al., 2020); this section presents the analysis of physics-based meridional velocity profiles in order to help constrain the large variance of possible internal structures.

4.4.1 Meridional profiles

The deep focusing method (Section 4.2) is applied to four profiles of meridional circulation. The first two are: a shallow single-cell profile, with a return flow at approximately $0.80R_{\odot}$, along with a double-cell meridional circulation profile with a weak reversal, referred to as M1 and M2, respectively, in Pipin & Kosovichev

(2019). The next two are: a single-cell meridional circulation model with a deep return flow situated near the base of the tachocline—based on the mean-field model of Kitchatinov (2004), along with a double-cell meridional circulation profile with a stronger return flow induced by gyroscopic pumping in the same model. They are described as models M2 and M3, respectively, in Pipin & Kosovichev (2018), and referred to as K1 and K2 here, in order to avoid confusion with the other models. These meridional velocities are used as the background terms ($\tilde{u}_r, \tilde{u}_\theta$) in the governing equations (Equations (3.1)-(3.3)). The latitudinal velocities (\tilde{u}_θ) for the models (M1, M2, K1, & K2) are shown in Figure 4.9, with streamlines representing the circulation profile.

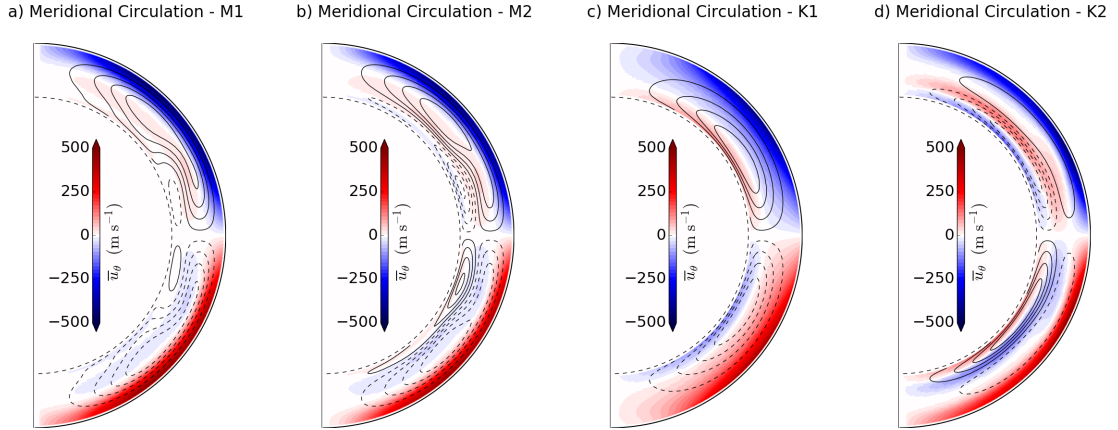


Figure 4.9 Latitudinal velocities (\tilde{u}_θ), generated by the mean-field models of Pipin & Kosovichev (2019) (M1 and M2) and Pipin & Kosovichev (2018) (K1 and K2—referred to as M2 and M3 in their paper). a) Single-cell meridional circulation with a shallow return flow at $\sim 0.80R_\odot$. b) Double-cell meridional circulation with weak reversal. c) Single-cell meridional circulation with a deep return flow near the base of the tachocline. d) Double-cell meridional circulation with strong reversal. Solid and dashed contours represent counterclockwise and clockwise rotation respectively. Meridional circulation models are amplified by a factor of 36 (see Section 4.1). *Source: adapted from Stejko et al. (2021b).*

The internal meridional flow profiles can be characterized by plotting N-S travel-time differences ($\delta\tau_{NS}$) as a function of their travel distance ($\Delta = 12^\circ -$

42°)—corresponding to an increasing depth in the convection zone ($r = 0.93R_{\odot} - 0.72R_{\odot}$). Figure 4.10 presents five latitudinal averages (30°N – 50°N, 10°N – 30°N, 10°S – 10°N, 10°S – 30°S, 30°S – 50°S) of these travel-time differences for the four regimes of meridional circulation. Measured travel-time differences (solid lines) are compared to theoretical travel-time differences (dashed lines) computed using the ray-path approximation (Equation (4.2)). Randomized functions are used to generate

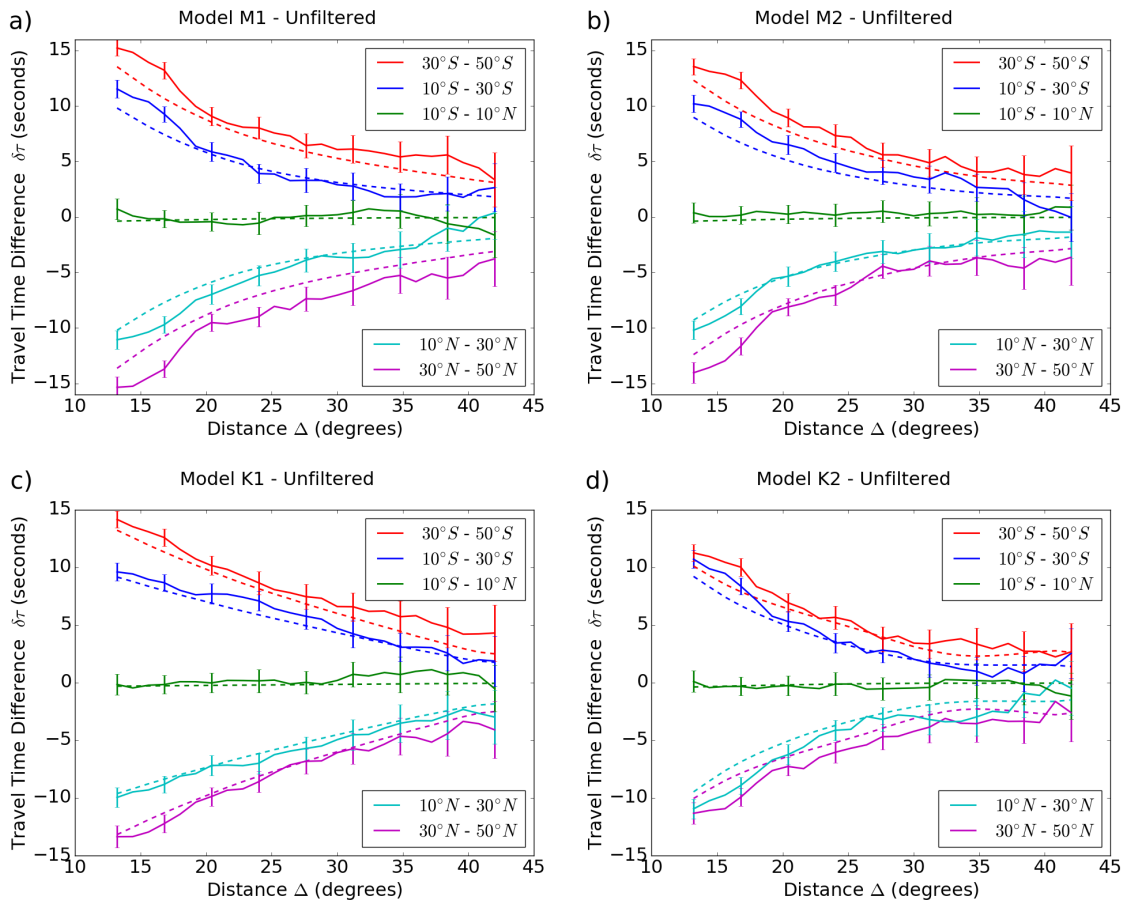


Figure 4.10 The N-S travel-time differences ($\delta\tau_{NS}$) as a function of travel distance (Δ) for models M1 (a), M2 (b), K1 (c), and K2 (d). The travel-time measurements are shown unfiltered for five latitudinal averages spanning 30°N – 50°N, 10°N – 30°N, 10°S – 10°N, 10°S – 30°S, 30°S – 50°S. Dashed lines are theoretical times computed using the ray-path approximation (Equation (4.2)). Meridional circulation models are amplified by a factor of 36 (see Section 4.1).

Source: adapted from Stejko et al. (2021b).

the oscillatory signal in the source (S , see Section 3.4)—of which four different profiles are shown for models M1, M2, K1, and K2 (Figure 4.10).

The bounds of the noise can be measured with the method described in Subsection 4.3.1; 100 unique source functions on a model with no background flows are used to characterize the noise as the standard deviation (σ_{NS} , Equation (4.3)) of the measured signal from zero. Error bars in Figure 4.10 show one standard deviation

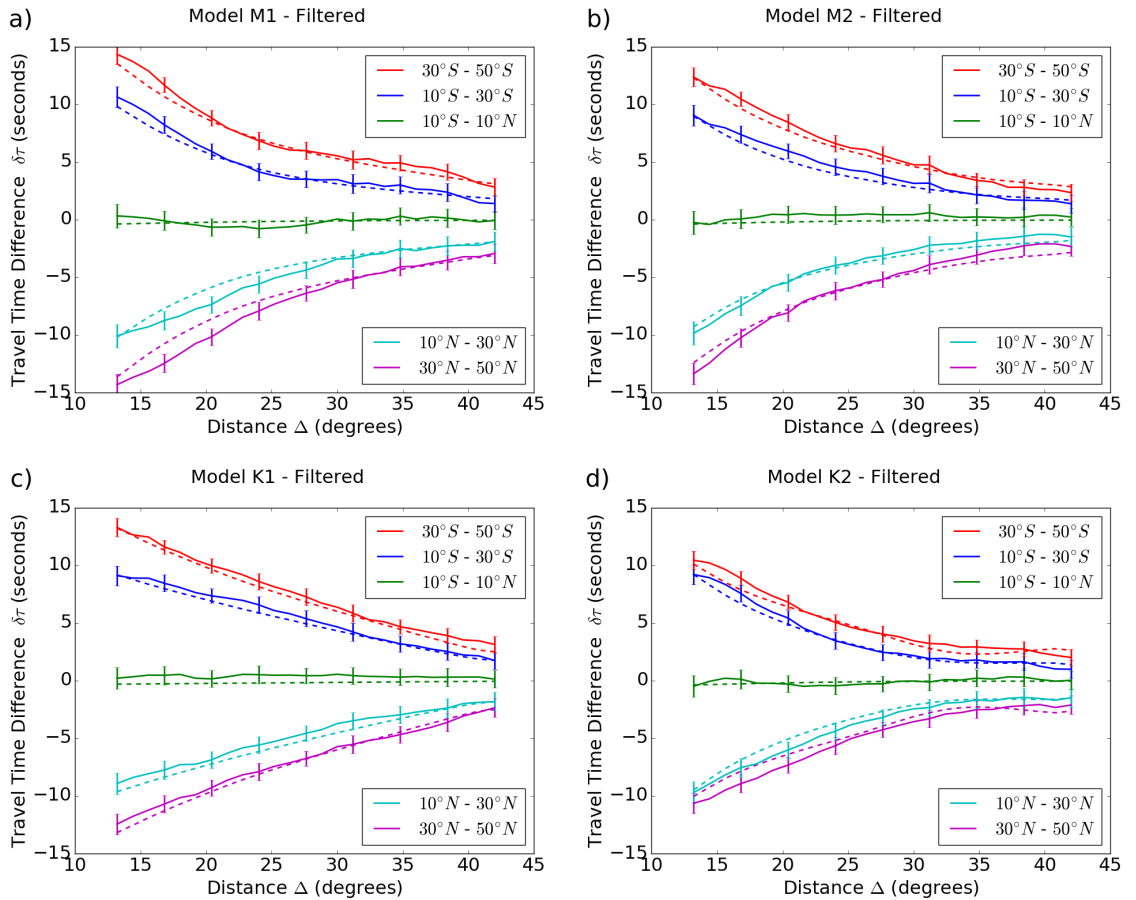


Figure 4.11 The N-S travel-time differences ($\delta\tau_{NS}$) as a function of travel distance (Δ) for models M1 (a), M2 (b), K1 (c), and K2 (d). The travel-time measurements are shown under the application of a Gaussian phase-speed filter ($\sigma = 0.05v_p$) for five latitudinal averages spanning $30^\circ\text{N} - 50^\circ\text{N}$, $10^\circ\text{N} - 30^\circ\text{N}$, $10^\circ\text{S} - 10^\circ\text{N}$, $10^\circ\text{S} - 30^\circ\text{S}$, $30^\circ\text{S} - 50^\circ\text{S}$. Dashed lines are theoretical times computed using the ray-path approximation (Equation (4.2)). Meridional circulation models are amplified by a factor of 36 (see Section 4.1).

Source: adapted from Stejko et al. (2021b).

of this noise profile. The SNR can be improved significantly—especially at larger travel-distances, by applying a phase-velocity filter to the data prior to deep focusing (see Section 4.3). The resulting travel-time differences can be seen in Figure 4.11.

A comparison of signals from the four models, shows noticeable variations between three of them. Moving from the deep single-cell profile (K1) to the shallow single-cell and weak-reversal double-cell profiles (M1 & M2), further onto the strong-reversal double-cell profile (K2), highlights a trend of increasing curvature, showing a more rapid decrease in travel-time differences with travel distance. These trends result in gaps wider than one standard deviation of the noise throughout a large part of the convective interior. The shallow single-cell and double-cell regimes (M1 and M2, respectively), however, fall within one standard deviation of the range of realization noise, even with the significant increase in the SNR through the application of a phase-velocity filter. These results have positive implications for the ability to distinguish between deep and shallow single-cell meridional circulation, as well as profiles of double-cell circulation with strong reversals. Unfortunately, the differences between shallow single- and double-cell profiles are much more subtle; using current helioseismology techniques, within the time-frame of HMI measurements (~ 10 years), any definitive statements on whether meridional circulation has one or two cells may be difficult to make.

In order to highlight systematic errors present in the model, as well as compare measurements to ray-path theory, computed travel-time differences of models with no background flows can be subtracted from the travel-time differences of the models with meridional circulation profiles that were excited with the same source (see Subsection 4.3.1). This results in realization noise being removed from travel-time differences in models M1, M2, K1, and K2, for the phase-speed filtered data-set (Figure 4.12)—revealing a close and consistent agreement to the ray-path approximation with the travel-time differences in the K1 model. As travel-time

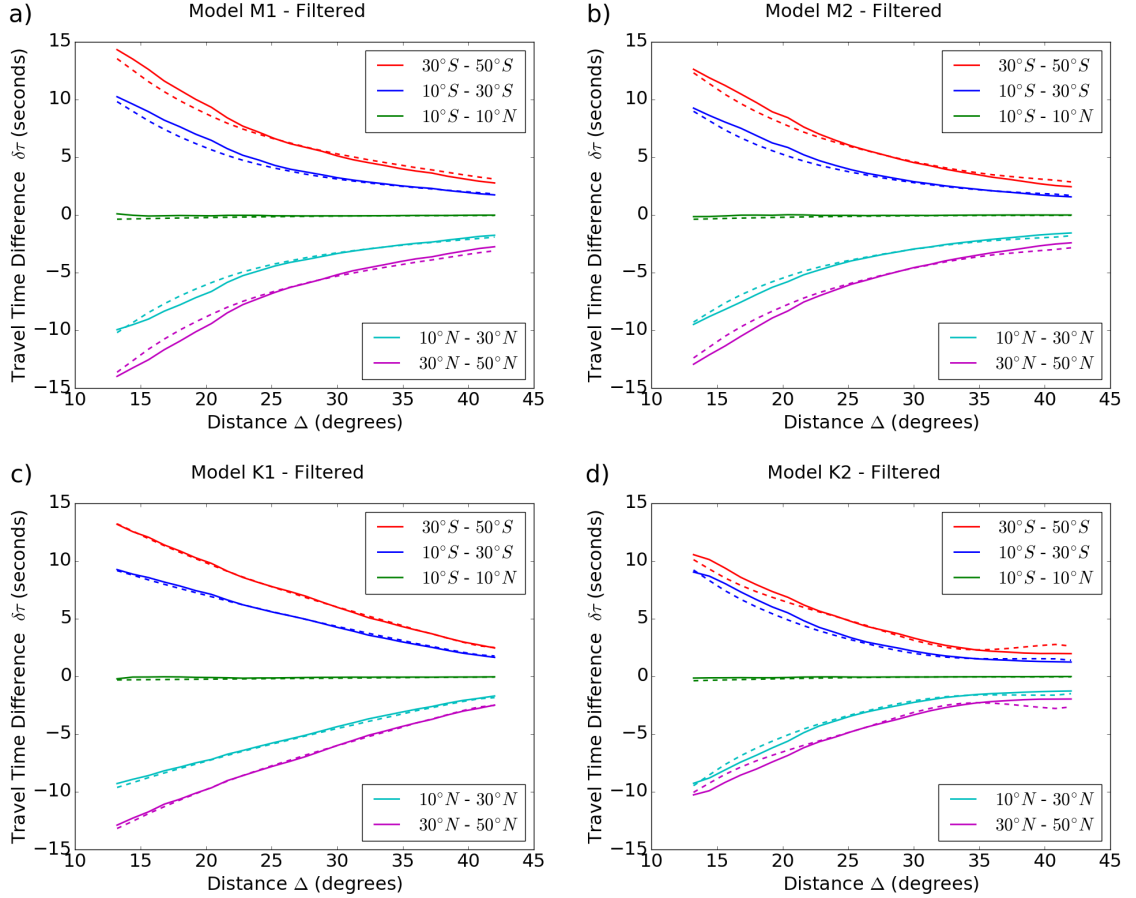


Figure 4.12 The N-S travel-time differences ($\delta\tau_{NS}$) as a function of travel distance (Δ) for models M1 (a), M2 (b), K1 (c), and K2 (d), under the application of Gaussian phase-speed filter ($\sigma = 0.05v_p$), with profiles of noise subtracted, showing five latitudinal averages spanning $30^\circ\text{N} - 50^\circ\text{N}$, $10^\circ\text{N} - 30^\circ\text{N}$, $10^\circ\text{S} - 10^\circ\text{N}$, $10^\circ\text{S} - 30^\circ\text{S}$, $30^\circ\text{S} - 50^\circ\text{S}$. Dashed lines are theoretical times computed using the ray-path approximation (Equation (4.2)). Meridional circulation models are amplified by a factor of 36 (see Section 4.1)

Source: adapted from Stejko et al. (2021b).

difference profiles begin to fall off more steeply with travel distance, however, the results begin to diverge slightly from the approximation, culminating in an inability to match the travel-time difference increase seen at large depths in model K2. Whether this is due to intrinsic systematic errors in the model or in the approximation itself deserves an in-depth investigation.

The profiles can also be compared to the publicly available data from the

analysis of Gizon et al. (2020) (Figure 4.13), scaling the travel-time differences computed using the ray-path approximation in models M1, M2, K1, and K2, to their travel-time measurements using MDI/GONG observations for Solar Cycle 24 (2008-2019). It is apparent that the level of noise is too large to draw significant conclusions distinguishing single- and double-cell regimes of meridional circulation.

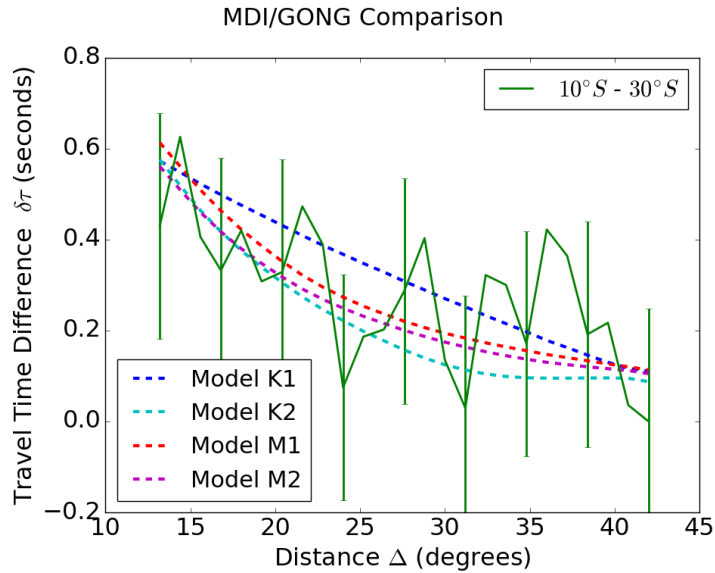


Figure 4.13 The N-S travel-time differences ($\delta\tau_{NS}$) as a function of travel distance (Δ) for MDI/GONG data published by Gizon et al. (2020). Latitude ranges in both hemispheres ($10^\circ\text{N} - 30^\circ\text{N}$, $10^\circ\text{S} - 30^\circ\text{S}$) are averaged in order to reduce noise and are compared to dashed lines representing latitudinal averages for models K1, K2, M1, and M2, as measured using the ray-path approximation (Equation (4.2)). Error bars are computed as the standard deviation (σ , Equation (4.3)) of the travel-time differences in the $10^\circ\text{N} - 10^\circ\text{S}$ latitude range from zero.

Source: adapted from Stejko et al. (2021b).

CHAPTER 5

DISCUSSION

5.1 Global Solar Modeling

The work presented in this dissertation focuses on the current state of global solar modeling. 3D simulations have become an indispensable part of the field of heliophysics and as the power of computing hardware and software continues to grow, these models will continue to open up new avenues of investigation. The study of solar and stellar environments is fundamentally a theoretical exercise, as their inhospitable environment may forever preclude direct observation. While the chaotic nature of solar dynamics does not lend itself well to simple theoretical explanations, it is exactly these types of situations where the promise of computational algorithms can be seen. The better that simple principles of physics can be prescribed, the more accurate and insightful the aggregate of computational solutions will be. Models of solar and stellar evolution will become the key to unlocking a deep and fundamental understanding of the nature of solar structure and pave the way for accurate predictive models of space weather.

Global MHD modeling has been instrumental in unlocking questions on the evolution of the solar dynamo. Simple operational dynamo models (Parker, 1955; Moffatt, 1978; Babcock, 1961; Leighton, 1969) build the foundation for mean-field theory (Brandenburg & Subramanian, 2005) to create a framework for the evolution of the solar cycle. Convectively-driven MHD models take the opposite approach, attempting to reproduce solar observations as a natural byproduct of an evolving system, and gain insight into the structure of turbulent coefficients in a holistic way. When these two approaches meet, they will signify a validation of our understanding of the nature of solar structure and the parameters that drive the system. Unfortunately,

global MHD modeling (Brun et al., 2004; Ghizaru et al., 2010; Racine et al., 2011; Cossette et al., 2013; Nelson et al., 2013; Augustson et al., 2015; Guerrero et al., 2016; Cossette et al., 2017; Warnecke, 2018; Guerrero et al., 2019) still has a long way to go before fully replicating solar observations in a satisfactory way. An important insight that these models have begun to show, however, is that they may have been taking a too narrow view of the system. The complex interaction of the internal dynamo structure with the solar surface presents an obstacle for the anelastic models that cannot simulate compressive interactions and are not built for the high plasma flow speeds in subsurface layers. It seems that the next step will rely on novel systems, purpose-built to simulate these interactions. A completely new non-linear compressible MHD model is a massive undertaking; in order to move the needle on this topic slightly forward, this dissertation presents the formulation of a new linearized compressible solar model. The pseudo-spectral computational techniques presented, are formulated in a way that can be extended to a non-linear model in the future. In the mean-time, there is no shortage of uses for a new generation of fast and efficient acoustic models, especially in the context of interpreting inferences of helioseismic observations of the Sun.

5.2 The GALE Code

The GALE code can be used facilitate the testing and validation of local and global helioseismology techniques in diverse regimes of three-dimensional flows. While helioseismology has been an indispensable tool in exploring interior dynamics on the Sun, it can have trouble resolving exact profiles of flow, especially at greater depths. Forward-modeling offers the opportunity to test the impact of subtle differences generated by a variety of theoretical models of mean mass flows, forming a basis to better interpret observational oscillation data.

This model is validated for two distinct profiles: differential rotation and meridional circulation. These two regimes are critical for understanding and simulating the distribution of angular momentum and magnetic flux that governs the solar magnetic cycle. The pseudo-spectral techniques presented here will be necessary components for future models to efficiently compute spherical harmonic resolutions of $l_{max} > 300$, previously considered to be too computationally expensive. These resolutions will be necessary to model local helioseismology techniques on sound speed perturbations due to small-scale structures on the solar surface, creating a link to linear effects of global perturbations.

In this dissertation, the GALE code is employed in an attempt to tackle unanswered questions on the nature of meridional circulation. Large variations in inferences have been made using similar local helioseismology techniques—from a double-cell meridional circulation profile seen in HMI observations (Zhao et al., 2013; Chen, 2019) to recent reassertions of a single cell profile from MDI/GONG data (Gizon et al., 2020). The feasibility of the two regimes has been explored in recent years, with convectively driven MHD and HD models reproducing the necessary environment for both.

The actual differences may lie somewhere in between the large variations inferred in the two regimes. This model attempts to test the feasibility of discerning between meridional profiles with a deep and shallow single-cell as well as strong and weak secondary-cell profiles, generated by the same mean-field model, operating with minimal parameter changes (K1 & K2 in Pipin & Kosovichev (2018)—referred to as M2 and M3 in their paper; M1 & M2 in Pipin & Kosovichev (2019)). Using the GALE code to simulate the stochastic excitation of acoustic modes throughout the convective interior, the deep focusing method can measure the resulting realization noise in travel-time differences. Noise is one of the main obstacles when inferring structures from observations. Even if the systematic CtoL effect can be fully resolved,

the time-frame of measurements remains a limiting factor. The high levels of noise in these measurements leave large uncertainties that may be the source of the divergent conclusions made on the nature of meridional circulation. Physics-based models can be used to constrain results in the context of a broader complex system. The GALE code is used to analyze differences between a shallow single-cell and a weak-reversal double-cell regime, generated by a mean-field simulation that uses a physics-based model of gyroscopic pumping to induce the reverse-flow cell near the base of the tachocline. These models show that even with the formation of a reverse flow, the travel-time differences may fall well within one standard deviation of error for both phase-speed filtered and unfiltered deep-focusing measurements. These profiles (M1 & M2) provide the low end of the baseline for variance between the two regimes. An examination of physics-based profiles that may be more consistent with single-cell (Gizon et al., 2020) inferences such as K1 or double-cell (Zhao et al., 2013; Chen, 2019) inferences such as K2, can also be useful. The deep single-cell profile (K1) and strong-reversal double-cell profile (K2) show large enough differences that a distinction with a relatively high degree of confidence is feasible. For now, however, the best way to constrain these solutions is by looking at the broader impacts of these profiles within the context of their effects on global solar dynamics (see Kitchatinov, 2013). Pipin & Kosovichev (2018) show that an unavoidable effect of increasing the strength of the return flow is a profile of differential rotation that is inconsistent with inferences of global helioseismology (Howe et al., 2011). While mean-field modeling does not fully capture the structure of the solar interior, a consistency with a theoretical understanding of the system can lend confidence to inferred results. While meaningful conclusions on the nature of the return flow are within the reach of local helioseismology techniques, currently, mean-field model-based profiles of meridional circulation show that any definitive statements on the prevalence of either a single- or double-cell regime should be taken with a grain of salt.

5.3 Future Plans

This section describes the future applications of the GALE code, including an extension that solves for the perturbations of a background magnetic field in the ideal MHD limit (Subsection 5.3.1), as well as the formulation of a non-linear algorithm based on the computational methods described in this dissertation (Subsection 5.3.2).

5.3.1 Magnetic field extension

Future iterations of the GALE code will include a linear perturbative magnetic field term, allowing helioseismic techniques to explore large global magnetic structures, as well as magnetic flux from emerging active regions on the solar surface. The effect of a background magnetic field on the conservation of momentum (Equation (3.2)) can be easily modeled by the action of the Lorentz force, which, with the aid of Ampere's law, vector identities, and the divergence-free field condition ($\nabla \cdot \mathbf{B} = 0$), can be written in the following conservative form.

$$\mathbf{F}_L = \frac{\mathbf{J} \times \mathbf{B}}{c} = -\nabla \left(\frac{B^2}{8\pi} \right) + \nabla \cdot \frac{\mathbf{B}\mathbf{B}}{4\pi}, \quad (5.1)$$

where the first term on the RHS of Equation (5.1) is the magnetic pressure and the second term is a magnetic hoop stress. The Lorentz Force (\mathbf{F}_L) can be linearized by splitting the magnetic field into a base field ($\tilde{\mathbf{B}}$) and a perturbation (\mathbf{B}'), keeping only the linear perturbation terms.

$$\mathbf{F}'_L = -\nabla \left(\frac{\tilde{\mathbf{B}} \cdot \mathbf{B}'}{8\pi} \right) + \nabla \cdot \frac{\mathbf{B}'_{ij}}{4\pi}, \quad (5.2)$$

The perturbation of the magnetic dyad is written as $\mathbf{B}'_{ij} = \tilde{\mathbf{B}}\mathbf{B}' + \mathbf{B}'\tilde{\mathbf{B}}$. The linearized Lorentz force can be added to the conservation of momentum (Equation (3.2)); writing the new relation alongside the linearized induction equation in the ideal MHD limit

(where conductivity is infinite), results in the extended linearized MHD governing equations:

$$\frac{\partial \Upsilon'}{\partial t} + \nabla : (\mathbf{m}'\tilde{\mathbf{u}} + \tilde{\rho}\tilde{\mathbf{u}}\mathbf{u}') = -\nabla^2 \left(p' + \frac{\tilde{\mathbf{B}} \cdot \mathbf{B}'}{8\pi} \right) - \nabla \cdot (\rho' \tilde{g}_r \hat{\mathbf{r}}) + R'_\Upsilon + \nabla : \frac{\mathcal{B}'_{ij}}{4\pi}, \quad (5.3)$$

$$\frac{\partial \mathbf{B}'}{\partial t} = \nabla \times (\mathbf{u}' \times \tilde{\mathbf{B}} + \tilde{\mathbf{u}} \times \mathbf{B}'). \quad (5.4)$$

The governing equation for the induction of the magnetic field (Equation (5.4)) can be solved in spherical coordinates, by computing the cross product of the velocity and the magnetic field ($\mathbf{u}' \times \tilde{\mathbf{B}} + \tilde{\mathbf{u}} \times \mathbf{B}'$) in real space. Taking the spherical harmonic decomposition of the resulting cross product coefficients will allow for a coordinate transformation into the VSH basis, using Equations (A.12), (A.13). The curl can then be computed with the technique defined in Appendix A, Section A.5. The induction equation can be discretized in time using the backward Euler method to maintain the stability of the solution. The resulting magnetic field term can now be used to solve for the Lorentz force contributions in the MHD extension of the conservation of momentum (Equation (5.3)). Computing the magnetic pressure is relatively easy to do in real space. The divergence of the linearized hoop stress ($\nabla : \mathcal{B}'_{ij}/4\pi$) can also be efficiently solved using the pseudo-spectral technique for the computation of the material derivative described in Subsection 3.6.5.

This algorithm presents the opportunity to test and simulate helioseismology techniques employed in the detection of magnetic structures. While linear acoustic simulations with magnetic fields already exist (Cameron et al., 2008; Khomenko et al., 2009; Parchevsky & Kosovichev, 2009; Felipe et al., 2016), they are exclusively relegated to small domains at the solar surface. A fast and efficient fully global linear MHD algorithm can open up many new avenues of investigation. Helioseismology is currently the only tool that can truly probe the solar interior directly, however,

the resulting structural inferences are only as good as the understanding of the technique’s limitations. Global linear MHD models offer the opportunity for an in-depth analysis of how large global magnetic fields can affect travel-time signatures at varying depths and magnetic field strengths, presenting a detailed picture of what can be expected when probing the solar interior. Such analyses can offer new insight into the opportunities and limits of what current techniques in helioseismology can achieve when attempting to detect global magnetic structures.

Global linear MHD models also offer an unprecedented chance to create a link between large global flows and the emergence of relatively small-scale active regions. A deeper understanding of the interconnected nature of these systems is fundamentally necessary in order to fully grasp how magnetic structures are created, stored, and then emerge onto the solar surface. More importantly, mapping the action of global and local subsurface flows can aid in building predictive models to more accurately gauge the potential strengths and locations of energetic events on the solar surface.

5.3.2 Non-linear algorithm

The computational structure of the GALE code, as well as its method of parallelization (Subsection 3.6.8), will become the foundation for the development of a fully non-linear global MHD algorithm. The formulation of this algorithm must include the solenoidal portion of the momentum field that was previously discarded. This field is mainly solved with force contributions from baroclinicity and the Coriolis force and the majority of its effects will be felt on vastly different scales than the potential flow field. Using the split-field formulation defined in Subsection 3.2.2, allows for the ability to control the resolution of the two fields independently, concentrating computing power where it is most needed.

The solenoidal field is defined as some vector potential ($\mathbf{m}_s = \nabla \times \Psi$) under the divergence-free field condition ($\nabla \cdot \mathbf{m}_s = 0$). These conditions are ensured

by solving for the curl of the conservation of momentum, Equation (3.7), where $\nabla \times \rho \mathbf{u} = \nabla \times \mathbf{m} = \nabla^2 \Psi = \boldsymbol{\varpi}$. \mathcal{M} is defined as the aggregate of all internal and external forces.

$$\frac{\partial \boldsymbol{\varpi}'}{\partial t} = \nabla \times \mathcal{M} . \quad (5.5)$$

The governing equation for the curl of the momentum field (Equation (5.5)) can be broken down into the orthogonal set of coefficients spanning the VSH basis (Section A.1).

$$\frac{\partial \varpi^r}{\partial t} = [\nabla \times \mathcal{M}]^r , \quad \frac{\partial \varpi^{(1)}}{\partial t} = [\nabla \times \mathcal{M}]^{(1)} , \quad \frac{\partial \varpi^{(2)}}{\partial t} = [\nabla \times \mathcal{M}]^{(2)} .$$

Using the definition for a curl in the VSH basis (Section A.5), it is immediately obvious that the relations for the first two coordinates (ϖ^r , $\varpi^{(1)}$) are degenerate solutions for the $m^{(2)}$ momentum field, while the last relation solves for $\varpi^{(2)}$ as a function of $\mathcal{M}^{(1)}$ and \mathcal{M}^r .

$$\begin{aligned} \frac{\partial m^{(2)}}{\partial t} &= \mathcal{M}^{(2)} , \\ \frac{\partial \varpi^{(2)}}{\partial t} &= \frac{1}{r} \frac{\partial}{\partial r} (r \mathcal{M}^{(1)}) - \frac{\mathcal{M}^r}{r} . \end{aligned}$$

This new governing equation for $\varpi^{(2)}$ can be used to solve for the orthogonal coefficients of the momentum field (m^r , $m^{(1)}$), using the definition of a curl in the VSH basis (Section A.5) and the divergence-free condition for the solenoidal momentum field ($\nabla \cdot \rho \mathbf{u} = 0$, Section A.4).

$$\varpi^{(2)} = \frac{1}{r} \frac{\partial}{\partial r} (r m^{(1)}) - \frac{m^r}{r} ,$$

$$\frac{1}{r^2} \frac{\partial}{\partial r} (r^2 m^r) - \frac{l(l+1)}{r} m^{(1)} = 0 .$$

Rearranging terms leaves the following two equalities needed to solve for the full solenoidal momentum field.

$$\frac{\partial^2}{\partial r^2} (r^2 m^r) - l(l+1) m^r = l(l+1) r \varpi^{(2)} , \quad (5.6)$$

$$r m^{(1)} = \frac{1}{l(l+1)} \frac{\partial}{\partial r} (r^2 m^r) . \quad (5.7)$$

An implicit numerical Helmholtz solver, formulated in a similar manner to the Poisson solver presented in Subsection 3.6.4, can be used to compute the radial part of solenoidal field (m^r , Equation (5.6)), while a simple radial finite-difference method can be used to compute $m^{(1)}$ (Equation (5.7)).

Gibb's relation ($T(Ds/Dt) = De/Dt + p(DV/Dt)$) lets the conservation of energy be expressed as an entropy relation in its conservative form, where \mathcal{Q} is the aggregate of heat conduction, radiation, viscous friction, and Ohmic heating. Using the formulation described in this section, the full set of governing equations for a non-linear global compressible MHD model can be written as:

$$\frac{\partial \rho}{\partial t} + \Upsilon = 0 , \quad (5.8)$$

$$\frac{\partial \Upsilon}{\partial t} + \nabla : (\rho \mathbf{u} \mathbf{u}) = -\nabla^2 \left(p + \frac{B^2}{8\pi} \right) + \nabla \cdot \mathcal{M} + \nabla : \frac{\mathbf{B} \mathbf{B}}{4\pi} , \quad (5.9)$$

$$\frac{\partial m^{(2)}}{\partial t} + [\nabla \cdot (\rho \mathbf{u} \mathbf{u})]^{(2)} = \mathcal{M}^{(2)} + \left[\nabla \cdot \frac{\mathbf{B} \mathbf{B}}{4\pi} \right]^{(2)} , \quad (5.10)$$

$$\begin{aligned} \frac{\partial \varpi^{(2)}}{\partial t} + \frac{1}{r} \frac{\partial}{\partial r} \left(r [\nabla \cdot (\rho \mathbf{u} \mathbf{u})]^{(1)} \right) - \frac{1}{r} [\nabla \cdot (\rho \mathbf{u} \mathbf{u})]^{(r)} &= \frac{1}{r} \frac{\partial}{\partial r} (r \mathcal{M}^{(1)}) - \frac{\mathcal{M}^r}{r} \\ &+ \frac{1}{r} \frac{\partial}{\partial r} \left(r \left[\nabla \cdot \frac{\mathbf{B} \mathbf{B}}{4\pi} \right]^{(1)} \right) - \frac{1}{r} \left[\nabla \cdot \frac{\mathbf{B} \mathbf{B}}{4\pi} \right]^r , \end{aligned} \quad (5.11)$$

$$\frac{\partial \rho s}{\partial t} + \nabla \cdot (\rho \mathbf{u} s) = \mathcal{Q} , \quad (5.12)$$

$$\frac{\partial \mathbf{B}}{\partial t} = \nabla \times (\mathbf{u} \times \mathbf{B}) - \frac{c^2}{4\pi\sigma} \nabla \times (\nabla \times \mathbf{B}) . \quad (5.13)$$

In these governing equations, \mathcal{M} is the aggregate of gravitational effects, pseudo-forces in a rotating reference frame, and the divergence of the viscous stress tensor ($\nabla \cdot \boldsymbol{\tau}_{ij}$). The conservation of the full momentum field is defined by the potential flow (Equation (5.9)), where $\Upsilon = \nabla \cdot \rho \mathbf{u}$, as well as the two components of the solenoidal field (Equations (5.10), (5.11)) in the VSH basis. These relations include the magnetic effects of the Lorentz force in its conservative form (see Subsection 5.3.1). This allows for the hoop stress, along with the material derivative, and the viscous stress tensor (in a gas with no angular momentum), to be defined as second-rank symmetric tensors, which can be decomposed into the TSH basis described in Appendix A, Section A.2. The divergence can be computed using the simple set of 1D radial PDE's in the pseudo-spectral method employed in the GALE code (Subsection 3.6.5), solving for components in the VSH basis directly. Induction of the magnetic field (Equation (5.13)) includes effects of plasma resistivity, where σ is the conductivity, and is solved in the manner described in Subsection 5.3.1. Pressure can be computed from entropy and density ($p(\rho, s)$), using ideal gas relations or equations of state for solar plasma.

The techniques tested and validated in this dissertation are all extendable to the operation of the non-linear code. The simple and efficient pseudo-spectral method used to compute the material derivative in the linearized GALE code (Subsection 3.6.5) can be used to solve for the other external force contributions, when expressed in their conservative form. This allows for the conservation of momentum equations to be solved entirely in frequency space—including the considerations of the viscous stress tensor, which can be used to model SGS turbulence in the LES approach (Germano et al., 1991). This culminates in a new and efficient method for

the numerical computation of the Navier-Stokes equations and can serve as a stepping stone for a new generation of global MHD solar and stellar models.

The promise of a new set of compressible global MHD models is an alluring one. The details of the mechanisms that connect the global toroidal magnetic field at the base of the tachocline to the poloidal field emerging on the solar surface remains one of the fundamental mysteries in solar physics. Fully compressible global model have the potential to simulate the complex interplay of turbulent transport coefficients in the overshoot layer underneath the tachocline, as well as addressing the complex role that near-surface shear plays in shaping the structure of the butterfly diagram. These simulations offer an unprecedented opportunity to link the evolution of the global dynamo to internal flow structures, such as differential rotation, meridional circulation, and convection. Understanding the influence of global flows on specific dynamo patterns will lead to much more robust models of the extended solar cycle, as well as be useful in putting a constraint on the wide range of inferences made using helioseismology. An efficient compressible algorithm will also set the ground work for global solar MHD models that can be extended beyond the solar atmosphere and into the corona, developing a full interconnected picture of how global magnetic structures develop, evolve, and emerge onto the solar surface to form highly energetic active regions.

APPENDIX A

VECTOR/TENSOR SPHERICAL HARMONICS

This appendix contains the description and derivation of the vector and tensor spherical harmonic coordinate bases employed in the pseudo-spectral computation of the GALE code.

A.1 Vector Spherical Harmonics

The VSH basis is defined by extending the scalar spherical harmonic (Y_{lm}) to a 3D vector field, described by the following linearly independent basis.

$$\mathbf{Y}_{lm} = Y_{lm} \hat{\mathbf{r}} , \tag{A.1}$$

$$\mathbf{\Psi}_{lm} = r \nabla Y_{lm} , \tag{A.2}$$

$$\mathbf{\Phi}_{lm} = \vec{\mathbf{r}} \times \nabla Y_{lm} , \tag{A.3}$$

where $\hat{\mathbf{r}}$ is the unit radial vector in spherical coordinates, $\vec{\mathbf{r}}$ is the radial position vector, and Y_{lm} is the spherical harmonic function, written in the Condon-Shortley convention as:

$$Y_{lm} = (-1)^m \sqrt{\frac{(2l+1)(l-m)!}{4\pi(l+m)!}} P_l^m(\cos\theta) e^{im\phi} . \tag{A.4}$$

The VSH unit vectors (Equations (A.1)-(A.3)) can also be described as a function of the scalar spherical harmonic (Equation (A.4)) in spherical coordinates.

$$\mathbf{Y}_{\mathbf{l}\mathbf{m}} = Y_{lm} \hat{\mathbf{r}} \quad (\text{A.5})$$

$$\mathbf{\Psi}_{\mathbf{l}\mathbf{m}} = \frac{\partial Y_{lm}}{\partial \theta} \hat{\boldsymbol{\theta}} + \frac{1}{\sin \theta} \frac{\partial Y_{lm}}{\partial \phi} \hat{\boldsymbol{\phi}} \quad (\text{A.6})$$

$$\mathbf{\Phi}_{\mathbf{l}\mathbf{m}} = -\frac{1}{\sin \theta} \frac{\partial Y_{lm}}{\partial \phi} \hat{\boldsymbol{\theta}} + \frac{\partial Y_{lm}}{\partial \theta} \hat{\boldsymbol{\phi}} \quad (\text{A.7})$$

An arbitrary 3D vector field (\mathbf{v}) can be expanded into the following components of the VSH basis.

$$\mathbf{v} = \sum_{m=-lmax}^{lmax} \sum_{l=|m|}^{lmax} \left(v_{lm}^r(r) \mathbf{Y}_{\mathbf{l}\mathbf{m}} + v_{lm}^{(1)}(r) \mathbf{\Psi}_{\mathbf{l}\mathbf{m}} + v_{lm}^{(2)}(r) \mathbf{\Phi}_{\mathbf{l}\mathbf{m}} \right) \quad (\text{A.8})$$

The superscript “ r ” (v^r) denotes the radial component of the vector field, while superscripts “(1)” ($v^{(1)}$) and “(2)” ($v^{(2)}$) represent components tangent to the surface of the two-sphere.

In order to ease the difficulty of working with vector spherical harmonics, the following set of real-space scalar VSH components defined by Novak et al. (2010), recast the VSH basis into Equations (A.9)-(A.11).

$$v^r = \sum_{m=-lmax}^{lmax} \sum_{l=|m|}^{lmax} v_{lm}^r(r) Y_{lm} , \quad (\text{A.9})$$

$$v^\eta = \sum_{m=-lmax}^{lmax} \sum_{l=|m|}^{lmax} v_{lm}^{(1)}(r) Y_{lm} , \quad (\text{A.10})$$

$$v^\mu = \sum_{m=-lmax}^{lmax} \sum_{l=|m|}^{lmax} v_{lm}^{(2)}(r) Y_{lm} . \quad (\text{A.11})$$

These components define a set of orthogonal VSH coefficients onto scalar spherical harmonic space (Y_{lm}), resulting in easy to use real-space components that lend themselves well to performing vector operations using recursion relations, such as the divergence ($\nabla \cdot$) and the Laplacian (∇^2). The transverse scalar VSH components

(Equations (A.10),(A.11)) can be defined in terms of spherical coordinates by plugging them into the definition for the VSH basis (Equations (A.6),(A.7)).

$$v^\theta = \frac{\partial v^\eta}{\partial \theta} - \frac{1}{\sin \theta} \frac{\partial v^\mu}{\partial \phi} , \quad (\text{A.12})$$

$$v^\phi = \frac{\partial v^\mu}{\partial \theta} + \frac{1}{\sin \theta} \frac{\partial v^\eta}{\partial \phi} . \quad (\text{A.13})$$

The scalar VSH basis can also be defined as a function of spherical coordinates by taking the transverse Laplacian ($\nabla_{\theta\phi}^2$) of the scalar VSH components and substituting in the spherical coordinate definitions above (Equations (A.12),(A.13)).

$$\nabla_{\theta\phi}^2 v^\eta = \frac{1}{\sin \theta} \frac{\partial}{\partial \theta} (\sin \theta v^\theta) + \frac{1}{\sin \theta} \frac{\partial v^\phi}{\partial \phi} , \quad (\text{A.14})$$

$$\nabla_{\theta\phi}^2 v^\mu = \frac{1}{\sin \theta} \frac{\partial}{\partial \theta} (\sin \theta v^\phi) - \frac{1}{\sin \theta} \frac{\partial v^\theta}{\partial \phi} , \quad (\text{A.15})$$

where the transverse Laplacian ($\nabla_{\theta\phi}^2$) for some function f , is defined as:

$$\nabla_{\theta\phi}^2 f = \frac{1}{\sin \theta} \frac{\partial}{\partial \theta} \left(\sin \theta \frac{\partial f}{\partial \theta} \right) + \frac{1}{\sin^2 \theta} \frac{\partial^2 f}{\partial \phi^2} . \quad (\text{A.16})$$

A.2 Tensor Spherical Harmonics

The following section contains extensive use of tensor notation, the unit vectors of which ($\hat{\mathbf{e}}_r, \hat{\mathbf{e}}_\theta, \hat{\mathbf{e}}_\phi$) can be explicitly defined as the covariant orthonormal natural basis in spherical coordinates.

$$\hat{\mathbf{e}}_r = \frac{\partial}{\partial r} , \quad \hat{\mathbf{e}}_\theta = \frac{1}{r} \frac{\partial}{\partial \theta} , \quad \hat{\mathbf{e}}_\phi = \frac{1}{r \sin \theta} \frac{\partial}{\partial \phi} . \quad (\text{A.17})$$

In this basis, the contravariant tensor components of some arbitrary tensor (\mathbf{T}) are:

$$\mathbf{T} = \sum_{i=r,\theta,\phi} \sum_{j=r,\theta,\phi} T^{ij} \hat{\mathbf{e}}_i \otimes \hat{\mathbf{e}}_j . \quad (\text{A.18})$$

The definition of the tensor spherical harmonic basis follows the general formulation and notation initially defined by Mathews (1962), and expanded on by Zerilli (1970) and Thorne (1980). An orthonormal basis for the rank two tensor, can be initially defined in the manner of Mathews (1962), by deriving a set of unit tensors (t_m) from the second-order spherical harmonic ($Y_{l=2,m}(\Omega)$), expressed in cartesian vectors ($\hat{\mathbf{x}}, \hat{\mathbf{y}}, \hat{\mathbf{z}}$) as:

$$\begin{aligned} \mathbf{t}_{\pm 2} &= \frac{1}{2} (\hat{\mathbf{x}}\hat{\mathbf{x}} - \hat{\mathbf{y}}\hat{\mathbf{y}}) \pm \frac{i}{2} (\hat{\mathbf{x}}\hat{\mathbf{y}} + \hat{\mathbf{y}}\hat{\mathbf{x}}) , \\ \mathbf{t}_{\pm 1} &= \mp \frac{1}{2} (\hat{\mathbf{x}}\hat{\mathbf{z}} + \hat{\mathbf{z}}\hat{\mathbf{x}}) - \frac{i}{2} (\hat{\mathbf{y}}\hat{\mathbf{z}} + \hat{\mathbf{z}}\hat{\mathbf{y}}) , \\ \mathbf{t}_0 &= \sqrt{\frac{1}{6}} (2\hat{\mathbf{z}}\hat{\mathbf{z}} - \hat{\mathbf{x}}\hat{\mathbf{x}} - \hat{\mathbf{y}}\hat{\mathbf{y}}) . \end{aligned}$$

This basis corresponds to the irreducible representation of the rotation group of order two in $\text{SO}(3)$ ($\mathcal{D}^{(2)}$ where $\mathbf{t} = \mathcal{D}^{(0)} + \mathcal{D}^{(1)} + \mathcal{D}^{(2)}$), which forms the complete basis for a traceless symmetric tensor. The other two irreducible parts of this rotation group consist of the order one ($\mathcal{D}^{(1)}$) and order zero ($\mathcal{D}^{(0)}$), which correspond to the antisymmetric part of a tensor and trace of a tensor respectively. Only symmetric tensors are used in this formulation, so the antisymmetric part can be discarded. Including the trace completes the definition of the symmetric tensor basis.

$$\sqrt{\frac{1}{3}}\delta = \sqrt{\frac{1}{3}} (\hat{\mathbf{x}}\hat{\mathbf{x}} + \hat{\mathbf{y}}\hat{\mathbf{y}} + \hat{\mathbf{z}}\hat{\mathbf{z}}) ,$$

where $\sqrt{1/3}$ is a normalization factor. These unit tensors can be coupled to the scalar spherical harmonic to complete the definition for a linearly independent spherical harmonic tensor basis (Equations (A.19)).

$$\begin{aligned}
\mathbf{T}_{\mathbf{lm}}^{(0)1} &= -\frac{\delta Y_{lm}}{\sqrt{3}} , \\
\mathbf{T}_{\mathbf{lm}}^{(2)1} &= \sum_{\mu} \langle l, m - \mu, 2, \mu | lm \rangle Y_{l, m - \mu} \mathbf{t}_{\mu} , \\
\mathbf{T}_{\mathbf{lm}}^{(2)1+1} &= \sum_{\mu} \langle l + 1, m - \mu, 2, \mu | lm \rangle Y_{l+1, m - \mu} \mathbf{t}_{\mu} , \\
\mathbf{T}_{\mathbf{lm}}^{(2)1+2} &= \sum_{\mu} \langle l + 2, m - \mu, 2, \mu | lm \rangle Y_{l+2, m - \mu} \mathbf{t}_{\mu} , \\
\mathbf{T}_{\mathbf{lm}}^{(2)1-1} &= \sum_{\mu} \langle l - 1, m - \mu, 2, \mu | lm \rangle Y_{l-1, m - \mu} \mathbf{t}_{\mu} , \\
\mathbf{T}_{\mathbf{lm}}^{(2)1-2} &= \sum_{\mu} \langle l - 2, m - \mu, 2, \mu | lm \rangle Y_{l-2, m - \mu} \mathbf{t}_{\mu} .
\end{aligned} \tag{A.19}$$

This orthonormal basis for tensor spherical harmonics can be conceptualized in a similar way to a scalar spherical harmonic with an additional “spin” of two, creating five linearly independent spherical harmonic terms of the same degree and azimuthal order (l, m) , covering the full basis of a symmetric traceless tensor. This basis, however, is not the optimal form for performing vector and tensor operations in this formulation. For a simple linearly independent basis with useful orthogonality relationships, these unit tensors (Equations (A.19)) can be rearranged into the TSH basis outlined and defined by Zerilli (1970), consisting of the following vector dyad operations on the scalar spherical harmonic.

$$\begin{aligned}
\nabla \nabla Y_{lm} , \quad \mathbf{L} \nabla Y_{lm} , \quad \mathbf{L} \mathbf{L} Y_{lm} , \\
\hat{\mathbf{r}} \nabla Y_{lm} , \quad \hat{\mathbf{r}} \mathbf{L} Y_{lm} , \quad \hat{\mathbf{r}} \hat{\mathbf{r}} Y_{lm} .
\end{aligned} \tag{A.20}$$

$\nabla \nabla$ is the gradient dyad and $\mathbf{L} \mathbf{L}$ is the angular momentum operator dyad, where $\mathbf{L} = -i(\hat{\mathbf{r}} \times \nabla)$. Zerilli (1970) expands these operations explicitly (Equations (A.20)), keeping only the terms corresponding to the tensor spherical harmonic basis for a symmetric tensor with a trace (Equations (A.19)):

$$\begin{aligned}
[\nabla\nabla Y_{lm}]_s &= \frac{1}{r^2} l(l+2) \sqrt{\frac{(l+1)(l+2)}{(2l+1)(2l+3)}} \mathbf{T}_{\mathbf{lm}}^{(2)1+2} + \frac{1}{r^2} l(l+1) \sqrt{\frac{2l(l+1)}{3(2l-1)(2l+3)}} \mathbf{T}_{\mathbf{lm}}^{(2)1} \\
&\quad + \frac{(l+1)(l-1)}{r^2} \sqrt{\frac{l(l-1)}{(2l+1)(2l-1)}} \mathbf{T}_{\mathbf{lm}}^{(2)1-2} + \frac{l(l+1)}{r^2 \sqrt{3}} \mathbf{T}_{\mathbf{lm}}^{(0)1} , \\
[\mathbf{L}\nabla Y_{lm}]_s &= -\frac{1}{r} l \sqrt{\frac{l(l+1)(l+2)}{2(2l+1)}} \mathbf{T}_{\mathbf{lm}}^{(2)1+1} - \frac{1}{r} (l+1) \sqrt{\frac{l(l+1)(l-1)}{2(2l+1)}} \mathbf{T}_{\mathbf{lm}}^{(2)1-1} , \\
[\mathbf{L}\mathbf{L}Y_{lm}]_s &= \sqrt{\frac{l(l+1)(2l-1)(2l+3)}{6}} \mathbf{T}_{\mathbf{lm}}^{(2)1} - \frac{l(l+1)}{\sqrt{3}} \mathbf{T}_{\mathbf{lm}}^{(0)1} , \\
[\hat{\mathbf{r}}\nabla Y_{lm}]_s &= \frac{1}{r} \sqrt{l(l+1)} \left[-\sqrt{\frac{l(l+2)}{(2l+1)(2l+3)}} \mathbf{T}_{\mathbf{lm}}^{(2)1+2} - \frac{3}{\sqrt{6(2l-1)(2l+3)}} \mathbf{T}_{\mathbf{lm}}^{(2)1} \right. \\
&\quad \left. + \sqrt{\frac{(l+1)(l-1)}{(2l-1)(2l+1)}} \mathbf{T}_{\mathbf{lm}}^{(2)1-2} \right] , \\
[\hat{\mathbf{r}}\mathbf{L}Y_{lm}]_s &= \sqrt{\frac{l(l+1)}{2}} \left[\sqrt{\frac{(l+2)}{(2l+1)}} \mathbf{T}_{\mathbf{lm}}^{(2)1+1} - \sqrt{\frac{(l-1)}{(2l+1)}} \mathbf{T}_{\mathbf{lm}}^{(2)1-1} \right] , \\
[\hat{\mathbf{r}}\hat{\mathbf{r}}Y_{lm}]_s &= \sqrt{\frac{(l+1)(l+2)}{(2l+1)(2l+3)}} \mathbf{T}_{\mathbf{lm}}^{(2)1+2} - \sqrt{\frac{2l(l+1)}{3(2l-1)(2l+3)}} \mathbf{T}_{\mathbf{lm}}^{(2)1} \\
&\quad + \sqrt{\frac{l(l-1)}{(2l+1)(2l-1)}} \mathbf{T}_{\mathbf{lm}}^{(2)1-2} - \frac{1}{\sqrt{3}} \mathbf{T}_{\mathbf{lm}}^{(0)1} .
\end{aligned} \tag{A.21}$$

The subscript “ s ” denotes the symmetric part of a tensor. This new TSH basis (Equations (A.21)) is defined as a complete set of linearly independent coordinates for a rank-two symmetric tensor. When written in spherical coordinates, Zerilli (1970) shows that these terms can be further arranged into six orthonormal unit tensors,

of which $\mathbf{T}_{\text{lm}}^{\text{L}_0}$ is the fully radial coordinate, $\mathbf{T}_{\text{lm}}^{\text{T}_0}$ is the transverse portion of the trace, $\mathbf{T}_{\text{lm}}^{\text{E}_1}$ and $\mathbf{T}_{\text{lm}}^{\text{B}_1}$ are mixed radial/transverse components, and $\mathbf{T}_{\text{lm}}^{\text{E}_2}$, $\mathbf{T}_{\text{lm}}^{\text{B}_2}$ are fully transverse. The final form of the TSH basis, in the notation of Thorne (1980), is:

$$\begin{aligned}\mathbf{T}_{\text{lm}}^{\text{L}_0} &= [\hat{\mathbf{r}}\hat{\mathbf{r}}Y_{lm}]_s \ , \\ \mathbf{T}_{\text{lm}}^{\text{E}_1} &= r\sqrt{\frac{2}{l(l+1)}} [\hat{\mathbf{r}}\nabla Y_{lm}]_s \ , \\ \mathbf{T}_{\text{lm}}^{\text{B}_1} &= i\sqrt{\frac{2}{l(l+1)}} [\hat{\mathbf{r}}\mathbf{L}Y_{lm}]_s \ , \\ \mathbf{T}_{\text{lm}}^{\text{T}_0} &= -\frac{1}{\sqrt{2}l(l+1)} [r^2 [\nabla\nabla Y_{lm}]_s + r [\hat{\mathbf{r}}\nabla Y_{lm}]_s - [\mathbf{L}\mathbf{L}Y_{lm}]_s] \ , \\ \mathbf{T}_{\text{lm}}^{\text{E}_2} &= \sqrt{\frac{1}{2l(l+1)(l-1)(l+2)}} [r^2 [\nabla\nabla Y_{lm}]_s + 3r [\hat{\mathbf{r}}\nabla Y_{lm}]_s + [\mathbf{L}\mathbf{L}Y_{lm}]_s] \ , \\ \mathbf{T}_{\text{lm}}^{\text{B}_2} &= ir\sqrt{\frac{2}{l(l+1)(l-1)(l+2)}} \left[[\mathbf{L}\nabla Y_{lm}]_s + \frac{[\hat{\mathbf{r}}\mathbf{L}Y_{lm}]_s}{r} \right] \ .\end{aligned}$$

Writing these basis tensors explicitly in spherical coordinates ($\hat{\mathbf{e}}_r, \hat{\mathbf{e}}_\theta, \hat{\mathbf{e}}_\phi$) can give further insight into their structure.

$$\begin{aligned}\mathbf{T}_{\text{lm}}^{\text{L}_0} &= \begin{bmatrix} Y_{lm} & 0 & 0 \\ 0 & 0 & 0 \\ 0 & 0 & 0 \end{bmatrix} \ , \quad \mathbf{T}_{\text{lm}}^{\text{E}_1} = \sqrt{\frac{1}{2l(l+1)}} \begin{bmatrix} 0 & \frac{\partial Y_{lm}}{\partial \theta} & \frac{1}{\sin \theta} \frac{\partial Y_{lm}}{\partial \phi} \\ \frac{\partial Y_{lm}}{\partial \theta} & 0 & 0 \\ \frac{1}{\sin \theta} \frac{\partial Y_{lm}}{\partial \phi} & 0 & 0 \end{bmatrix} \ , \\ \mathbf{T}_{\text{lm}}^{\text{B}_1} &= \sqrt{\frac{1}{2l(l+1)}} \begin{bmatrix} 0 & -\frac{1}{\sin \theta} \frac{\partial Y_{lm}}{\partial \phi} & \frac{\partial Y_{lm}}{\partial \theta} \\ -\frac{1}{\sin \theta} \frac{\partial Y_{lm}}{\partial \phi} & 0 & 0 \\ \frac{\partial Y_{lm}}{\partial \theta} & 0 & 0 \end{bmatrix} \ ,\end{aligned}$$

$$\mathbf{T}_{\mathbf{lm}}^{\mathbf{T}_0} = \frac{1}{\sqrt{2}} \begin{bmatrix} 0 & 0 & 0 \\ 0 & Y_{lm} & 0 \\ 0 & 0 & Y_{lm} \end{bmatrix},$$

$$\mathbf{T}_{\mathbf{lm}}^{\mathbf{E}_2} = \sqrt{\frac{1}{2l(l+1)(l-1)(l+2)}} \begin{bmatrix} 0 & 0 & 0 \\ 0 & W_{lm} & \frac{X_{lm}}{\sin \theta} \\ 0 & \frac{X_{lm}}{\sin \theta} & -W_{lm} \end{bmatrix},$$

$$\mathbf{T}_{\mathbf{lm}}^{\mathbf{B}_2} = \sqrt{\frac{1}{2l(l+1)(l-1)(l+2)}} \begin{bmatrix} 0 & 0 & 0 \\ 0 & -\frac{X_{lm}}{\sin \theta} & W_{lm} \\ 0 & W_{lm} & \frac{X_{lm}}{\sin \theta} \end{bmatrix},$$

where:

$$X_{lm} = 2 \frac{\partial}{\partial \phi} \left(\frac{\partial}{\partial \theta} - \cot \theta \right) Y_{lm}, \quad W_{lm} = \left(\frac{\partial^2}{\partial \theta^2} - \cot \theta \frac{\partial}{\partial \theta} - \frac{1}{\sin^2 \theta} \frac{\partial^2}{\partial \phi^2} \right) Y_{lm}. \quad (\text{A.22})$$

This TSH basis (Equation (A.22)) can be employed to expand any arbitrary symmetric 3D tensor field (\mathbf{T}) in the following manner (Equation (A.23)).

$$\mathbf{T} = \sum_{m=-lmax}^{lmax} \sum_{l=|m|}^{lmax} (L_{lm}^0 \mathbf{T}_{\mathbf{lm}}^{\mathbf{L}_0} + E_{lm}^1 \mathbf{T}_{\mathbf{lm}}^{\mathbf{E}_1} + B_{lm}^1 \mathbf{T}_{\mathbf{lm}}^{\mathbf{B}_1} + T_{lm}^0 \mathbf{T}_{\mathbf{lm}}^{\mathbf{T}_0} + E_{lm}^2 \mathbf{T}_{\mathbf{lm}}^{\mathbf{E}_2} + B_{lm}^2 \mathbf{T}_{\mathbf{lm}}^{\mathbf{B}_2}) . \quad (\text{A.23})$$

Recasting the TSH coordinates into scalar spherical harmonic space (Novak et al., 2010), results in a simpler and more useful form of the TSH basis.

$$T^{rr} = \sum_{m=-lmax}^{lmax} \sum_{l=|m|}^{lmax} L_{lm}^0(r) Y_{lm} , \quad (\text{A.24})$$

$$T^\eta = \sum_{m=-lmax}^{lmax} \sum_{l=|m|}^{lmax} \sqrt{\frac{1}{2l(l+1)}} E_{lm}^1(r) Y_{lm} , \quad (\text{A.25})$$

$$T^\mu = \sum_{m=-lmax}^{lmax} \sum_{l=|m|}^{lmax} \sqrt{\frac{1}{2l(l+1)}} B_{lm}^1(r) Y_{lm} , \quad (\text{A.26})$$

$$T^\tau = \sum_{m=-lmax}^{lmax} \sum_{l=|m|}^{lmax} \sqrt{\frac{1}{2}} T_{lm}^0(r) Y_{lm} , \quad (\text{A.27})$$

$$T^W = \sum_{m=-lmax}^{lmax} \sum_{l=|m|}^{lmax} \sqrt{\frac{1}{2l(l+1)(l-1)(l+2)}} E_{lm}^2(r) Y_{lm} , \quad (\text{A.28})$$

$$T^X = \sum_{m=-lmax}^{lmax} \sum_{l=|m|}^{lmax} \sqrt{\frac{1}{2l(l+1)(l-1)(l+2)}} B_{lm}^2(r) Y_{lm} . \quad (\text{A.29})$$

The scalar TSH components (T^{rr} , T^η , T^μ , T^τ , T^W , T^X) can be expressed in terms of spherical coordinates (T^{rr} , $T^{\theta\theta}$, $T^{\phi\phi}$, $T^{r\theta}$, $T^{r\phi}$, $T^{\theta\phi}$), allowing for the transformation of field terms between the two bases (Novak et al., 2010). These relations can be built by using the spherical coordinate expression in Equation (A.22), substituting the new scalar TSH basis into the tensor field (Equation (A.23)).

The fully radial term (T^{rr}) corresponds to the radial coordinate $\mathbf{T}_{\mathbf{lm}}^{\mathbf{L}_0}$. The other two components of the trace ($T^{\theta\theta}$, $T^{\phi\phi}$) are spanned by the transverse components ($\mathbf{T}_{\mathbf{lm}}^{\mathbf{T}_0}$, $\mathbf{T}_{\mathbf{lm}}^{\mathbf{E}_2}$, $\mathbf{T}_{\mathbf{lm}}^{\mathbf{B}_2}$). By inspection of Equation (A.22), it is clear that $\mathbf{T}_{\mathbf{lm}}^{\mathbf{E}_2}$, $\mathbf{T}_{\mathbf{lm}}^{\mathbf{B}_2}$ are traceless, leaving only the single basis $\mathbf{T}_{\mathbf{lm}}^{\mathbf{T}_0}$ to fully describe the transverse trace (Equation (A.30)).

$$T^\tau = T^{\theta\theta} + T^{\phi\phi} . \quad (\text{A.30})$$

The total trace (T) can be written as:

$$T = T^{rr} + T^r . \quad (\text{A.31})$$

The two mixed radial/transverse components ($T^{r\theta}$, $T^{r\phi}$) are spanned by T^η and T^μ , corresponding to the tensor coordinates $\mathbf{T}_{\text{lm}}^{\mathbf{E}_1}$ and $\mathbf{T}_{\text{lm}}^{\mathbf{B}_1}$.

$$T^{r\theta} = \frac{\partial T^\eta}{\partial \theta} - \frac{1}{\sin \theta} \frac{\partial T^\mu}{\partial \phi} , \quad (\text{A.32})$$

$$T^{r\phi} = \frac{\partial T^\mu}{\partial \theta} + \frac{1}{\sin \theta} \frac{\partial T^\eta}{\partial \phi} . \quad (\text{A.33})$$

These relations take on a similar form to the VSH basis in spherical coordinates (Equations (A.12),(A.13)). The inverse relations for the TSH components (T^η , T^μ) can be derived in a similar manner to the VSH components in Equations (A.14),(A.15).

$$\nabla_{\theta\phi}^2 T^\eta = \frac{1}{\sin \theta} \frac{\partial}{\partial \theta} (\sin \theta T^{r\theta}) + \frac{1}{\sin \theta} \frac{\partial T^{r\phi}}{\partial \phi} , \quad (\text{A.34})$$

$$\nabla_{\theta\phi}^2 T^\mu = \frac{1}{\sin \theta} \frac{\partial}{\partial \theta} (\sin \theta T^{r\phi}) - \frac{1}{\sin \theta} \frac{\partial T^{r\theta}}{\partial \phi} . \quad (\text{A.35})$$

The last component in the spherical coordinate basis ($T^{\theta\phi}$) can be solved as a function of the scalar TSH components T^W and T^X , corresponding to the transverse traceless TSH basis ($\mathbf{T}_{\text{lm}}^{\mathbf{E}_2}$, $\mathbf{T}_{\text{lm}}^{\mathbf{B}_2}$).

$$T^{\theta\phi} = \frac{\partial^2 T^X}{\partial \theta^2} - \cot \theta \frac{\partial T^X}{\partial \theta} - \frac{1}{\sin^2 \theta} \frac{\partial^2 T^X}{\partial \phi^2} + 2 \frac{\partial}{\partial \theta} \left(\frac{1}{\sin \theta} \frac{\partial T^W}{\partial \phi} \right) . \quad (\text{A.36})$$

One more relation is required to solve for the transverse trace components ($t^{\theta\theta}$, $t^{\phi\phi}$) independently. Taking the difference of these two terms eliminates the trace ($\mathbf{T}_{\text{lm}}^{\mathbf{T}_0}$), resulting in a definition spanned by the transverse traceless components ($\mathbf{T}_{\text{lm}}^{\mathbf{E}_2}$, $\mathbf{T}_{\text{lm}}^{\mathbf{B}_2}$).

$$P = \frac{T^{\theta\theta} - T^{\phi\phi}}{2} = \frac{\partial^2 T^W}{\partial\theta^2} - \cot\theta \frac{\partial T^W}{\partial\theta} - \frac{1}{\sin^2\theta} \frac{\partial^2 T^W}{\partial\phi^2} - 2 \frac{\partial}{\partial\theta} \left(\frac{1}{\sin\theta} \frac{\partial T^X}{\partial\phi} \right). \quad (\text{A.37})$$

The inverse relations for the tranverse TSH components (T^X , T^W) can be computed through the application of the operator: $\nabla_{\theta\phi}^2 (\nabla_{\theta\phi}^2 + 2)$, followed by the substitution of the spherical coordinate definitions (Equations (A.36),(A.37)).

$$\begin{aligned} \nabla_{\theta\phi}^2 (\nabla_{\theta\phi}^2 + 2) T^X &= \frac{\partial^2 T^{\theta\phi}}{\partial\theta^2} + \frac{3}{\tan\theta} \frac{\partial T^{\theta\phi}}{\partial\theta} - \frac{1}{\sin^2\theta} \frac{\partial^2 T^{\theta\phi}}{\partial\phi^2} \\ &\quad - 2T^{\theta\phi} - \frac{2}{\sin\theta} \frac{\partial}{\partial\phi} \left(\frac{\partial P}{\partial\theta} + \frac{P}{\tan\theta} \right), \end{aligned} \quad (\text{A.38})$$

$$\begin{aligned} \nabla_{\theta\phi}^2 (\nabla_{\theta\phi}^2 + 2) T^W &= \frac{\partial^2 P}{\partial\theta^2} + \frac{3}{\tan\theta} \frac{\partial P}{\partial\theta} - \frac{1}{\sin^2\theta} \frac{\partial^2 P}{\partial\phi^2} \\ &\quad - 2P + \frac{2}{\sin\theta} \frac{\partial}{\partial\phi} \left(\frac{\partial T^{\theta\phi}}{\partial\theta} + \frac{T^{\theta\phi}}{\tan\theta} \right). \end{aligned} \quad (\text{A.39})$$

These relations allow for the transformation of field variables between spherical coordinates and the TSH basis.

A.3 Properties

The Vector and Tensor Spherical Harmonics have the same properties as scalar spherical harmonics, such as symmetry:

$$\begin{aligned} \mathbf{Y}_{1,-m} &= (-1)^m \mathbf{Y}_{1m}^*, & \mathbf{T}_{1,-m}^{\mathbf{L}_0} &= (-1)^m \mathbf{T}_{1m}^{\mathbf{L}_0*}, & \mathbf{T}_{1,-m}^{\mathbf{T}_0} &= (-1)^m \mathbf{T}_{1m}^{\mathbf{T}_0*}, \\ \mathbf{\Psi}_{1,-m} &= (-1)^m \mathbf{\Psi}_{1m}^*, & \mathbf{T}_{1,-m}^{\mathbf{E}_1} &= (-1)^m \mathbf{T}_{1m}^{\mathbf{E}_1*}, & \mathbf{T}_{1,-m}^{\mathbf{E}_2} &= (-1)^m \mathbf{T}_{1m}^{\mathbf{E}_2*}, \\ \mathbf{\Phi}_{1,-m} &= (-1)^m \mathbf{\Phi}_{1m}^*, & \mathbf{T}_{1,-m}^{\mathbf{B}_1} &= (-1)^m \mathbf{T}_{1m}^{\mathbf{B}_1*}, & \mathbf{T}_{1,-m}^{\mathbf{B}_2} &= (-1)^m \mathbf{T}_{1m}^{\mathbf{B}_2*}. \end{aligned}$$

Being a linearly independent basis, the unit coordinates satisfy orthogonality.

$$\begin{aligned}
\mathbf{Y}_{1,m} \cdot \boldsymbol{\Psi}_{1,m} &= 0 , \\
\mathbf{Y}_{1,m} \cdot \boldsymbol{\Phi}_{1,m} &= 0 , & \mathbf{T}_{1m}^{\alpha\beta} \cdot \mathbf{T}_{1m}^{\gamma\delta} &= 0 . \\
\boldsymbol{\Psi}_{1,m} \cdot \boldsymbol{\Phi}_{1,m} &= 0 ,
\end{aligned}$$

The vector and tensor bases also satisfy orthogonality in Hilbert space.

$$\begin{aligned}
\int \mathbf{Y}_{lm} \cdot \mathbf{Y}_{l'm'}^* &= \delta_{ll'} \delta_{mm'} , \\
\int \boldsymbol{\Psi}_{lm} \cdot \boldsymbol{\Psi}_{l'm'}^* &= l(l+1) \delta_{ll'} \delta_{mm'} , & \int \mathbf{T}_{lm}^{\alpha\beta} \cdot \mathbf{T}_{l'm'}^{\gamma\delta*} &= \delta_{\alpha\gamma} \delta_{\beta\delta} \delta_{ll'} \delta_{mm'} . \\
\int \boldsymbol{\Phi}_{lm} \cdot \boldsymbol{\Phi}_{l'm'}^* &= l(l+1) \delta_{ll'} \delta_{mm'} ,
\end{aligned}$$

A.4 Divergence

The divergence of a vector field in the VSH basis can be defined by taking the divergence of each basis coordinate (Equations (A.1)-(A.3)).

$$\begin{aligned}
\nabla \cdot (f(r) \mathbf{Y}_{lm}) &= \left(\frac{df}{dr} + \frac{2}{r} f \right) Y_{lm} , \\
\nabla \cdot (f(r) \boldsymbol{\Psi}_{lm}) &= -\frac{l(l+1)}{r} f Y_{lm} , \\
\nabla \cdot (f(r) \boldsymbol{\Phi}_{lm}) &= 0 .
\end{aligned}$$

By definition, the $\boldsymbol{\Phi}$ coordinate is a curl, resulting in a zero divergence. The other coordinates can be merged to define the divergence of a field (\mathbf{v}) in the VSH basis.

$$\nabla \cdot \mathbf{v} = \sum_{m=-lmax}^{lmax} \sum_{l=|m|}^{lmax} \left(\frac{dv_{lm}^r}{dr} + \frac{2}{r} v_{lm}^r - \frac{l(l+1)}{r} v_{lm}^{(1)} \right) Y_{lm} . \quad (\text{A.40})$$

The divergence can be written in real space by substituting in the definitions for the scalar VSH coordinates (Equations (A.9)-(A.11)).

$$\nabla \cdot \mathbf{v} = \frac{dv^r}{dr} + \frac{2}{r}v^r + \frac{1}{r}\nabla_{\theta\phi}^2 v^\eta. \quad (\text{A.41})$$

The divergence of a tensor field (\mathbf{T}) in the TSH basis can be derived from the covariant divergence of a contravariant tensor (T^{ij}) (Equation (A.18)) in spherical coordinates (Equation (A.17)).

$$\nabla \cdot \mathbf{T} = \begin{cases} [\nabla \cdot \mathbf{T}]^r = \frac{1}{r^2} \frac{\partial}{\partial r} (r^2 T^{rr}) + \frac{1}{r \sin \theta} \frac{\partial}{\partial \theta} (\sin \theta T^{r\theta}) + \frac{1}{r \sin \theta} \frac{\partial T^{r\phi}}{\partial \phi} - \frac{T^{\theta\theta} + T^{\phi\phi}}{r}, \\ [\nabla \cdot \mathbf{T}]^\theta = \frac{1}{r^3} \frac{\partial}{\partial r} (r^3 T^{r\theta}) + \frac{1}{r \sin \theta} \frac{\partial}{\partial \theta} (\sin \theta T^{\theta\theta}) + \frac{1}{r \sin \theta} \frac{\partial T^{\theta\phi}}{\partial \phi} - \frac{T^{\phi\phi}}{r \tan \theta}, \\ [\nabla \cdot \mathbf{T}]^\phi = \frac{1}{r^3} \frac{\partial}{\partial r} (r^3 T^{r\phi}) + \frac{1}{r} \frac{\partial T^{\theta\phi}}{\partial \theta} + \frac{1}{r \sin \theta} \frac{\partial T^{\phi\phi}}{\partial \phi} + \frac{2T^{\theta\phi}}{r \tan \theta}. \end{cases} \quad (\text{A.42})$$

The spherical coordinate components of the tensor (T^{rr} , $T^{\theta\theta}$, $T^{\phi\phi}$, $T^{r\theta}$, $T^{r\phi}$, $T^{\theta\phi}$) can be written in terms of the scalar TSH components (T^{rr} , T^η , T^μ , T^τ , T^W , T^X) using the TSH basis definitions in Equations (A.30)-(A.39). The spherical coordinate components of the divergence ($[\nabla \cdot \mathbf{T}]^r$, $[\nabla \cdot \mathbf{T}]^\theta$, $[\nabla \cdot \mathbf{T}]^\phi$) can similarly be defined in the VSH basis using the relationships in Equations (A.12)-(A.15).

$$\begin{aligned} [\nabla \cdot \mathbf{T}]^r &= \frac{1}{r^2} \frac{\partial}{\partial r} (r^2 T^{rr}) + \frac{1}{r} (\nabla_{\theta\phi}^2 T^\eta - T^\tau), \\ [\nabla \cdot \mathbf{T}]^\eta &= \nabla_{\theta\phi}^2 \left[\frac{1}{r^3} \frac{\partial}{\partial r} (r^3 T^\eta) + \frac{1}{r} \left((\nabla_{\theta\phi}^2 + 2) T^W + \frac{T^\tau}{2} \right) \right], \\ [\nabla \cdot \mathbf{T}]^\mu &= \nabla_{\theta\phi}^2 \left[\frac{1}{r^3} \frac{\partial}{\partial r} (r^3 T^\mu) + \frac{1}{r} (\nabla_{\theta\phi}^2 + 2) T^X \right]. \end{aligned} \quad (\text{A.43})$$

The tensor divergence (Equation (A.43)) can be expressed in its spherical harmonic decomposition by expanding the TSH components in terms of the scalar spherical harmonic as defined in Equations (A.24)-(A.29)).

$$\begin{aligned}
[\nabla \cdot \mathbf{T}]^r &= \sum_{m=-lmax}^{lmax} \sum_{l=|m|}^{lmax} \left[\frac{1}{r^2} \frac{\partial}{\partial r} (r^2 L_{lm}^0) - \frac{1}{r} (l(l+1)E_{lm}^1 + T_{lm}^0) \right] Y_{lm} , \\
[\nabla \cdot \mathbf{T}]^\eta &= \sum_{m=-lmax}^{lmax} \sum_{l=|m|}^{lmax} -l(l+1) \left[\frac{1}{r^3} \frac{\partial}{\partial r} (r^3 E_{lm}^1) + \frac{1}{r} \left(\frac{T_{lm}^0}{2} - (l-1)(l+2)E_{lm}^2 \right) \right] Y_{lm} , \\
[\nabla \cdot \mathbf{T}]^\mu &= \sum_{m=-lmax}^{lmax} \sum_{l=|m|}^{lmax} -l(l+1) \left[\frac{1}{r^3} \frac{\partial}{\partial r} (r^3 B_{lm}^1) - \frac{(l-1)(l+2)}{r} B_{lm}^2 \right] Y_{lm} .
\end{aligned} \tag{A.44}$$

A.5 Curl

The curl of a vector field can be defined in a similar way to the divergence, by taking the curl of the components of some field (f) in the VSH basis.

$$\begin{aligned}
\nabla \times (f(r)\mathbf{Y}_{lm}) &= -\frac{1}{r}f\mathbf{\Phi}_{lm} \\
\nabla \times (f(r)\mathbf{\Psi}_{lm}) &= \left(\frac{df}{dr} + \frac{1}{r}f \right) \mathbf{\Phi}_{lm} \\
\nabla \times (f(r)\mathbf{\Phi}_{lm}) &= -\frac{l(l+1)}{r}f\mathbf{Y}_{lm} - \left(\frac{df}{dr} + \frac{1}{r}f \right) \mathbf{\Psi}_{lm}
\end{aligned}$$

These components can be merged to define the curl of a vector field ($\nabla \times \mathbf{v}$).

$$\begin{aligned}
\nabla \times \mathbf{v} &= \sum_{m=-lmax}^{lmax} \sum_{l=|m|}^{lmax} \left(-\frac{l(l+1)}{r}v_{lm}^{(2)}\mathbf{Y}_{lm} - \left(\frac{\partial v_{lm}^{(2)}}{\partial r} + \frac{1}{r}v_{lm}^{(2)} \right) \mathbf{\Psi}_{lm} \right. \\
&\quad \left. + \left(-\frac{1}{r}v_{lm}^r + \frac{\partial v_{lm}^{(1)}}{\partial r} + \frac{1}{r}v_{lm}^{(1)} \right) \mathbf{\Phi}_{lm} \right) \tag{A.45}
\end{aligned}$$

The curl (Equation (A.45)) can be written in real-space using the scalar VSH components defined in Section A.1.

$$\begin{aligned}[\nabla \times \mathbf{v}]^r &= \frac{1}{r} \nabla_{\theta\phi}^2 v^\eta \\[\nabla \times \mathbf{v}]^\eta &= -\frac{1}{r} \frac{\partial}{\partial r} (r v^\mu) \\[\nabla \times \mathbf{v}]^\mu &= \frac{1}{r} \left(-v^r + \frac{\partial}{\partial r} (r E^\eta) \right)\end{aligned}$$

APPENDIX B

RECURSION RELATIONS

This appendix contains the full description and derivation of the recursion relations employed by transformations between the vector and tensor spherical harmonic coordinate bases described in Appendix A.

B.1 Calculating Clebsch-Gordan Coefficients

In the formulation of the GALE code, various sets of spherical harmonic (Y_{lm}) terms are convolved during the computation of the potential flow in spherical harmonic space. The relevant convolutions can be solved explicitly in their full form, starting with the definition of the convolution identity in its canonical Clebsch-Gordan form (Landau & Lifshitz, 1977):

$$Y_{l_1 m_1} Y_{l_2 m_2} = \sum_{L, M} \sqrt{\frac{(2l_1 + 1)(2l_2 + 1)}{4\pi(2L + 1)}} \langle l_1 0 l_2 0 | L 0 \rangle \langle l_1 m_1 l_2 m_2 | LM \rangle Y_{LM} , \quad (\text{B.1})$$

where L and M are the coupled spherical harmonic degree and angular momentum, under the following selection rules: $M = m_1 + m_2$ and $|l_1 - l_2| \leq L \leq l_1 + l_2$. $\langle l_1 0 l_2 0 | L 0 \rangle$ and $\langle l_1 m_1 l_2 m_2 | LM \rangle$ are the Clebsch-Gordan (CG) Coefficients (Landau & Lifshitz, 1977). The spherical harmonic convolutions relevant to this formulation ($Y_{00}Y_{lm}$, $Y_{10}Y_{lm}$, $Y_{20}Y_{lm}$) can be explicitly expanded using these identities.

The convolution identity (Equation (B.1)) can be used to express the definition of $Y_{00}Y_{lm}$ as follows:

$$Y_{00}Y_{lm} = \sum_L \sqrt{\frac{(2l + 1)}{4\pi(2L + 1)}} \langle 0 0 l 0 | L 0 \rangle \langle 0 0 l m | L m \rangle Y_{Lm} .$$

The selection rules call for the superposition of all values of L simultaneously, however, since there is only a single value of L ($L = l$), the sum can be written as:

$$Y_{00}Y_{lm} = \sqrt{\frac{1}{4\pi}} \langle 0 \ 0 \ l \ 0 | L \ 0 \rangle \langle 0 \ 0 \ l \ m | L \ m \rangle Y_{lm} .$$

The definition of this special case of CG coefficients is unity (Varshalovich et al., 1988), resulting in the final form of the convolution identity for $Y_{00}Y_{lm}$.

$$Y_{00}Y_{lm} = \sqrt{\frac{1}{4\pi}} Y_{lm} . \quad (\text{B.2})$$

The next convolution term ($Y_{10}Y_{lm}$) can also be written with help of the convolution identity (Equation (B.1)).

$$Y_{10}Y_{lm} = \sum_L \sqrt{\frac{3(2l+1)}{4\pi(2L+1)}} \langle 1 \ 0 \ l \ 0 | L \ 0 \rangle \langle 1 \ 0 \ l \ m | L \ m \rangle Y_{Lm} .$$

The sum is explicitly expressed as a superposition of all allowable degrees of L ($L = l - 1, L = l, L = l + 1$).

$$\begin{aligned} Y_{10}Y_{lm} = & \sqrt{\frac{3(2l+1)}{4\pi(2l+3)}} \langle 1 \ 0 \ l \ 0 | l+1 \ 0 \rangle \langle 1 \ 0 \ l \ m | l+1 \ m \rangle Y_{l+1,m} \\ & + \sqrt{\frac{3}{4\pi}} \langle 1 \ 0 \ l \ 0 | l \ 0 \rangle \langle 1 \ 0 \ l \ m | l \ m \rangle Y_{lm} \\ & + \sqrt{\frac{3(2l+1)}{4\pi(2l-1)}} \langle 1 \ 0 \ l \ 0 | l-1 \ 0 \rangle \langle 1 \ 0 \ l \ m | l-1 \ m \rangle Y_{l-1,m} . \end{aligned}$$

Calculating these CG coefficients directly is overly cumbersome, however, there are a few special cases which have been precomputed and are formulated in Table (8.2) of Varshalovich et al. (1988) as follows:

$$\begin{aligned} \langle 1 \ 0 \ l \ 0 | (l+1) \ 0 \rangle \langle 1 \ 0 \ l \ m | (l+1) \ m \rangle &= \left(\sqrt{\frac{(l+1)}{(2l+1)}} \right) \left(\sqrt{\frac{(l-m+1)(l+m+1)}{(2l+1)(l+1)}} \right), \\ \langle 1 \ 0 \ l \ 0 | l \ 0 \rangle \langle 1 \ 0 \ l \ m | l \ m \rangle &= 0, \\ \langle 1 \ 0 \ l \ 0 | (l-1) \ 0 \rangle \langle 1 \ 0 \ l \ m | (l-1) \ m \rangle &= \left(-\frac{l}{\sqrt{l(2l+1)}} \right) \left(-\sqrt{\frac{(l-m)(l+m)}{l(2l+1)}} \right). \end{aligned}$$

The convolution identity ($Y_{10}Y_{lm}$) can be defined explicitly, using these relations.

$$Y_{10}Y_{lm} = \sqrt{\frac{3(l-m+1)(l+m+1)}{4\pi(2l+3)(2l+1)}} Y_{l+1,m} + \sqrt{\frac{3(l-m)(l+m)}{4\pi(2l-1)(2l+1)}} Y_{l-1,m}. \quad (\text{B.3})$$

The final convolution term ($Y_{20}Y_{lm}$) will be solved using the same approach, starting with the convolution identity (Equation (B.1)).

$$Y_{20}Y_{lm} = \sum_L \sqrt{\frac{5(2l+1)}{4\pi(2L+1)}} \langle 2 \ 0 \ l \ 0 | L \ 0 \rangle \langle 2 \ 0 \ l \ m | L \ m \rangle Y_{Lm}.$$

Opening up the sum as a superposition of all allowable degrees of L ($L = l+2$, $L = l+1$, $L = l$, $L = l-1$, $L = l-2$) results in:

$$\begin{aligned} Y_{20}Y_{lm} &= \sqrt{\frac{5(2l+1)}{4\pi(2l+5)}} \langle 2 \ 0 \ l \ 0 | l+2 \ 0 \rangle \langle 2 \ 0 \ l \ m | l+2 \ m \rangle Y_{l+2,m} \\ &+ \sqrt{\frac{5(2l+1)}{4\pi(2l+3)}} \langle 2 \ 0 \ l \ 0 | l+1 \ 0 \rangle \langle 2 \ 0 \ l \ m | l+1 \ m \rangle Y_{l+1,m} \\ &+ \sqrt{\frac{5}{4\pi}} \langle 2 \ 0 \ l \ 0 | l \ 0 \rangle \langle 2 \ 0 \ l \ m | l \ m \rangle Y_{lm} \\ &+ \sqrt{\frac{5(2l+1)}{4\pi(2l-1)}} \langle 2 \ 0 \ l \ 0 | l-1 \ 0 \rangle \langle 2 \ 0 \ l \ m | l-1 \ m \rangle Y_{l-1,m} \\ &+ \sqrt{\frac{5(2l+1)}{4\pi(2l-3)}} \langle 2 \ 0 \ l \ 0 | l-2 \ 0 \rangle \langle 2 \ 0 \ l \ m | l-2 \ m \rangle Y_{l-2,m}. \end{aligned}$$

The CG coefficients for this term ($Y_{20}Y_{lm}$) can also be found precomputed in Table (8.4) of Varshalovich et al. (1988).

$$\begin{aligned}
\langle 2\ 0\ l\ 0 | l+2\ 0 \rangle &= \sqrt{\frac{3(l+1)(l+2)(l+1)}{(2l+1)(2l+2)(2l+3)}}, \\
\langle 2\ 0\ l\ m | l+2\ m \rangle &= \sqrt{\frac{3(l+1+m)(l+2+m)(l+1-m)(l+2-m)}{(2l+1)(2l+2)(2l+3)(l+2)}}, \\
\langle 2\ 0\ l\ 0 | l+1\ 0 \rangle &= 0\sqrt{\frac{3(l+1)(l+1)}{l(2l+1)(l+1)(l+2)}} = 0, \\
\langle 2\ 0\ l\ m | l+1\ m \rangle &= m\sqrt{\frac{3(l+1+m)(l+1-m)}{l(2l+1)(l+1)(l+2)}}, \\
\langle 2\ 0\ l\ 0 | l\ 0 \rangle &= -\frac{l(l+1)}{\sqrt{(2l-1)l(l+1)(2l+3)}}, \\
\langle 2\ 0\ l\ m | l\ m \rangle &= \frac{3m^2 - l(l+1)}{\sqrt{(2l-1)l(l+1)(2l+3)}}, \\
\langle 2\ 0\ l\ 0 | l-1\ 0 \rangle &= -0\sqrt{\frac{3l}{(l-1)(2l+1)(l+1)}} = 0, \\
\langle 2\ 0\ l\ m | l-1\ m \rangle &= -m\sqrt{\frac{3(l+m)(l-m)}{(l-1)l(2l+1)(l+1)}}, \\
\langle 2\ 0\ l\ 0 | l-2\ 0 \rangle &= \sqrt{\frac{3l(l-1)}{2(2l-1)(2l+1)}}, \\
\langle 2\ 0\ l\ m | l-2\ m \rangle &= \sqrt{\frac{3(l-1+m)(l+m)(l-1-m)(l-m)}{(l-1)(2l-1)(2l)(2l+1)}}.
\end{aligned}$$

The definition for the final convolution identity ($Y_{20}Y_{lm}$) can now be written explicitly using these relations.

$$\begin{aligned}
Y_{20}Y_{lm} = & \frac{3(l+1)}{(2l+2)(2l+3)} \sqrt{\frac{5(l+1+m)(l+2+m)(l+1-m)(l+2-m)}{4\pi(2l+1)(2l+5)}} Y_{l+2,m} \\
& - \frac{3m^2 - l(l+1)}{(2l-1)(2l+3)} \sqrt{\frac{5}{4\pi}} Y_{lm} \\
& + \frac{3}{2(2l-1)} \sqrt{\frac{5(l-1+m)(l+m)(l-1-m)(l-m)}{4\pi(2l-3)(2l+1)}} Y_{l-2,m} .
\end{aligned} \tag{B.4}$$

B.2 Deriving Recursion Relations

Various recursion relations are employed in computing the governing equations in spherical harmonic space. These include the application of simple trigonometric functions on the surface of a two-sphere $(\cos \theta, \sin^2 \theta)$, as well as the surface derivatives $(\sin \theta(\partial/\partial\theta), \partial/\partial\phi)$.

B.2.1 Surface functions

In order to define the recursion relation for the application of the cosine function $(\cos \theta)$, the function is first written in spherical harmonic space as:

$$\cos \theta = 2\sqrt{\frac{\pi}{3}} Y_{10} .$$

Taking the cosine of some function in spherical harmonic space $(f(r, \theta, \phi) = a_{lm}(r)Y_{lm}(\theta, \phi))$ results in the following convolution.

$$\cos \theta f(r, \theta, \phi) = 2a_{1m} \sqrt{\frac{\pi}{3}} Y_{10} Y_{lm} . \tag{B.5}$$

The Clebsch-Gordan coefficients that have been computed for this convolution in the previous section (Equation (B.3)) can be plugged into the cosine function (Equation (B.5)), resulting in the following recursion relation for cosine.

$$\cos \theta f(r, \theta, \phi) = a_{lm} \sqrt{\frac{(l-m+1)(l+m+1)}{(2l+3)(2l+1)}} Y_{l+1,m} + \sqrt{\frac{(l-m)(l+m)}{(2l-1)(2l+1)}} Y_{l-1,m} . \quad (\text{B.6})$$

To solve for the squared sine function ($\sin^2 \theta$), it is first written as a superposition of orthogonal spherical harmonics, which can be derived by inspection from the definition of a spherical harmonic in Section A.1, Equation (A.4).

$$\sin^2 \theta = \frac{4}{3} \sqrt{\pi} \left(Y_{00} - \sqrt{\frac{1}{5}} Y_{20} \right) .$$

Taking the square sine of some function decomposed in spherical harmonic space ($f(r, \theta, \phi) = a_{lm}(r) Y_{lm}(\theta, \phi)$), results in the two following convolutions.

$$\sin^2 \theta f(r, \theta, \phi) = \frac{4}{3} \sqrt{\pi} a_{lm} \left(Y_{00} Y_{lm} - \sqrt{\frac{1}{5}} Y_{20} Y_{lm} \right) . \quad (\text{B.7})$$

The definitions for coupled spherical harmonics that were derived in the previous section ($Y_{00} Y_{lm}$, $Y_{20} Y_{lm}$), Equations (B.2), (B.4), respectively, can be plugged into the squared sine function (Equation (B.7)) resulting in the following recursion relation for $\sin^2 \theta$.

$$\begin{aligned} \sin^2 \theta f(r, \theta, \phi) = a_{lm} \left(-\frac{1}{(2l+3)} \sqrt{\frac{[(l+1)^2 - m^2][(l+2)^2 - m^2]}{(2l+1)(2l+5)}} Y_{l+2,m} \right. \\ \left. + \frac{2(l^2 + l - 1 + m^2)}{(2l-1)(2l+3)} Y_{lm} - \frac{1}{(2l-1)} \sqrt{\frac{[(l-1)^2 - m^2](l^2 - m^2)}{(2l-3)(2l+1)}} Y_{l-2,m} \right) . \quad (\text{B.8}) \end{aligned}$$

B.2.2 Surface derivatives

The recursion relations for the surface derivatives can be derived using the derivative of the spherical harmonic function (Y_{lm}), defined in the Condon-Shortley convention in Appendix A, Equation (A.4).

$$Y_{lm} = (-1)^m \sqrt{\frac{(2l+1)(l-m)!}{4\pi(l+m)!}} P_l^m(\cos\theta) e^{im\phi} .$$

The surface derivatives of some function in spherical harmonic space ($f(r, \theta, \phi) = a_{lm}(r)Y_{lm}(\theta, \phi)$) are written as follows:

$$\begin{aligned} \frac{\partial f}{\partial \theta} &= a_{lm}(r) \frac{\partial}{\partial \theta} Y_{lm}(\theta, \phi) , \\ \frac{\partial f}{\partial \phi} &= a_{lm}(r) \frac{\partial}{\partial \phi} Y_{lm}(\theta, \phi) , \end{aligned}$$

where the derivatives of the spherical harmonic function (Y_{lm}) (Equation (A.4)) are

$$\frac{\partial Y_{lm}}{\partial \theta} = (-1)^m \sqrt{\frac{(2l+1)(l-m)!}{4\pi(l+m)!}} e^{im\phi} \frac{\partial}{\partial \theta} P_l^m(\cos\theta) , \quad (\text{B.9})$$

$$\frac{\partial Y_{lm}}{\partial \phi} = (-1)^m \sqrt{\frac{(2l+1)(l-m)!}{4\pi(l+m)!}} P_l^m(\cos\theta) \frac{\partial}{\partial \phi} e^{im\phi} . \quad (\text{B.10})$$

To compute the polar derivative (Equation (B.9)) as a recursion relation, the identity for the first derivative of the associated Legendre polynomial (P_l^m) can be employed.

$$\frac{dP_l^m(\mu)}{d\theta} = \frac{l\mu P_l^m(\mu) - (l+m)P_{l-1}^m(\mu)}{\sqrt{1-\mu^2}} , \quad \text{where } \mu = \cos\theta . \quad (\text{B.11})$$

Plugging this identity (Equation (B.11)) into the polar derivative of the spherical harmonic (Equation (B.9)), results in the relation:

$$\frac{\partial Y_{lm}}{\partial \theta} = (-1)^m \sqrt{\frac{(2l+1)(l-m)!}{4\pi(l+m)!}} e^{im\phi} \left(\frac{l \cos \theta P_l^m(\cos \theta) - (l+m)P_{l-1}^m(\cos \theta)}{\sin \theta} \right) .$$

Expanding this function and rewriting the Legendre polynomials as spherical harmonic terms, results in a recursion relation which can be multiplied by the sine function—leaving an equation that can be fully defined by a superposition of spherical harmonics.

$$\sin \theta \frac{\partial Y_{lm}}{\partial \theta} = l \cos \theta Y_{lm}(\theta, \phi) - \sqrt{\frac{2l+1}{2l-1}} (l^2 - m^2) Y_{l-1,m}(\theta, \phi) . \quad (\text{B.12})$$

The cosine function can be computed in spherical harmonic space using the recursion relation derived in the previous section (Equation (B.6)). Plugging this definition into the polar derivative (Equation (B.12)) results in a spectral recursion relation for the polar surface derivative.

$$\sin \theta \frac{\partial Y_{lm}}{\partial \theta} = l \sqrt{\frac{(l-m+1)(l+m+1)}{(2l+3)(2l+1)}} Y_{l+1,m} - (l+1) \sqrt{\frac{(l-m)(l+m)}{(2l-1)(2l+1)}} Y_{l-1,m} . \quad (\text{B.13})$$

The solution for the azimuthal derivative (Equation (B.10)) is trivial and can be written as follows:

$$\frac{\partial Y_{lm}}{\partial \phi} = im(-1)^m \sqrt{\frac{(2l+1)(l-m)!}{4\pi(l+m)!}} P_l^m(\cos \theta) e^{im\phi} . \quad (\text{B.14})$$

This relation (Equation (B.14)) can easily be expressed in terms of the spherical harmonic function (Y_{lm}).

$$\frac{\partial Y_{lm}}{\partial \phi} = im Y_{lm} . \quad (\text{B.15})$$

The definition of the azimuthal derivative (Equation (B.15)) can be reformulated in real spherical harmonic space as:

$$\begin{aligned}\frac{\partial Y_{lm}}{\partial \phi} &= -|m|Y_{l,-m} , \\ \frac{\partial Y_{l,0}}{\partial \phi} &= 0 , \\ \frac{\partial Y_{l,-m}}{\partial \phi} &= |m|Y_{l,m} .\end{aligned}\tag{B.16}$$

REFERENCES

- Augustson, K., Brun, A. S., Miesch, M., & Toomre, J. 2015. Grand Minima and Equatorward Propagation in a Cycling Stellar Convective Dynamo. *ApJ*, 809, 149, doi: [10.1088/0004-637X/809/2/149](https://doi.org/10.1088/0004-637X/809/2/149)
- Babcock, H. W. 1961. The Topology of the Sun's Magnetic Field and the 22-YEAR Cycle. *ApJ*, 133, 572, doi: [10.1086/147060](https://doi.org/10.1086/147060)
- Baldner, C. S., & Schou, J. 2012. Effects of Asymmetric Flows in Solar Convection on Oscillation Modes. *ApJ*, 760, L1, doi: [10.1088/2041-8205/760/1/L1](https://doi.org/10.1088/2041-8205/760/1/L1)
- Barekat, A., Schou, J., & Gizon, L. 2014. The Radial Gradient of the Near-Surface Shear Layer of the Sun. *A&A*, 570, L12, doi: [10.1051/0004-6361/201424839](https://doi.org/10.1051/0004-6361/201424839)
- Bekki, Y., & Yokoyama, T. 2017. Double-cell-type Solar Meridional Circulation Based on a Mean-field Hydrodynamic Model. *ApJ*, 835, 9, doi: [10.3847/1538-4357/835/1/9](https://doi.org/10.3847/1538-4357/835/1/9)
- Bogart, R. S., Baldner, C. S., & Basu, S. 2015. Evolution of Near-surface Flows Inferred from High-resolution Ring-diagram Analysis. *ApJ*, 807, 125, doi: [10.1088/0004-637X/807/2/125](https://doi.org/10.1088/0004-637X/807/2/125)
- Bonanno, A., Elstner, D., Rüdiger, G., & Belvedere, G. 2002. Parity Properties of an Advection-dominated Solar α^2 Omega-dynamo. *A&A*, 390, 673, doi: [10.1051/0004-6361:20020590](https://doi.org/10.1051/0004-6361:20020590)
- Böning, V. G. A. 2018. Ambiguity of the Solar Meridional Flow. *IAU Symposium*, 340, 13, doi: [10.1017/S1743921318001837](https://doi.org/10.1017/S1743921318001837)
- Böning, V. G. A., Roth, M., Jackiewicz, J., & Kholikov, S. 2017. Inversions for Deep Solar Meridional Flow Using Spherical Born Kernels. *ApJ*, 845, 2, doi: [10.3847/1538-4357/aa7af0](https://doi.org/10.3847/1538-4357/aa7af0)
- Brandenburg, A. 2005. The Case for a Distributed Solar Dynamo Shaped by Near-Surface Shear. *ApJ*, 625, 539, doi: [10.1086/429584](https://doi.org/10.1086/429584)
- Brandenburg, A., & Subramanian, K. 2005. Astrophysical Magnetic Fields and Nonlinear Dynamo Theory. *Phys. Rep.*, 417, 1, doi: [10.1016/j.physrep.2005.06.005](https://doi.org/10.1016/j.physrep.2005.06.005)

- Braun, D. C., & Birch, A. C. 2008. Prospects for the Detection of the Deep Solar Meridional Circulation. *ApJ*, 689, L161, doi: [10.1086/595884](https://doi.org/10.1086/595884)
- Braun, D. C., Birch, A. C., Benson, D., Stein, R. F., & Nordlund, Å. 2007. Helioseismic Holography of Simulated Solar Convection and Prospects for the Detection of Small-Scale Subsurface Flows. *ApJ*, 669, 1395, doi: [10.1086/521782](https://doi.org/10.1086/521782)
- Brun, A. S., Miesch, M. S., & Toomre, J. 2004. Global-scale Turbulent Convection and Magnetic Dynamo Action in the Solar Envelope. *ApJ*, 614, 1073, doi: [10.1086/423835](https://doi.org/10.1086/423835)
- Brun, A. S., & Toomre, J. 2002. Turbulent Convection under the Influence of Rotation: Sustaining a Strong Differential Rotation. *ApJ*, 570, 865, doi: [10.1086/339228](https://doi.org/10.1086/339228)
- Cameron, R., Gizon, L., & Duvall, T. L., J. 2008. Helioseismology of Sunspots: Confronting Observations with Three-dimensional MHD Simulations of Wave Propagation. *Sol. Phys.*, 251, 291, doi: [10.1007/s11207-008-9148-1](https://doi.org/10.1007/s11207-008-9148-1)
- Chaplin, W. J., Elsworth, Y., Isaak, G. R., et al. 1996. Solar Core Rotation from Low-degree BiSON p-mode Splittings: 1981-95. *MNRAS*, 283, L31, doi: [10.1093/mnras/283.2.L31](https://doi.org/10.1093/mnras/283.2.L31)
- Charbonneau, P. 2010. Dynamo Models of the Solar Cycle. *Living Rev. Sol. Phys.*, 7, 3, doi: [10.12942/lrsp-2010-3](https://doi.org/10.12942/lrsp-2010-3)
- Chatterjee, P., Nandy, D., & Choudhuri, A. R. 2004. Full-sphere Simulations of a Circulation-dominated Solar Dynamo: Exploring the Parity Issue. *A&A*, 427, 1019, doi: [10.1051/0004-6361:20041199](https://doi.org/10.1051/0004-6361:20041199)
- Chen, R. 2019. Helioseismic Measurements of the Sun's Meridional Circulation and Sunquakes. PhD thesis, Stanford Univ. https://stacks.stanford.edu/file/druid:rz950hb4219/thesis_submitted-augmented.pdf [accessed on May 1, 2021]
- Chen, R., & Zhao, J. 2017. A Comprehensive Method to Measure Solar Meridional Circulation and the Center-to-limb Effect Using Time-Distance Helioseismology. *ApJ*, 849, 144, doi: [10.3847/1538-4357/aa8eec](https://doi.org/10.3847/1538-4357/aa8eec)
- . 2018. Frequency Dependence of Helioseismic Measurements of the Center-to-Limb Effect and Flow-induced Travel-time Shifts. *ApJ*, 853, 161, doi: [10.3847/1538-4357/aaa3e3](https://doi.org/10.3847/1538-4357/aaa3e3)

- Christensen-Dalsgaard, J. 2002. Helioseismology. *Rev. Mod. Phys.*, 74, 1073, doi: [10.1103/RevModPhys.74.1073](https://doi.org/10.1103/RevModPhys.74.1073)
- . 2014, Lecture Notes on Stellar Oscillations (Aarhus: Aarhus Universitet, Institut for Fysik og Astronomi). <https://users-phys.au.dk/jcd/oscilnotes/> [accessed on May 1, 2021]
- Christensen-Dalsgaard, J., Dappen, W., Ajukov, S. V., et al. 1996. The Current State of Solar Modeling. *Science*, 272, 1286, doi: [10.1126/science.272.5266.1286](https://doi.org/10.1126/science.272.5266.1286)
- Claverie, A., Isaak, G. R., McLeod, C. P., van der Raay, H. B., & Cortes, T. R. 1979. Solar Structure from Global Studies of the 5-minute Oscillation. *Nature*, 282, 591, doi: [10.1038/282591a0](https://doi.org/10.1038/282591a0)
- Cossette, J.-F., Charbonneau, P., & Smolarkiewicz, P. K. 2013. Cyclic Thermal Signature in a Global MHD Simulation of Solar Convection. *ApJ*, 777, L29, doi: [10.1088/2041-8205/777/2/L29](https://doi.org/10.1088/2041-8205/777/2/L29)
- Cossette, J.-F., Charbonneau, P., Smolarkiewicz, P. K., & Rast, M. P. 2017. Magnetically Modulated Heat Transport in a Global Simulation of Solar Magneto-convection. *ApJ*, 841, 65, doi: [10.3847/1538-4357/aa6d60](https://doi.org/10.3847/1538-4357/aa6d60)
- Cowling, T. G. 1941. The Non-radial Oscillations of Polytropic Stars. *MNRAS*, 101, 367, doi: [10.1093/mnras/101.8.367](https://doi.org/10.1093/mnras/101.8.367)
- Cox, J. P., & Giuli, R. T. 1968, Principles of Stellar Structure (New York: Gordon and Breach). <https://ui.adsabs.harvard.edu/abs/1968pss..book.....C> [accessed on May 1, 2021]
- Di Mauro, M. P. 2003. Helioseismology: A Fantastic Tool to Probe the Interior of the Sun. In *The Sun's Surface and Subsurface: Investigating Shape*, ed. J. P. Rozelot, Vol. 599, 31–67, doi: [10.1007/3-540-45755-0_3](https://doi.org/10.1007/3-540-45755-0_3)
- Dikpati, M., & Charbonneau, P. 1999. A Babcock-Leighton Flux Transport Dynamo with Solar-like Differential Rotation. *ApJ*, 518, 508, doi: [10.1086/307269](https://doi.org/10.1086/307269)
- Dikpati, M., & Gilman, P. A. 2001. Flux-Transport Dynamos with α -Effect from Global Instability of Tachocline Differential Rotation: A Solution for Magnetic Parity Selection in the Sun. *ApJ*, 559, 428, doi: [10.1086/322410](https://doi.org/10.1086/322410)
- Domaradzki, J. A., Xiao, Z., & Smolarkiewicz, P. K. 2003. Effective Eddy Viscosities in Implicit Large Eddy Simulations of Turbulent Flows. *Phys. Fluids*, 15, 3890, doi: [10.1063/1.1624610](https://doi.org/10.1063/1.1624610)

- Domingo, V., Fleck, B., & Poland, A. I. 1995. The SOHO Mission: an Overview. *Sol. Phys.*, 162, 1, doi: [10.1007/BF00733425](https://doi.org/10.1007/BF00733425)
- Duvall, T. L., J. 1979. Large-scale Solar Velocity Fields. *Sol. Phys.*, 63, 3, doi: [10.1007/BF00155690](https://doi.org/10.1007/BF00155690)
- Duvall, T. L., J., Dziembowski, W. A., Goode, P. R., et al. 1984. Internal Rotation of the Sun. *Nature*, 310, 22, doi: [10.1038/310022a0](https://doi.org/10.1038/310022a0)
- Elliott, J. R., & Smolarkiewicz, P. K. 2002. Eddy Resolving Simulations of Turbulent Solar Convection. *Int. J. Num. Methods Fluids*, 39, 855, doi: <https://doi.org/10.1002/flid.333>
- Featherstone, N. A., & Miesch, M. S. 2015. Meridional Circulation in Solar and Stellar Convection Zones. *ApJ*, 804, 67, doi: [10.1088/0004-637X/804/1/67](https://doi.org/10.1088/0004-637X/804/1/67)
- Felipe, T., Braun, D. C., Crouch, A. D., & Birch, A. C. 2016. Helioseismic Holography of Simulated Sunspots: Magnetic and Thermal Contributions to Travel Times. *ApJ*, 829, 67, doi: [10.3847/0004-637X/829/2/67](https://doi.org/10.3847/0004-637X/829/2/67)
- Fossat, E., Boumier, P., Corbard, T., et al. 2017. Asymptotic g-modes: Evidence for a Rapid Rotation of the Solar Core. *A&A*, 604, A40, doi: [10.1051/0004-6361/201730460](https://doi.org/10.1051/0004-6361/201730460)
- Gastine, T., Yadav, R. K., Morin, J., Reiners, A., & Wicht, J. 2014. From Solar-like to Antisolar Differential Rotation in Cool Stars. *MNRAS*, 438, L76, doi: [10.1093/mnrasl/slt162](https://doi.org/10.1093/mnrasl/slt162)
- Germano, M., Piomelli, U., Moin, P., & Cabot, W. H. 1991. A Dynamic Subgrid-scale Eddy Viscosity Model. *Phys. Fluids A*, 3, 1760, doi: [10.1063/1.857955](https://doi.org/10.1063/1.857955)
- Ghizaru, M., Charbonneau, P., & Smolarkiewicz, P. K. 2010. Magnetic Cycles in Global Large-eddy Simulations of Solar Convection. *ApJ*, 715, L133, doi: [10.1088/2041-8205/715/2/L133](https://doi.org/10.1088/2041-8205/715/2/L133)
- Giles, P. M. 2000. Time-distance Measurements of Large-scale Flows in the Solar Convection Zone. PhD thesis, Stanford Univ. <https://ui.adsabs.harvard.edu/abs/2000PhDT.....9G> [accessed on May 1, 2021]
- Giles, P. M., Duvall, T. L., Scherrer, P. H., & Bogart, R. S. 1997. A Subsurface Flow of Material from the Sun's Equator to its Poles. *Nature*, 390, 52, doi: [10.1038/36294](https://doi.org/10.1038/36294)

- Gilman, P. A., & Miller, J. 1981. Dynamically Consistent Nonlinear Dynamos Driven by Convection in a Rotating Spherical Shell. *ApJS*, 46, 211, doi: [10.1086/190743](https://doi.org/10.1086/190743)
- Gizon, L., & Birch, A. C. 2004. Time-Distance Helioseismology: Noise Estimation. *ApJ*, 614, 472, doi: [10.1086/423367](https://doi.org/10.1086/423367)
- . 2005. Local Helioseismology. *Living Rev. Sol. Phys.*, 2, 6, doi: [10.12942/lrsp-2005-6](https://doi.org/10.12942/lrsp-2005-6)
- Gizon, L., Cameron, R. H., Pourabdian, M., et al. 2020. Meridional Flow in the Sun's Convection Zone is a Single Cell in each Hemisphere. *Science*, 368, 1469, doi: [10.1126/science.aaz7119](https://doi.org/10.1126/science.aaz7119)
- Gizon, L., Barucq, H., Duruflé, M., et al. 2017. Computational Helioseismology in the Frequency Domain: Acoustic Waves in Axisymmetric Solar Models with Flows. *A&A*, 600, A35, doi: [10.1051/0004-6361/201629470](https://doi.org/10.1051/0004-6361/201629470)
- Goldreich, P., Murray, N., & Kumar, P. 1994. Excitation of Solar p-modes. *ApJ*, 424, 466, doi: [10.1086/173904](https://doi.org/10.1086/173904)
- Grinstein, F. F., Margolin, L. G., & Rider, W. J. 2007, *Implicit Large Eddy Simulation: Computing Turbulent Fluid Dynamics* (Cambridge: Cambridge University Press), doi: [10.1017/CB09780511618604](https://doi.org/10.1017/CB09780511618604)
- Guerrero, G., & de Gouveia Dal Pino, E. M. 2008. Turbulent Magnetic Pumping in a Babcock-Leighton Solar Dynamo Model. *A&A*, 485, 267, doi: [10.1051/0004-6361:200809351](https://doi.org/10.1051/0004-6361:200809351)
- Guerrero, G., Smolarkiewicz, P. K., de Gouveia Dal Pino, E. M., Kosovichev, A. G., & Mansour, N. N. 2016. On the Role of Tachoclines in Solar and Stellar Dynamos. *ApJ*, 819, 104, doi: [10.3847/0004-637X/819/2/104](https://doi.org/10.3847/0004-637X/819/2/104)
- Guerrero, G., Smolarkiewicz, P. K., Kosovichev, A. G., & Mansour, N. N. 2013. Differential Rotation in Solar-like Stars from Global Simulations. *ApJ*, 779, 176, doi: [10.1088/0004-637X/779/2/176](https://doi.org/10.1088/0004-637X/779/2/176)
- Guerrero, G., Zaire, B., Smolarkiewicz, P. K., et al. 2019. What Sets the Magnetic Field Strength and Cycle Period in Solar-type Stars? *ApJ*, 880, 6, doi: [10.3847/1538-4357/ab224a](https://doi.org/10.3847/1538-4357/ab224a)
- Hanasoge, S. M., Duvall, T. L., J., & Couvidat, S. 2007. Validation of Helioseismology through Forward Modeling: Realization Noise Subtraction and Kernels. *ApJ*, 664, 1234, doi: [10.1086/519070](https://doi.org/10.1086/519070)

- Hanasoge, S. M., Larsen, R. M., Duvall, T. L., J., et al. 2006. Computational Acoustics in Spherical Geometry: Steps toward Validating Helioseismology. *ApJ*, 648, 1268, doi: [10.1086/505927](https://doi.org/10.1086/505927)
- Hartlep, T., Kosovichev, A. G., Zhao, J., & Mansour, N. N. 2011. Signatures of Emerging Subsurface Structures in Acoustic Power Maps of the Sun. *Sol. Phys.*, 268, 321, doi: [10.1007/s11207-010-9544-1](https://doi.org/10.1007/s11207-010-9544-1)
- Hartlep, T., Zhao, J., Kosovichev, A. G., & Mansour, N. N. 2013. Solar Wave-field Simulation for Testing Prospects of Helioseismic Measurements of Deep Meridional Flows. *ApJ*, 762, 132, doi: [10.1088/0004-637X/762/2/132](https://doi.org/10.1088/0004-637X/762/2/132)
- Hartlep, T., Zhao, J., Mansour, N. N., & Kosovichev, A. G. 2008. Validating Time-distance Far-side Imaging of Solar Active Regions through Numerical Simulations. *ApJ*, 689, 1373, doi: [10.1086/592721](https://doi.org/10.1086/592721)
- Harvey, J. W., Hill, F., Hubbard, R. P., et al. 1996. The Global Oscillation Network Group (GONG) Project. *Science*, 272, 1284, doi: [10.1126/science.272.5266.1284](https://doi.org/10.1126/science.272.5266.1284)
- Harvey, K. L., & Martin, S. F. 1973. Ephemeral Active Regions. *Sol. Phys.*, 32, 389, doi: [10.1007/BF00154951](https://doi.org/10.1007/BF00154951)
- Hathaway, D. H. 1996. Doppler Measurements of the Sun's Meridional Flow. *ApJ*, 460, 1027, doi: [10.1086/177029](https://doi.org/10.1086/177029)
- . 2012. Supergranules as Probes of the Sun's Meridional Circulation. *ApJ*, 760, 84, doi: [10.1088/0004-637X/760/1/84](https://doi.org/10.1088/0004-637X/760/1/84)
- Hathaway, D. H., Nandy, D., Wilson, R. M., & Reichmann, E. J. 2003. Evidence That a Deep Meridional Flow Sets the Sunspot Cycle Period. *ApJ*, 589, 665, doi: [10.1086/374393](https://doi.org/10.1086/374393)
- Hotta, H., Iijima, H., & Kusano, K. 2019. Weak Influence of Near-surface Layer on Solar Deep Convection Zone Revealed by Comprehensive Simulation from Base to Surface. *Sci. Adv.*, 5, 2307, doi: [10.1126/sciadv.aau2307](https://doi.org/10.1126/sciadv.aau2307)
- Hotta, H., & Yokoyama, T. 2011. Modeling of Differential Rotation in Rapidly Rotating Solar-type Stars. *ApJ*, 740, 12, doi: [10.1088/0004-637X/740/1/12](https://doi.org/10.1088/0004-637X/740/1/12)
- Howe, R., Larson, T. P., Schou, J., et al. 2011. First Global Rotation Inversions of HMI Data. *J. Phys.: Conf. Ser.*, 271, 012061, doi: [10.1088/1742-6596/271/1/012061](https://doi.org/10.1088/1742-6596/271/1/012061)

- Ilonidis, S., Zhao, J., & Hartlep, T. 2013. Helioseismic Investigation of Emerging Magnetic Flux in the Solar Convection Zone. *ApJ*, 777, 138, doi: [10.1088/0004-637X/777/2/138](https://doi.org/10.1088/0004-637X/777/2/138)
- Ilonidis, S., Zhao, J., & Kosovichev, A. 2011. Detection of Emerging Sunspot Regions in the Solar Interior. *Science*, 333, 993, doi: [10.1126/science.1206253](https://doi.org/10.1126/science.1206253)
- Jackiewicz, J., Serebryanskiy, A., & Kholikov, S. 2015. Meridional Flow in the Solar Convection Zone. II. Helioseismic Inversions of GONG Data. *ApJ*, 805, 133, doi: [10.1088/0004-637X/805/2/133](https://doi.org/10.1088/0004-637X/805/2/133)
- Jensen, J. M., Olsen, K. B., Duvall, Thomas L., J., & Jacobsen, B. H. 2003. Test of Helioseismic Time-distance Inversion using 3-D Finite-difference Wavefield Modeling. In *GONG+ 2002. Local and Global Helioseismology: the Present and Future*, ed. H. Sawaya-Lacoste, Vol. 517, 319–320. <https://ui.adsabs.harvard.edu/abs/2003ESASP.517..319J> [accessed on May 1, 2021]
- Käpylä, P. J., Käpylä, M. J., & Brandenburg, A. 2014. Confirmation of Bistable Stellar Differential Rotation Profiles. *A&A*, 570, A43, doi: [10.1051/0004-6361/201423412](https://doi.org/10.1051/0004-6361/201423412)
- Karak, B. B., Rheinhardt, M., Brandenburg, A., Käpylä, P. J., & Käpylä, M. J. 2014. Quenching and Anisotropy of Hydromagnetic Turbulent Transport. *ApJ*, 795, 16, doi: [10.1088/0004-637X/795/1/16](https://doi.org/10.1088/0004-637X/795/1/16)
- Kholikov, S., Serebryanskiy, A., & Jackiewicz, J. 2014. Meridional Flow in the Solar Convection Zone. I. Measurements from GONG Data. *ApJ*, 784, 145, doi: [10.1088/0004-637X/784/2/145](https://doi.org/10.1088/0004-637X/784/2/145)
- Khomenko, E., Kosovichev, A., Collados, M., Parchevsky, K., & Olshevsky, V. 2009. Theoretical Modeling of Propagation of Magnetoacoustic Waves in Magnetic Regions Below Sunspots. *ApJ*, 694, 411, doi: [10.1088/0004-637X/694/1/411](https://doi.org/10.1088/0004-637X/694/1/411)
- Kitchatinov, L. L. 2004. Differential Rotation and Meridional Circulation near the Boundaries of the Solar Convection Zone. *Astron. Rep.*, 48, 153, doi: [10.1134/1.1648079](https://doi.org/10.1134/1.1648079)
- Kitchatinov, L. L. 2013. Theory of Differential Rotation and Meridional Circulation. In *Solar and Astrophysical Dynamos and Magnetic Activity*, ed. A. G. Kosovichev, E. de Gouveia Dal Pino, & Y. Yan, Vol. 294, 399–410, doi: [10.1017/S1743921313002834](https://doi.org/10.1017/S1743921313002834)

- Kitchatinov, L. L., & Olemskoy, S. V. 2012. Differential Rotation of Main-sequence Dwarfs: Predicting the Dependence on Surface Temperature and Rotation Rate. *MNRAS*, 423, 3344, doi: [10.1111/j.1365-2966.2012.21126.x](https://doi.org/10.1111/j.1365-2966.2012.21126.x)
- Kitchatinov, L. L., & Rudiger, G. 1993. Lamda-effect and Differential Rotation in Stellar Convection Zones. *A&A*, 276, 96. <https://ui.adsabs.harvard.edu/abs/1993A&A...276...96K> [accessed on May 1, 2021]
- Komm, R., González Hernández, I., Howe, R., & Hill, F. 2015. Solar-Cycle Variation of Subsurface Meridional Flow Derived with Ring-Diagram Analysis. *Sol. Phys.*, 290, 3113, doi: [10.1007/s11207-015-0729-5](https://doi.org/10.1007/s11207-015-0729-5)
- Kosovichev, A. G. 1996. Helioseismic Constraints on the Gradient of Angular Velocity at the Base of the Solar Convection Zone. *ApJ*, 469, L61, doi: [10.1086/310253](https://doi.org/10.1086/310253)
- . 2009. Photospheric and Subphotospheric Dynamics of Emerging Magnetic Flux. *Space Sci. Rev.*, 144, 175, doi: [10.1007/s11214-009-9487-8](https://doi.org/10.1007/s11214-009-9487-8)
- Kosovichev, A. G., & Duvall, T. L., J. 1997. Acoustic Tomography of Solar Convective Flows and Structures. In *SCORe'96: Solar Convection and Oscillations and their Relationship*, ed. F. P. Pijpers, J. Christensen-Dalsgaard, & C. S. Rosenthal, Vol. 225, 241–260, doi: [10.1007/978-94-011-5167-2_26](https://doi.org/10.1007/978-94-011-5167-2_26)
- Kosovichev, A. G., Zhao, J., & Ilonidis, S. 2018. Local Helioseismology of Emerging Active Regions: A Case Study. In *Variability of the Sun and Sun-like Stars: from Asteroseismology to Space Weather*, ed. J. P. Rozelot & E. S. Babayev, 15–38. <https://ui.adsabs.harvard.edu/abs/2018vsss.book...15K> [accessed on May 1, 2021]
- Kühnlein, C., Deconinck, W., Klein, R., et al. 2019. FVM 1.0: A Nonhydrostatic Finite-volume Dynamical Core for the IFS. *Geosci. Model Dev.*, 12, 651, doi: [10.5194/gmd-12-651-2019](https://doi.org/10.5194/gmd-12-651-2019)
- Küker, M., Rüdiger, G., & Kitchatinov, L. L. 2011. The Differential Rotation of G Dwarfs. *A&A*, 530, A48, doi: [10.1051/0004-6361/201015994](https://doi.org/10.1051/0004-6361/201015994)
- Landau, L. D., & Lifshitz, E. M. 1977, In *Quantum Mechanics (Third Edition)*, ed. L. D. Landau & E. M. Lifshitz (Oxford: Pergamon Press), 431–452, doi: [10.1016/B978-0-08-020940-1.50021-9](https://doi.org/10.1016/B978-0-08-020940-1.50021-9)
- Lazrek, M., Pantel, A., Fossat, E., et al. 1996. Is the Solar Core Rotating Faster or Slower Than the Envelope? *Sol. Phys.*, 166, 1, doi: [10.1007/BF00179353](https://doi.org/10.1007/BF00179353)

- Leighton, R. B. 1969. A Magneto-Kinematic Model of the Solar Cycle. *ApJ*, 156, 1, doi: [10.1086/149943](https://doi.org/10.1086/149943)
- Leighton, R. B., Noyes, R. W., & Simon, G. W. 1962. Velocity Fields in the Solar Atmosphere. I. Preliminary Report. *ApJ*, 135, 474, doi: [10.1086/147285](https://doi.org/10.1086/147285)
- Liang, Z.-C., & Chou, D.-Y. 2015. Effects of Solar Surface Magnetic Fields on the Time-distance Analysis of Solar Subsurface Meridional Flows. *ApJ*, 805, 165, doi: [10.1088/0004-637X/805/2/165](https://doi.org/10.1088/0004-637X/805/2/165)
- Lilly, K. 1966. On the Application of the Eddy Viscosity Concept in the Inertial Sub-range of Turbulence. In *NCAR Manuscript No. 123*, doi: [10.5065/D67H1GGQ](https://doi.org/10.5065/D67H1GGQ)
- Lin, C.-H., & Chou, D.-Y. 2018. Solar-cycle Variations of Meridional Flows in the Solar Convection Zone Using Helioseismic Methods. *ApJ*, 860, 48, doi: [10.3847/1538-4357/aac026](https://doi.org/10.3847/1538-4357/aac026)
- Lipps, F. B., & Hemler, R. S. 1982. A Scale Analysis of Deep Moist Convection and Some Related Numerical Calculations. *J. Atmos. Sci.*, 39, 2192, doi: [10.1175/1520-0469\(1982\)039<2192:ASAODM>2.0.CO;2](https://doi.org/10.1175/1520-0469(1982)039<2192:ASAODM>2.0.CO;2)
- Margolin, L. G., Smolarkiewicz, P. K., & Wyszogrodzki, A. A. 2006. Dissipation in Implicit Turbulence Models: A Computational Study. *J. Appl. Mech.*, 73, 469, doi: [10.1115/1.2176749](https://doi.org/10.1115/1.2176749)
- Margolin, L. G., Smolarkiewicz, P. K., & Wyszogrodzki, A. A. 2002. Implicit Turbulence Modeling for High Reynolds Number Flows. *J. Fluids Eng.*, 124, 862, doi: [10.1115/1.1514210](https://doi.org/10.1115/1.1514210)
- Mathews, J. 1962. Gravitational Multipole Radiation. *J. Soc. Ind. Appl. Math.*, 10, 768. <http://www.jstor.org/stable/2098922> [accessed on May 1, 2021]
- Matilsky, L. I., Hindman, B. W., & Toomre, J. 2019. The Role of Downflows in Establishing Solar Near-surface Shear. *ApJ*, 871, 217, doi: [10.3847/1538-4357/aaf647](https://doi.org/10.3847/1538-4357/aaf647)
- . 2020. Revisiting the Sun's Strong Differential Rotation along Radial Lines. *ApJ*, 898, 111, doi: [10.3847/1538-4357/ab9ca0](https://doi.org/10.3847/1538-4357/ab9ca0)
- Miesch, M. S., Brun, A. S., & Toomre, J. 2006. Solar Differential Rotation Influenced by Latitudinal Entropy Variations in the Tachocline. *ApJ*, 641, 618, doi: [10.1086/499621](https://doi.org/10.1086/499621)

- Mitra-Kraev, U., & Thompson, M. J. 2007. Meridional Flow Profile Measurements with SOHO/MDI. *Astron. Nachr.*, 328, 1009, doi: [10.1002/asna.200710873](https://doi.org/10.1002/asna.200710873)
- Moffatt, H. K. 1978, Magnetic Field Generation in Electrically Conducting Fluids (Cambridge: Cambridge University Press), doi: [10.1017/S002211207923067X](https://doi.org/10.1017/S002211207923067X)
- Müller, D., St. Cyr, O. C., Zouganelis, I., et al. 2020. The Solar Orbiter Mission. Science Overview. *A&A*, 642, A1, doi: [10.1051/0004-6361/202038467](https://doi.org/10.1051/0004-6361/202038467)
- Nandy, D., & Choudhuri, A. R. 2002. Explaining the Latitudinal Distribution of Sunspots with Deep Meridional Flow. *Science*, 296, 1671, doi: [10.1126/science.1070955](https://doi.org/10.1126/science.1070955)
- Nelson, N. J., Brown, B. P., Brun, A. S., Miesch, M. S., & Toomre, J. 2013. Magnetic Wreaths and Cycles in Convective Dynamos. *ApJ*, 762, 73, doi: [10.1088/0004-637X/762/2/73](https://doi.org/10.1088/0004-637X/762/2/73)
- Nigam, R., Kosovichev, A. G., & Scherrer, P. H. 2007. Analytical Models for Cross-Correlation Signal in Time-Distance Helioseismology. *ApJ*, 659, 1736, doi: [10.1086/512535](https://doi.org/10.1086/512535)
- Novak, J., Cornou, J. L., & Vasset, N. 2010. A Spectral Method for the Wave Equation of Divergence-free Vectors and Symmetric Tensors inside a Sphere. *J. Comput. Phys.*, 229, 399, doi: [10.1016/j.jcp.2009.09.033](https://doi.org/10.1016/j.jcp.2009.09.033)
- Papini, E., Birch, A. C., Gizon, L., & Hanasoge, S. M. 2015. Simulating acoustic waves in spotted stars. *A&A*, 577, A145, doi: [10.1051/0004-6361/201525842](https://doi.org/10.1051/0004-6361/201525842)
- Papini, E., Gizon, L., & Birch, A. C. 2014. Propagating Linear Waves in Convectively Unstable Stellar Models: A Perturbative Approach. *Sol. Phys.*, 289, 1919, doi: [10.1007/s11207-013-0457-7](https://doi.org/10.1007/s11207-013-0457-7)
- Parchevsky, K. V., & Kosovichev, A. G. 2007. Three-dimensional Numerical Simulations of the Acoustic Wave Field in the Upper Convection Zone of the Sun. *ApJ*, 666, 547, doi: [10.1086/520108](https://doi.org/10.1086/520108)
- . 2009. Numerical Simulation of Excitation and Propagation of Helioseismic MHD Waves: Effects of Inclined Magnetic Field. *ApJ*, 694, 573, doi: [10.1088/0004-637X/694/1/573](https://doi.org/10.1088/0004-637X/694/1/573)
- Parchevsky, K. V., Zhao, J., Hartlep, T., & Kosovichev, A. G. 2014. Verification of the Helioseismology Travel-time Measurement Technique and the Inversion Procedure for Sound Speed Using Artificial Data. *ApJ*, 785, 40, doi: [10.1088/0004-637X/785/1/40](https://doi.org/10.1088/0004-637X/785/1/40)

- Parker, E. N. 1955. Hydromagnetic Dynamo Models. *ApJ*, 122, 293, doi: [10.1086/146087](https://doi.org/10.1086/146087)
- . 1979, *Cosmical Magnetic Fields: their Origin and their Activity* (Oxford: Oxford University Press). <https://ui.adsabs.harvard.edu/abs/1979cmft.book.....P> [accessed on May 1, 2021]
- Pesnell, W. D., Thompson, B. J., & Chamberlin, P. C. 2012. The Solar Dynamics Observatory (SDO). *Sol. Phys.*, 275, 3, doi: [10.1007/s11207-011-9841-3](https://doi.org/10.1007/s11207-011-9841-3)
- Pipin, V. V., & Kosovichev, A. G. 2018. On the Origin of the Double-cell Meridional Circulation in the Solar Convection Zone. *ApJ*, 854, 67, doi: [10.3847/1538-4357/aaa759](https://doi.org/10.3847/1538-4357/aaa759)
- . 2019. On the Origin of Solar Torsional Oscillations and Extended Solar Cycle. *ApJ*, 887, 215, doi: [10.3847/1538-4357/ab5952](https://doi.org/10.3847/1538-4357/ab5952)
- Prusa, J. M., Smolarkiewicz, P. K., & Wyszogrodzki, A. A. 2008. EULAG, a Computational Model for Multiscale Flows. *Comput. Fluids*, 37, 1193, doi: [10.1016/j.compfluid.2007.12.001](https://doi.org/10.1016/j.compfluid.2007.12.001)
- Racine, É., Charbonneau, P., Ghizaru, M., Bouchat, A., & Smolarkiewicz, P. K. 2011. On the Mode of Dynamo Action in a Global Large-eddy Simulation of Solar Convection. *ApJ*, 735, 46, doi: [10.1088/0004-637X/735/1/46](https://doi.org/10.1088/0004-637X/735/1/46)
- Rajaguru, S. P., & Antia, H. M. 2015. Meridional Circulation in the Solar Convection Zone: Time-distance Helioseismic Inferences from Four Years of HMI/SDO Observations. *ApJ*, 813, 114, doi: [10.1088/0004-637X/813/2/114](https://doi.org/10.1088/0004-637X/813/2/114)
- . 2020. Time-Distance Helioseismology of Deep Meridional Circulation. *Astrophys. Space Sci. Proc.*, 57, 107, doi: [10.1007/978-3-030-55336-4_11](https://doi.org/10.1007/978-3-030-55336-4_11)
- Reinecke, M., & Seljebotn, D. S. 2013. Libsharp - Spherical Harmonic Transforms Revisited. *A&A*, 554, A112, doi: [10.1051/0004-6361/201321494](https://doi.org/10.1051/0004-6361/201321494)
- Rempel, M. 2005. Solar Differential Rotation and Meridional Flow: The Role of a Subadiabatic Tachocline for the Taylor-Proudman Balance. *ApJ*, 622, 1320, doi: [10.1086/428282](https://doi.org/10.1086/428282)
- Ruediger, G. 1989, *Differential Rotation and Stellar Convection: Sun and Solar-Type Stars* (Berlin: Akademie-Verlag). <https://ui.adsabs.harvard.edu/abs/1989drsc.book.....R> [accessed on May 1, 2021]

- Sanchez, S., Fournier, A., Pinheiro, K., & Aubert, J. 2014. A Mean-field Babcock-Leighton Solar Dynamo Model with Long-term Variability. *Acad. Bras. Cinc.*, 86, 11, doi: [10.1590/0001-37652014111212](https://doi.org/10.1590/0001-37652014111212)
- Schad, A., Timmer, J., & Roth, M. 2013. Global Helioseismic Evidence for a Deeply Penetrating Solar Meridional Flow Consisting of Multiple Flow Cells. *ApJ*, 778, L38, doi: [10.1088/2041-8205/778/2/L38](https://doi.org/10.1088/2041-8205/778/2/L38)
- Scharmer, G. B., Bjelksjo, K., Korhonen, T. K., Lindberg, B., & Petterson, B. 2003. The 1-meter Swedish solar telescope. In Society of Photo-Optical Instrumentation Engineers (SPIE) Conference Series, Vol. 4853, *Innovative Telescopes and Instrumentation for Solar Astrophysics*, ed. S. L. Keil & S. V. Avakyan, 341–350, doi: [10.1117/12.460377](https://doi.org/10.1117/12.460377)
- Scherrer, P. H., Bogart, R. S., Bush, R. I., et al. 1995. The Solar Oscillations Investigation - Michelson Doppler Imager. *Sol. Phys.*, 162, 129, doi: [10.1007/BF00733429](https://doi.org/10.1007/BF00733429)
- Scherrer, P. H., Schou, J., Bush, R. I., et al. 2012. The Helioseismic and Magnetic Imager (HMI) Investigation for the Solar Dynamics Observatory (SDO). *Sol. Phys.*, 275, 207, doi: [10.1007/s11207-011-9834-2](https://doi.org/10.1007/s11207-011-9834-2)
- Schou, J. 2015. Effects of Granulation on the Visibility of Solar Oscillations. *A&A*, 580, L11, doi: [10.1051/0004-6361/201526445](https://doi.org/10.1051/0004-6361/201526445)
- Schou, J., Antia, H. M., Basu, S., et al. 1998. Helioseismic Studies of Differential Rotation in the Solar Envelope by the Solar Oscillations Investigation Using the Michelson Doppler Imager. *ApJ*, 505, 390, doi: [10.1086/306146](https://doi.org/10.1086/306146)
- Schou, J., Howe, R., Basu, S., et al. 2002. A Comparison of Solar p-mode Parameters from the Michelson Doppler Imager and the Global Oscillation Network Group: Splitting Coefficients and Rotation Inversions. *ApJ*, 567, 1234, doi: [10.1086/338665](https://doi.org/10.1086/338665)
- Shibata, K., Tajima, T., Steinolfson, R. S., & Matsumoto, R. 1989. Two-dimensional Magnetohydrodynamic Model of Emerging Magnetic Flux in the Solar Atmosphere. *ApJ*, 345, 584, doi: [10.1086/167932](https://doi.org/10.1086/167932)
- Smolarkiewicz, P. K. 2006. Multidimensional Positive Definite advection Transport Algorithm: an overview. *Int. J. Numer. Methods Fluids*, 50, 1123, doi: [10.1002/flid.1071](https://doi.org/10.1002/flid.1071)

- Smolarkiewicz, P. K., & Charbonneau, P. 2013. EULAG, A Computational Model for Multiscale Flows: An MHD Extension. *J. Comp. Phys.*, 236, 608, doi: [10.1016/j.jcp.2012.11.008](https://doi.org/10.1016/j.jcp.2012.11.008)
- Smolarkiewicz, P. K., & Prusa, J. M. 2002. Forward-in-time Differencing for Fluids: Simulation of Geophysical Turbulence. In *Turbulent Flow Computation*, ed. D. Drikakis & B. J. Guerts (Dordrecht: Springer), 279–312, doi: [10.1007/0-306-48421-8](https://doi.org/10.1007/0-306-48421-8)
- Snodgrass, H. B., & Ulrich, R. K. 1990. Rotation of Doppler Features in the Solar Photosphere. *ApJ*, 351, 309, doi: [10.1086/168467](https://doi.org/10.1086/168467)
- Steenbeck, M., Krause, F., & Rädler, K. H. 1966. Berechnung der Mittleren Lorentz-Feldstärke für ein Elektrisch Leitendes Medium in Turbulenter, durch Coriolis-Kräfte Beeinflusster Bewegung. *Z. Naturforsch. A*, 21, 369, doi: [10.1515/zna-1966-0401](https://doi.org/10.1515/zna-1966-0401)
- Stefan, J. T., Kosovichev, A. G., & Stejko, A. M. 2021. Analysis of Time-Distance Helioseismology for Detection of Emerging Active Regions. *ApJ*, in press. <https://arxiv.org/abs/2012.01367> [accessed on May 1, 2021]
- Stein, R. F., & Nordlund, Å. 2001. Solar Oscillations and Convection. II. Excitation of Radial Oscillations. *ApJ*, 546, 585, doi: [10.1086/318218](https://doi.org/10.1086/318218)
- Stejko, A. M., Guerrero, G., Kosovichev, A. G., & Smolarkiewicz, P. K. 2020. 3D MHD Modeling of the Impact of Subsurface Stratification on the Solar Dynamo. *ApJ*, 888, 16, doi: [10.3847/1538-4357/ab5854](https://doi.org/10.3847/1538-4357/ab5854)
- Stejko, A. M., Kosovichev, A. G., & Mansour, N. N. 2021a. Helioseismic Modeling of Background Flows. *ApJS*, 253, 9, doi: [10.3847/1538-4365/abd3fe](https://doi.org/10.3847/1538-4365/abd3fe)
- Stejko, A. M., Kosovichev, A. G., & Pipin, V. V. 2021b. Helioseismic Signatures of One- and Two-cell Meridional Circulation. *ApJ*, 911, 90, doi: [10.3847/1538-4357/abec70](https://doi.org/10.3847/1538-4357/abec70)
- Thorne, K. S. 1980. Multipole Expansions of Gravitational Radiation. *Rev. Mod. Phys.*, 52, 299, doi: [10.1103/RevModPhys.52.299](https://doi.org/10.1103/RevModPhys.52.299)
- Toriumi, S., Ilonidis, S., Sekii, T., & Yokoyama, T. 2013. Probing the Shallow Convection Zone: Rising Motion of Subsurface Magnetic Fields in the Solar Active Region. *ApJ*, 770, L11, doi: [10.1088/2041-8205/770/1/L11](https://doi.org/10.1088/2041-8205/770/1/L11)
- Toriumi, S., & Wang, H. 2019. Flare-productive Active Regions. *Living Rev. Sol. Phys.*, 16, 3, doi: [10.1007/s41116-019-0019-7](https://doi.org/10.1007/s41116-019-0019-7)

- Ulrich, R. K. 2010. Solar Meridional Circulation from Doppler Shifts of the Fe I Line at 5250 Å as Measured by the 150-foot Solar Tower Telescope at the Mt. Wilson Observatory. *ApJ*, 725, 658, doi: [10.1088/0004-637X/725/1/658](https://doi.org/10.1088/0004-637X/725/1/658)
- Varshalovich, D. A., Moskalev, A. N., & Khersonskii, V. K. 1988, Quantum Theory of Angular Momentum (World Scientific), doi: [10.1142/0270](https://doi.org/10.1142/0270)
- Warnecke, J. 2018. Dynamo Cycles in Global Convection Simulations of Solar-like Stars. *A&A*, 616, A72, doi: [10.1051/0004-6361/201732413](https://doi.org/10.1051/0004-6361/201732413)
- Warnecke, J., Käpylä, P. J., Mantere, M. J., & Brandenburg, A. 2013. Spoke-like Differential Rotation in a Convective Dynamo with a Coronal Envelope. *ApJ*, 778, 141, doi: [10.1088/0004-637X/778/2/141](https://doi.org/10.1088/0004-637X/778/2/141)
- Warnecke, J., Rheinhardt, M., Tuomisto, S., et al. 2018. Turbulent Transport Coefficients in Spherical Wedge Dynamo Simulations of Solar-like Stars. *A&A*, 609, A51, doi: [10.1051/0004-6361/201628136](https://doi.org/10.1051/0004-6361/201628136)
- Woodard, M. F. 1984. Short-Period Oscillations in the Total Solar Irradiance. PhD thesis, Univ. of California, SD. <https://ui.adsabs.harvard.edu/abs/1984PhDT.....34W> [accessed on May 1, 2021]
- Wray, A. A., Bensassi, K., Kitiashvili, I. N., Mansour, N. N., & Kosovichev, A. G. 2015. Simulations of Stellar Magnetoconvection using the Radiative MHD Code ‘StellarBox’. *arXiv e-prints*, arXiv:1507.07999. <https://arxiv.org/abs/1507.07999> [accessed on May 1, 2021]
- Zerilli, F. J. 1970. Tensor Harmonics in Canonical Form for Gravitational Radiation and Other Applications. *J. Math. Phys.*, 11, 2203, doi: [10.1063/1.1665380](https://doi.org/10.1063/1.1665380)
- Zhao, J., Bogart, R. S., Kosovichev, A. G., Duvall, T. L., J., & Hartlep, T. 2013. Detection of Equatorward Meridional Flow and Evidence of Double-cell Meridional Circulation inside the Sun. *ApJ*, 774, L29, doi: [10.1088/2041-8205/774/2/L29](https://doi.org/10.1088/2041-8205/774/2/L29)
- Zhao, J., Hartlep, T., Kosovichev, A. G., & Mansour, N. N. 2009. Imaging the Solar Tachocline by Time-distance Helioseismology. *ApJ*, 702, 1150, doi: [10.1088/0004-637X/702/2/1150](https://doi.org/10.1088/0004-637X/702/2/1150)
- Zhao, J., & Kosovichev, A. G. 2004. Torsional Oscillation, Meridional Flows, and Vorticity Inferred in the Upper Convection Zone of the Sun by Time-distance Helioseismology. *ApJ*, 603, 776, doi: [10.1086/381489](https://doi.org/10.1086/381489)

- Zhao, J., Nagashima, K., Bogart, R. S., Kosovichev, A. G., & Duvall, T. L., J. 2012. Systematic Center-to-limb Variation in Measured Helioseismic Travel Times and its Effect on Inferences of Solar Interior Meridional Flows. *ApJ*, 749, L5, doi: [10.1088/2041-8205/749/1/L5](https://doi.org/10.1088/2041-8205/749/1/L5)
- Zhao, J., Stejko, A., & Chen, R. 2016. Effect of Foreshortening on Center-to-limb Variations of Measured Acoustic Travel Times. *Sol. Phys.*, 291, 731, doi: [10.1007/s11207-016-0864-7](https://doi.org/10.1007/s11207-016-0864-7)